ONE DIMENSIONAL ZINC OXIDE NANOSTRUCTURES FOR OPTOELECTRONIC

APPLICATIONS: SOLAR CELLS AND PHOTODIODES

Except where reference is made to the work of others, the work described in this dissertation is my own or was done in collaboration with my advisory committee. This dissertation does not include proprietary or classified information.

_____

An-Jen Cheng

Certificate of Approval:

_____	_____
Minseo Park, Co-Chair Assistant Professor Physics	Yonhua Tzeng, Co-Chair Professor Emeritus Electrical and Computer Engineering
_____	_____
Richard C. Jaeger Distinguished University Professor Electrical and Computer Engineering	Jianjun Dong Associate Professor Physics

_____

George T. Flowers
Interim Dean
Graduate School

ONE DIMENSIONAL ZINC OXIDE NANOSTRUCTURES FOR OPTOELECTRONIC APPLICATIONS: SOLAR CELLS AND PHOTODIODES

An-Jen Cheng

A Dissertation

Submitted to

the Graduate Faculty of

Auburn University

in Partial Fulfillment of the

Requirement for the

Degree of

Doctor of Philosophy

Auburn, Alabama
August 9, 2008

ONE DIMENSIONAL ZINC OXIDE NANOSTRUCTURES FOR OPTOELECTRONIC APPLICATIONS: SOLAR CELLS AND PHOTODIODES

An-Jen Cheng

_____

Signature of Author

_____

Date of Graduation

VITA

An-Jen Cheng, son of En-Jer, Jack, Jang (Cheng) and Chin-hua (Jane-hua) Chen, was born on April 26, 1980, in Tainan, Taiwan, Republic of China. He has a sister; An-Li (Alice) Cheng was born in Auburn, Alabama, majors in finance at National Center University, Taiwan. He entered Physics Department, Chun-Yuan Christian University in September, 1999, and graduate with the degree of Bachelor of Science in June, 2003. He entered the graduate program in the Department of Electrical and Computer Engineering in Auburn University under the guidance of Dr. Yonhua Tzeng in January, 2004, and graduate with the degree of Master of Science in May, 2006. He continues pursuing the degree of Doctor of Philosophy in Auburn University also under the guidance of Dr. Yonhua Tzeng from Department of Electrical and Computer Engineering and Dr. Minseo Park from Department of Physics in January, 2006.

DISSERTATION ABSTRACT

ONE DIMENSIONAL ZINC OXIDE NANOSTRUCTURES FOR OPTOELECTRONIC APPLICATIONS: SOLAR CELLS AND PHOTODIODES

An-Jen Cheng

Doctor of Philosophy, September 9, 2008
(Master of Science, Auburn University, May 11, 2006)
(B.S. Chun-Yuan Christian University, R.O.C Taiwan, June 2003)

219 Typed Pages

Directed by Minseo Park and Yonhua Tzeng

Several different morphologies of one-dimensional (1-D) ZnO nanostructured arrays can be controllably synthesized using novel thermal chemical vapor deposition at low temperatures. Well aligned and two dimensional periodic ZnO nanostructures like, nanorods, nanoflower, inverse nanotetrapod, nanonail, and nanotip can be controllably grown on different substrates, and have been analyzed by scanning electron microscopy, X-ray diffraction, photoluminescence, Raman spectrum and so on, in order to comprehensively study the electrical and optical properties of ZnO nanostrucutres. The purpose to growth those ZnO nanostructures are to utilize these materials for optoelectronic device applications.

Raman scattering was performed to study the well-aligned ZnO nanorods. ZnO nanorods is determined to be relatively strain free by analyzing the $E_2^{(2)}$ mode using Raman spectroscopy. The free carrier concentration as well as electron mobility was obtained by the line shape analysis of the coupled A_1(LO) phonon plasmon mode for the first time of ZnO nanostructures. The position of the LO phonon peak was found to be depended on both the temperature and the LO phonon-plasmon coupling; therefore, the local temperature of the nanorod sample was estimated based on the integration ratio of Stokes to anti-Stokes Raman peak intensity. As a comparison, the LPP modes collected from single crystal bulk ZnO wafer was also investigated.

Micro-Raman diagnosis of phonon lifetime of bulk ZnO, aligned ZnO nanorods, and nanopowder is performed by Raman spectrum. Experiments have observed that the Raman linewidth of most materials exhibits a finite width that indicates the presence decay channels that shorten the phonon lifetime. The Raman modes investigated in this study are the $E_2^{(2)}$, E_1(TO), A_1(TO) and A_1(LO). The $E_2^{(2)}$ mode Raman linewidth becomes broaden as the dimensionality decreases from bulk to one dimensional nanorods and then to nanopowder.

Dye sensitized solar cell was fabricated using a quasi-aligned 1-D ZnO nanostructure. The ZnO nanostructures were successfully grown on indium tin oxide coated glass substrate *via* a thermal chemical vapor deposition. Current-voltage measurements were performed to extract the working performance of the solar cell. The power conversion efficiency of our device is 0.6%, which is comparable to the DSSC fabricated based on MOCVD-grown ZnO nanostructures.

ACKNOWLEDGEMENTS

The author would like to extend his deepest thanks to Prof. Yonhua Tzeng and Prof. Minseo Park for their supervising this dissertation and being a great academic advisor during the author's graduate study in Auburn University.

The author would like to express his appreciation to Dr. Dake Wang for lots of useful discussions in ZnO and other wide band-gap semiconductors optical properties, Raman spectrum, Photoluminescence, AFM, NSOM, and so on.

The author would like to express his appreciation to Ms. Hee Won Seo for her early stage investigations on growing ZnO nanostructures.

The author would like to express his appreciation to Prof. Jianjun Dong and Prof. Richard C. Jaeger for being author's committee members.

The author would like to thank Prof. An-Ban Chen for providing guidance and encouragement all along during author Ph.D. study in Auburn University.

The author would like express his deepest special appreciation to his lovely girl friend Huihua (Vicky) Shu for her supports and encouragements in spirit, body, and life.

Finally, the author would like to thanks his family, especially his mother Chin-hua Chen and his uncle K. S. Wang, for their love, encouragement, dedication, and support.

Thanks to Jesus Christ who is my only Lord and the savior of my life.

我所做的, 你如今不知道,後來必明白. (約 13:7)

What I am doing, you do not understand now, but you will understand later.

(John 13:7)

但那等候耶和華的必重新得力,他們必如鷹展翅上騰;

他們奔跑卻不困倦,行走卻不疲乏. (以 40:31)

They that hope in the LORD will renew their strength, they will soar as with eagles' wings; they will run and not grow weary, walk and not grow faint.

(Isaiah 40:31)

我們有這寶貝放在瓦器裏,要顯明這莫大的能力

是出於上帝, 不是出於我們 (哥後 4:7)

But we hold this treasure in earthen vessels, that the surpassing power may be of God and not from us.

(2 Corinthians 4:7)

Style manual or journal used: Bibliography conforms to those of the Journal of Applied Physics

Computer software used: Microsoft Word 2007 for Windows, Origin 7.5, Mathematica.

TABLE OF CONTENTS

LIST OF FIGURES

LIST OF TABLES

CHAPTER 1

INTRODUCTION

Low dimensional semiconductor materials for nano scale and high performance device fabrication have been intensively studied in the past decades. Since Iijima discovered the carbon nanotubes in 1991 carbon-based nanostructured materials like nano-crystalline diamond, fullerenes, nanotubes, as well as group III-V and II-VI wide band gap compound semiconductors have attracted considerable attention due to their extraordinary properties among the fields of chemical, physical, optical and electrical fields. More and more research efforts have been invested to study nanostructured based wide band gap semiconductors, such as silicon carbide (SiC), gallium nitride (GaN) and zinc oxide (ZnO) , which have been evidenced by a myriad of publications in this field.

Wide band gap semiconductor nanostructures have attracted enormous attention due to their unique properties which are result of low dimensionality. Furthermore, many advantages are provided by the intrinsic nature of wide band gap semiconductors. Nanostructures with size ranging in the submicron scale to as small as a few nanometers share the same lattice constants and crystal structures as their bulk counterpart, as demonstrated by X-ray diffraction pattern and transmission electron microscopy. Therefore, for nano-sized materials, many bulk properties are still preserved. However, a

very large surface-to-volume-ratio makes their physical, optical, and electrical properties remarkably different from their bulk counterpart. Nanostructural units resemble one continuous single crystal that is in sharp contrast with the bulk material structure, which are full of structural defects. Nanostructures should have at least one dimension less than 100nm, typically including layer-like, wire-like, and particle-like structures. The electron-hole interaction has been greatly enhanced due to the increased electronic density of states. Similar enhancement occurs for the electron-phonon interactions. The quantum confinement effect occurs as the dimensionality shrinks to less than the critical length (<10nm) of the corresponding physical processes, such as mean free path of electrons, coherence length, or screening length. Quantum confinement effects of charge carriers and lattice vibrations begin to strongly affect their behaviors. The surface electronic and vibrational modes play significant roles in nanostrucutres since constituent atoms in a nanostructure are very close to the surface. Two-dimensional (2D) quantum wells, one-dimensional quantum wires, and zero-dimensional quantum dots are the typical structural forms.

Wide band gap semiconductors are commonly defined as a material with a band gap of larger than 2 eV. Most wide band gap semiconductors lie on a broader line between semi-insulators and semiconductors. However, their electronics properties can be tuned by proper doping. A relatively low intrinsic carrier concentration and high breakdown voltage, i.e. diamond, SiC, and GaN, allow high temperature, high frequency, and high power device applications. For direct band gap semiconductors, like GaN and ZnO, the high electronic energy of band-to-band transitions allow emission in the green, blue, or

UV region of the spectrum. The novel properties of semiconductor nanostructures like the greatly enhanced Purcell factor can be exploited in a plethora of optoelectronic applications. Optoelectronic devices such as light emitting devices, photodetectors, and laser diodes have been commercially fabricated based on bulk or thin film wide band gap semiconductors like GaN.

Functional oxides of wide band gap semiconductors can arrange to form several types of novel nanostructures such as nanobelts, nanowires, nanoneedles, nanonsheeets, and nanohelixes. These nanostructures are the fundamental building blocks of smart devices. Many metal oxide materials such as ZnO, SnO_2, In_2O_3, Ga_2O_3 and PbO_2 have been investigated and synthesized. Zinc oxide (ZnO), a key technological material, is the metal oxide that will be focused in this study.

Oxides are the basis of smart and functional materials. Synthesis and potential device applications using functional oxides have attracted great attention due to the fact that physical properties of these oxides can be tuned. Functional oxides have two structural characteristics: cations with mixed valence states, and anions with deficiencies (vacancies). By adjusting either or both of these characteristics, the electrical, optical, magnetic, and chemical properties can be tuned, giving the possibility of fabricating smart devices. The structures of functional oxides are very diverse and varied, and there are everlasting new phenomena and applications constantly being discovered. These unique characteristics make oxides one of the most diverse materials, covering several application fields such as semiconductor, superconductor, ferroelectrics, and magnetics.

Wurtzite structure ZnO, a wide band gap (3.37eV) II-VI compound semiconductor, has a hexagonal wurtzite structure. The structure of ZnO can be simply described as a number of alternating planes composed of tetrahedrally coordinated O^{2-} and Zn^{2+} ions, heaped alternatively along the c-axis. The tetrahedral coordination in ZnO leads to a non-central symmetric structure, which is one of the most important structural characteristics of wurtzite nanostructured materials. ZnO shows strong electromechanical coupling due to its unique structure, which results in strong piezoelectric and pyroelectric properties. The other important structural characteristic of ZnO is its polar surfaces. The most common polar surface is the basal plane. ZnO is also a bio-safe and biocompatible material, which can be used for biomedical applications without further coating.

Transparent thin film transistors (TFTs) using ZnO as an active channel have achieved much higher field effect mobility than amorphous silicon TFTs. These transistors can be widely used for display applications. ZnO has been proposed as a more promising candidate for UV emitting than GaN because of its larger exciton binding energy (60meV). This leads to the reduction of UV lasing threshold and the increment of UV emitting efficiency at room temperature.

A wide variety of geometrical morphologies of metal oxide nanostructured materials have been synthesized via chemical vapor deposition. These can be classified into: tubes, cages, cylindrical wires, rod, co-axial and bi-axial cables, ribbons or belts, sheets, and diskettes.

The synthetic methods can be generally classified into several categories: (1) vapor-phase growth, which includes thermal evaporation, chemical vapor-phase deposition,

metal-organic chemical vapor-phase deposition, arc-discharge, laser ablation, and etc, (2) chemical bath solution growth, (3) sol-gel, (4) templated-based methods, and etc. Among these methods, thermal evaporation is the most commonly used growth method in the investigation of oxide nanostructures. Different kinds of nanostructures can be prepared using thermal evaporation technique by adjusting processing parameters such as pressure, growth temperature, carrier and reactant gas flow rates, and substrates.

In this dissertation, works can be categorized into three phases as followed: (1) growth of ZnO nanostructures using thermal chemical vapor deposition (CVD); (2) analysis of electrical and optical properties of those materials; and (3) application of ZnO nanostrucutres for dye sensitized solar cells. The light matter interaction in ZnO nanostructures has been investigated by optical spectroscopy such as Raman spectroscopy and photoluminescence. The mechanisms of many optical and electrical processes have been studied in detail.

Growth of ZnO nanostructures using thermal CVD is described in detail Chapter 3. In this work, we presented a new modified method to synthesize ZnO nanostructures of different morphologies by conventional oxygen assisted pressure-controlled thermal CVD. A simple double-source-double tube (DSDT) is modified to growth those ZnO nanostructures. ZnO nanostructures have been synthesized over a large area with/without using metallic catalyst. A systematic investigation of using thermal CVD to synthesize ZnO nanostructures, such as nanorods, nanoflowers, nanonails, and nanocrowns, on ITO and Si substrates has been carried out. Based on this apparatus, well-aligned ZnO nanostructures can be prepared onto different types of substrates without the need of

catalysts. The nanostructuray features of ZnO can be properly tuned by employing different processing parameters with high reproducibility. The as-grown nanostructures are investigated in detail in terms of their structural and optical properties. The as-grown ZnO nanostructures were also analyzed by scanning electron microscopy and X-ray diffraction. The growth mechanisms and the formation of ZnO nanostructures will be described further.

In Chapter 4, the Raman scattering of the aligned ZnO nanorods are investigated. It was determined by Raman spectroscopy that the ZnO nanorods are relatively strain-free. The free carrier concentration as well as electron mobility of the ZnO nanorods were obtained by the line shape analysis of the coupled A_1(LO) phonon-plasmon mode. It was the first time for this Raman scattering based characterization technique to be applied on semiconductor nanostructures. Electrical characterization techniques such as Hall and impedance measurements are contact methods to measure carrier concentration and mobility. On the other hand, optical measurement such as Raman spectroscopy provides a non-contact method to measure the electronic parameters. Optical method is more useful than electrical counterpart when analyzing low-dimensional materials system due to difficulty in preparation of the electrical contacts to nanostructure.

Raman characteristic of LO-phonon-plasmon coupled (LPP) modes is used to demonstrate the combined of phonon confinement and crystal orientation, both of which become significantly importance with decreasing dimensionality. LPP modes are intensively investigated in wide band-gap polar semiconductors using Raman spectroscopy. For polar semiconductors, the long-range electrostatic Coulomb force

interacts with LO phonons and the fluctuated charge-density wave of an injected plasmon resulting in the formation of two hybrid excitations of the LO-phonon-plasmon coupled modes. The position of the LO phonon peak was found to be dependent on both the temperature and the LO phonon-plasmon coupling; it is crucial to consider temperature effect in determining the frequency of the uncoupled LO phonon mode for the line shape analysis. The relative energy shift and line-width broadening of the phonon modes are directly influenced by the concentration and the mobility of free charge carriers, respectively. The local temperature of the nanorod sample was estimated based on the ratio of Stokes to anti-Stokes Raman peak intensity. The LO phonon-plasmon coupled modes of ZnO nanorods have not been investigated. Therefore, in this work, we have studied LPP modes in ZnO nanorods comprehensively. As a comparison, the LPP modes collected from single crystal bulk ZnO wafer was also investigated. Electronic properties of undoped bulk zinc oxide (ZnO) and vertically well-aligned ZnO nanorods have been investigated using micro-Raman spectroscopy. The mobility and carrier concentration of the undoped bulk ZnO obtained from the line shape analysis are 108.87cm^2/V-s and $1.94\times10^{17}/cm^3$, respectively. The carrier concentration of the undoped ZnO obtained from the C-V measurement further confirmed the results obtaining form A_1(LO) mode line shape analysis. The mobility and carrier concentration of well-aligned ZnO nanorods are 84.76cm^2/V-s and $3.76\times10^{17}/cm^3$, respectively. The mobility of well-aligned ZnO nanorods is about 20% lower than that of undoped bulk ZnO. This can be due to enhanced surface scattering.

Micro-Raman diagnosis of phonon lifetime of bulk ZnO, aligned ZnO nanorods, and nanopowder is presented in Chapter 5. Numerous scientific investigation issues of improving the crystal quality as well as diagnosis techniques for wide band gap semiconductors have been intensively carried out in order to control wide band gap semiconductor related devices fabrication and their performance. Profound knowledge of the vibrational properties of this material is necessary to determine the transport characteristics and phonon interaction with the free carrier, both of which have great impact on optoelectronic device performance. Raman spectrum has been widely used for analyzing the wide band gap semiconductors properties such as carrier concentration, phonon interaction and dynamics. The interaction between phonon and free carriers degrades the performance of the devices; however, the phonon interactions can also be utilized to engineer certain laser devices.

The phonon lifetime of wide band gap semiconductors is important and needs to be characterized. One convenience method is to employ Raman spectroscopy since the phonon lifetime and the factors affecting it can be obtained from the Raman phonon linewidth. The theory of spectral line shape of a collected spectrum signal in a dispersive media predicts that the line shape to be Lorentzian and the linewidth, which is a parameter determining the damping effect, to be inversely proportional to the lifetime of the spectrum signal. The line shape is expected to be infinitesimally narrow for an ideal harmonic crystal. However, experiments have observed that the Raman linewidth of most materials exhibits a finite width indicating the presence decay channels that shorten the phonon lifetime. The Raman modes investigated in this study are the $E_2^{(2)}$, $E_1(TO)$,

A_1(TO) and A_1(LO). The $E_2^{(2)}$ mode exhibits a visibly asymmetric line shape which can be attributed to anharmonic interaction with transverse and longitudinal acoustic phonon combinations in the vicinity of K point, where the two-phonon density of states displays a sharp edge around the $E_2^{(2)}$ frequency.

In this work, we present the study of the room temperature phonon lifetimes of the Raman phonon modes in undoped bulk zinc oxide (ZnO) single crystal, aligned ZnO nanorods, and nanopowder. We observed that the $E_2^{(2)}$ mode Raman linewidth was broaden as the dimensionality decreases from bulk to one dimensional nanorods and then to nanopowder. The $E_2^{(2)}$ mode phonon lifetime decreased from 0.6ps to 0.5ps and then 0.4 ps as the dimensionality of the ZnO decreased.

In Chapter 6, ZnO nanorods based dye sensitized solar cell (DSSC) is presented. DSSC was fabricated using a quasi-aligned 1-dimensional (1-D) ZnO nanostructure. The ZnO nanostructures were successfully grown on indium tin oxide (ITO) coated glass substrate *via* a thermal CVD. It has been considered that thermal CVD is not suitable for the growth of ZnO nanostructure on ITO/glass due to the high processing temperature. However, we have demonstrated that a densely populated ZnO nanostructure can be successfully prepared on ITO/glass substrate by a novel DSDT CVD process. As-grown ZnO nanostructures were studied using X-ray diffraction, scanning electron microscopy, UV-vis spectrophotometer, Raman scattering and photoluminescence. The electrical characteristics of the DSSC based on the ZnO nanostructures were studied using current-voltage measurement. The power conversion efficiency of our device is 0.6%, which is comparable to the DSSC fabricated based on MOCVD-grown ZnO nanostructures.

CHAPTER 2

LITERATURE REVIEW

The advent of one-dimensional (1D) wide band-gap metal-oxide semiconductors has caused a large billowy effect not only on electronics but also on photophysics and photochemistry. Zinc oxide (ZnO) belongs to the II-IV binary compound semiconductor with the space group of P63mc.[1] ZnO has been one of the most intensively studied metal-oxide semiconductor materials in recent years because of its fairly large band-gap, high exciton binding energy, and strong piezoelectric responses. ZnO is one of the most important materials for blue and ultra-violet optical device applications. Other favorable aspects of ZnO include radiation hardness, biocompatibility, a broad chemistry leading to many opportunities for wet chemical etching, and a low power threshold for optical pumping. [2]

ZnO typically occurs in three different crystal structures, wurtzite (hexagonal symmetry), zinc blende (cubic symmetry), and rock salt structure. ZnO crystallize behaves in a stable wurtzite structural formation under a pressure of one atmosphere at room temperature as shown in Figure 2.1. This hexagonal lattice formation belongs to the space group, $P6_3mc$. At room temperature, the lattice constant a=0.325 nm, which represents the basal plane; the lattice constant c=0.521 nm, which is in the basal direction.

The c/a ratio is 1.602, which is close to the 1.633 ratio of an ideal hexagonal closed packed structure. This structure is characterized by two interconnecting sub-lattices of Zn^{2+} and O^{2-} such that each Zn ion is surrounded by a tetrahedral O ion, and vice-versa. The two sets of sub-lattices are separated by u=0.385 in fractional coordinates along the c-axis. The parameter u of ZnO crystal is derived from the ideal wurtzite structure (u=0.375), and is defined as the amount by which each atom is displaced with respect to the next along the c-axis. Two important characteristics of the wurtzite structural formation are its non-central symmetry and its polar surface. ZnO can be simply described as a number of alternating planes each consisted of tetrahedral coordinated O^{2-} and Zn^{2+} ions, stacked alternately along the c-axis. The tetrahedral coordination in ZnO leads to a non-central symmetric structure, which is one of the most important characteristics of wurtzite structural materials. The lack of central symmetry in wurtzite structure, combined with large electromechanical coupling, results in strong piezoelectric and pyroelectric properties. The other important structural characteristic of ZnO is the polar surfaces. The most common polar surface is the basal plane.

An internal charge of ZnO is created by positively charged Zn-(0001) and negatively charged O-$(000\bar{1})$ surfaces, resulting in the creation of dipole moment and spontaneous polarization along the c-axis as well as a divergence in surface energy.[3,4] To maintain a stable structure, the polar surfaces generally have facets or exhibit massive surface reconstructions. However, ZnO -$\pm(000\bar{1})$ are exceptions: they are atomically flat, stable and without reconstruction.[4,5] The other two most commonly observed facets for ZnO are $(11\bar{2}0)$ (a-axis) and $(10\bar{1}0)$, which are non-polar surfaces and they have lower

energy than the (0001) facets. The polar faces posses different chemical and physical properties, while the O-terminated face possess a slightly different electronic structure to the other three faces. [6] Moreover, the polar surface and the $(10\bar{1}0)$ surface are found to be stable; whrereas, the $(11\bar{2}0)$ face is less stable and generally has a higher level of surface roughness. The tetrahedral coordination of this compound is also a common indicator of sp^3 covalent bonding. However, the Zn-O bond also possesses very strong ionic character, and thus ZnO lies on the borderline between being classified as a covalent or ionic compound, with an iconicity of f_i=0.616 on the Phillips iconicity scale. [7] As a result of the sp^3 hybridization of the oxygen 2p orbital and zinc 3d orbital, each oxygen/zinc ion is surrounded by four zinc/oxygen ions at the corners of a tetrahedron, in zinc blende or wurtzite structures.

The (0001) planes in zinc oxide possess the highest surface energy among the low-index planes indicating that no surface construction or passivation has taken place. As a result, zinc oxide nanostructures usually have the highest growth rate along the c-axis so as to minimize the surface area of the (0001) planes. This has been most commonly observed in the vapor phase growth process.

In addition to the wurtzite structure, ZnO is known to crystallize in the cubic zincblende and rocksalt (NaCl) structure. Zinc blende ZnO is stable only by growth on a cubic substrate [8,9,10] whereas the rocksalt structure is a high-pressure metastable structure forming at pressure near 10GPa. Table 2.1 shows a compilation of the basic physical parameters of ZnO. [11] ZnO wurtzite structure is a direct band gap semiconductor with a band gap of 3.37eV at room temperature.

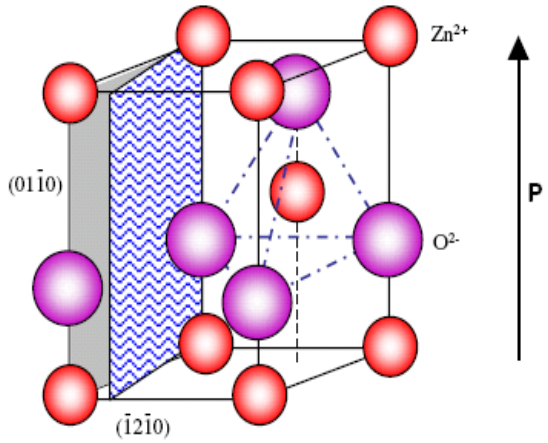

Figure 2.1: The wurtzite structure model of ZnO. The tetrahedral coordination of Zn-O is shown. [4]

The electronic band structure of ZnO has been studied by using Local Density Approximation (LDA) [12, 13] which incorporates atomic self-interaction corrected pseudopotentials (SIC-PP) to accurately estimate the Zn 3d electron. Figure 2.2 shows the band structure diagram reported by Vogel *et al.* [12]

Table 2.1 Properties of wurtzite ZnO. [11]

Property	Value
Lattice parameters at 300K	
a_o	0.32495 nm
c_o	0.52069 nm
a_o/c_o	1.602
u	0.375
Density	5.606 g/cm^3
Stable phase at 300K	Wurtzite
Melting point	1975°C
Thermal conductivity	0.6, 1-1.2
Linear expansion coefficient (/°C)	a_o: 6.5×10^{-6} c_o: 3.0×10^{-6}
Static dielectric constant	8.656

Refractive index	2.008, 2.029
Energy gap	3.4eV, direct
Intrinsic carrier concentration	$<10^6$ cm-3 (max n-type doping) $>10^{20}cm^{-3}$ (max p-type doping $<10^{17}$ cm^{-3})
Exciton binding energy	60meV
Electron effective mass	0.24
Electron Hall mobility at 300K for low n-type conductivity	200 cm^2/V-s
Hole effective mass	0.59
Hole Hall mobility at 300K for low p-type conductivity	5-50 cm^2/V-s

The band structure of ZnO possesses high symmetry lines in the hexagonal Brillouin zone. The direct interband transition takes place between the lowest conduction band and the top of the valence band at the Γ point k=0 in the Brillouin zone. The lowest conduction band of zinc oxide is s-like state having Γ_7^c symmetry , whereas the valence band is a six-fold degenerate p-type and is split into three subbands due to spin-orbit interaction and crystal-field effect.[14] The near band gap intrinsic absorption and emission spectrum is dominated by transitions involving these three valence bands and the conduction band. Hopfield has reported a formula for the valence band mixing, the extent of which is controlled by the relative magnitudes of the spin-orbit and crystal field splitting. [15] If the energy of the top most valence band is taken as zero (E_A=0), the energies of the two other exciton lines in this formala are given as,

$$E_{B,C} = -\frac{\delta+\Delta}{2} \pm \sqrt{[(\frac{\delta+\Delta}{2})^2 - \frac{2}{3}\delta\Delta]}, \qquad (1)$$

where δ and Δ repesent the spin orbit and crystal field parameters, and can be calculated by using the measured level splitting E_{AB} and E_{BC}. From the band diagram in Figure 2.2,

the bottom 10 bands, which are located at -9eV, correspond to Zn 3d levels. The next 6 bands between -5eV to 0eV correspond to O 2p bonding states. The first two conduction bands are strongly localized and correspond to empty Zn 3s levels.

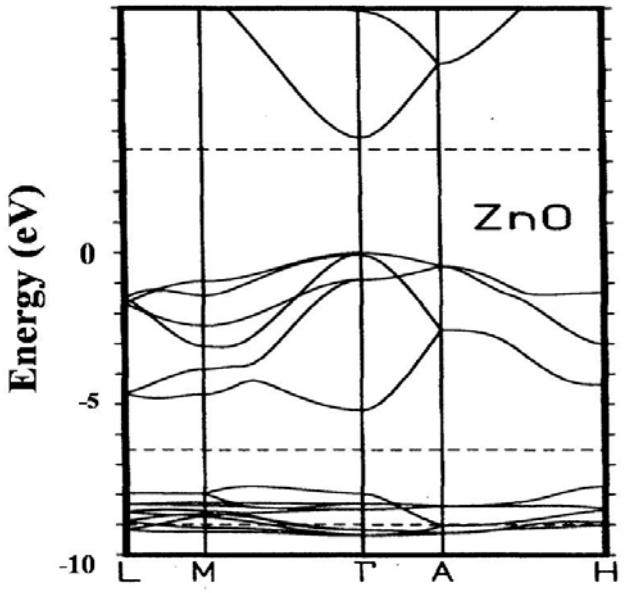

Figure 2.2 The LDA band structure of bulk wurtzite ZnO using diminant SIC-PP. [16]

Experimentally, the ZnO valence band is splitted into three band states. The splitting of the valence band is ishown in Figure 2.3. A (heavy hole), B (light hole), and C (crystal-field split band) indicates spin-orbit and crystal-field splitting. The A and C subbands are known to possess Γ_7 symmetry, while the middle band, B, has Γ_9 symmetry. The band gap is temperature dependence up to 300K given by the relationship:

$$E_g = E_g(T=0)\frac{5.05\times10^{-4}T^2}{900-T} \qquad (2)$$

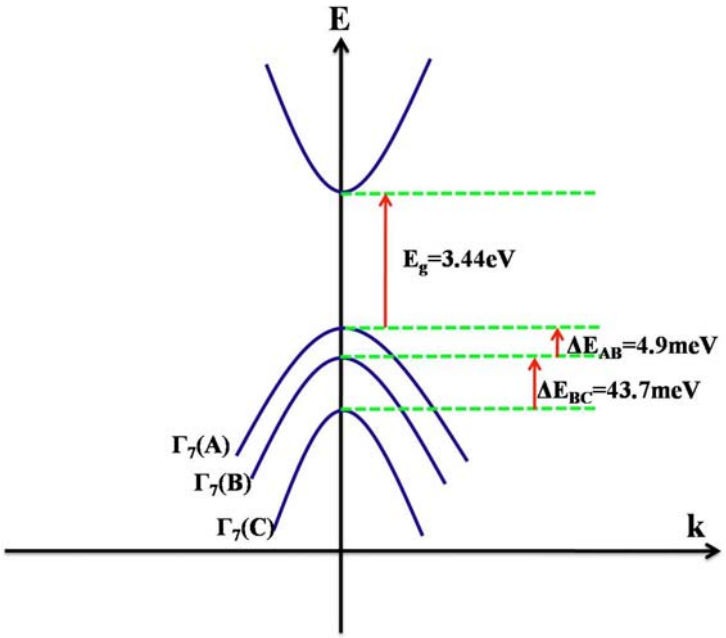

Figrue 2.3 Schematic diagram represents the crystal-field and spin-orbit splitting of the valence band of ZnO into 3 subbandstatesA, B, and C at 4.2K. [2]

The optical properties of wide band-gap semiconductors originate from both intrinsic and extrinsic effects. Intrinsic optical transitions take place between free electrons in the conduction band and holes in the valence band, which include excitonic effects due to Coulomb interaction. Excitons are classified into free and bound excitons. In high-quality substrates with low impurity concentrations, the free excitons can also exhibit excited states in addition to their ground-state transitions. Extrinsic properties are related to dopant/impurities or other point defects and complexes that usually create electronic states within the band-gap. Therefore, the optical absorption and emission processes can be tuned. The electronic states of the bound excitons, may be bound to neutral or charged donors and acceptors, depending strongly on the semiconductor material and in particular their band structure. For a shallow neutral donor bound exciton (DBE), the two electrons

in the bound exciton state are assumed to pair off into a two-electron state with zero spin. The additional hole is then weakly bound in the net hole-attractive Coulomb potential set up by this bound two-electron aggregate. For a shallow neutral acceptor bound exciton (ABE), it is expected to generate a two-hole state derived from the topmost valence band and one electron interaction. Many other extrinsic transitions can be observed in the optical spectrum, such as free-to-bound (electron-acceptor), bound-to-bound (donor-acceptor), and etc. The optical properties of ZnO greatly influence by the energy band structure and lattice dynamic. In a single crystal wurtzite ZnO, there are 4 atoms per unit cell, giving rise to 12 phonon modes. These modes are important for understanding the thermal, electrical, and optical properties of the crystal, which are described as follows: one longitudinal acoustic (LA), two transverse-acoustic (TA), three longitudinal-optical (LO) and six transverse-optical branches. The A_1 and E_1 branches are Raman and infrared active, while the two E_2 branches (non-polar) are only Raman active. The low E_2 mode is associated with the vibrations in the Zn sub-lattice, while the high E_2 mode is associated with the oxygen atoms only. [2] The B_1 branches are always inactive. The phonon modes of ZnO have been intensively studied and will be described in detail in Chapter 3 and 4.

In Raman spectroscopy, the sample is irradiated by intense laser beams in the UV-visible region (υ_o), and the scattered light is usually observed in the direction perpendicular to the incident beam. The scattered light consisted of two types: one, called Rayleigh scattering, is strong has the same frequency as the incident beam (υ_o); and the other, called Raman scattering, is very weak (10^{-5} of the incident beam) with frequencies $\upsilon_o \pm \upsilon_m$, where υ_m is a vibrational frequency of a molecule. The $\upsilon_o - \upsilon_m$ and $\upsilon_o + \upsilon_m$ lines are

referred to as the Stokes and anti-Stokes line. In Raman spectroscopy, we measured the vibrational frequency (υ_m) as a shift from the incident beam frequency (υ_o). [16, 17]

Raman scattering can be explained as the electrical field strength (E) of the electromagnetic wave (laser beam) fluctuates with time as shown by the equation,

$$E=E_o\cos 2\pi\upsilon_o t$$

, in this equation, E_o is the vibrational amplitude and υ_o is the frequency of the laser. If a diatomic molecule is irradiated by this light, an electric dipole moment P is generated:

$$P=\alpha E=\alpha\, E_o\cos 2\pi\upsilon_o t \qquad (3)$$

Here, α is a proportionality constant and is called polarizability. If the molecule is vibrating with a frequency υ_m, the nuclear displacement q is written as

$$q=q_o\cos 2\pi\,\upsilon_m t, \qquad (4)$$

, where q_o is the vibrational amplitude. For a small perturbation, α is a linear function of q. Thus we can write as following,

$$\alpha=\alpha_0+(\frac{\partial\alpha}{\partial q})_0 q_0+..... \qquad (5)$$

Here, α_0 is the polarizability at the equilibrium position, and $(\frac{\partial\alpha}{\partial q})_0$ is the rate of change of α with respect to the change in q, evaluated at the equilibrium position.

Combining equations (3) with (4) and (5) we obtain [16, 17]

$$P = \alpha E_0 \cos 2\pi \upsilon_0 t = \alpha_0 E_0 \cos 2\pi \upsilon_0 t + (\frac{\partial \alpha}{\partial q})_0 q E_0 \cos 2\pi \upsilon_0 t$$

$$= \alpha_0 E_0 \cos 2\pi \upsilon_0 t + (\frac{\partial \alpha}{\partial q})_0 q_0 E_0 \cos 2\pi \upsilon_0 t \cos \upsilon_m t$$

$$= \alpha_0 E_0 \cos 2\pi \upsilon_0 t + \frac{1}{2}(\frac{\partial \alpha}{\partial q})_0 q_0 E_0 [\cos\{2\pi(\upsilon_0 + \upsilon_m)t\} + \cos\{2\pi(\upsilon_0 - \upsilon_m)t\}]$$

According to the classical theory, the first term represents an oscillating dipole that radiates light of frequency υ_o (Rayleigh scattering), while the second term corresponds to the Raman scattering of frequencies $\upsilon_o + \upsilon_m$ (anti-Stokes) $\upsilon_o - \upsilon_m$ (Stokes). Therefore, the Raman intensity is proportional to the first derivative of the polarizability. If $(\frac{\partial \alpha}{\partial q})_0$ is zero, the vibration is not Raman-active. To be Raman-active, the rate of change of polarizability (α) with the vibration must not be zero.

The exciton binding energies of ZnO are much larger than the room temperature thermal energy (25 meV), making the excitonic recombination processes possible even at room temperature, whereas in other wide-band-gap semiconductors such as gallium nitride the electron-hole-plasma transition is the dominate recombination processes. Separated electrons and holes can be easily recombined and more vulnerable to the trapping of various defect levels between the valence band and the conduction band in the crystal. Thus, efficient excitonic emission processes persist in ZnO at room temperature and higher, and in fact, prototype ZnO based-LED have been shown to operate at nearly 400°C. Therefore, it is desirable to have a material with large exciton binding energy for optoelectronic applications. Low-temperature absorption [18,19], reflection [20,21] photoreflectance, [22,23] and photoluminescence [24,25,26] spectroscopy were usually performed to study the transition energies related to the intrinsic excitons in zinc oxide.

Low-temperature (~ 4K) photoluminescence measurement has the ability to reveal multiple emission lines resulted from the electronic transitions near the band edge. They include: free excitonic emissions and their phonon replicas, neutral donor bound excitons, neutral acceptor bound excitons, two-electron satellites, and shallow donor-shallow acceptor pair transitions etc. At room temperature, all the aforementioned emission lines are not resolved, and only a relatively broad and featureless emission band can be seen. Although the exciton binding energy of zinc oxide is very large, the energy of its longitudinal optical phonon is intensively energetic (72 meV). The free excitons can be easily ionized upon scattering by longitudinal optical phonons. It was found that the electro-phonon coupling strength decreases with decreasing size of the zinc oxide nanostructures. [27] A more reliable excitonic recombination is occurred in zinc oxide nanostructures than in zinc oxide bulk. Zinc oxide strongly absorbs photons with energy larger than the band gap, and the absorption coefficient of zinc oxide found to be ~160,000 cm^{-1} at 325 nm.[28]

The extrinsic optical property of zinc oxide is related to native point defects, impurities, and other defects. These defect states are generated from discrete energy levels in the band gap. Some of them can be expressed through visible luminescence *via* radiative recombination processes of electron hole pairs. The mechanism of the defect related to electron-hole recombination processes in zinc oxide has been intensively investigated, but remains a controversial issue. Among the different mechanisms proposed to explain the visible luminescence, oxygen vacancies have been widely considered as the most probable candidate, although no consensus could be reached regarding the charge state of

the oxygen vacancy; *i.e.*, singly ionized [29] or doubly ionized oxygen vacancy [30]. Oxygen annealing is usually employed to modify the level of oxygen deficiency in zinc oxide. However, contradictory results regarding the effect of annealing on the luminescence property of zinc oxide have been reported. In some reports [31,32,33], oxygen annealing has enhanced the intensity of the visible luminescence band and has reduced the intensity of the band edge ultraviolet luminescence band. Yet in some other experiments, the exact opposite trend was observed. [34, 35] It was also found that the change in relative intensities of the visible and ultraviolet luminescence bands depends on the annealing temperature. [36, 37]

Table 2.2 Key properties of the binary II-VI oxide. [38]

	ZnO	MgO	CdO
E_g(eV)	3.4	7.8	2.2
m_e^*	0.28	0.35	-
m_{hh}^*(mo)	0.78	1.60[001], 2.77[111]	-
m_{lh}^*(mo)	-	0.35[001] 0.31[111]	-
a(Å)	3.2	4.2	4.7
c(Å)	5.2	-	-
Structure	Wurtzite	Rocksalt	rocksalt

Wurtzite zinc oxide is native n-type semiconductor due to the deviation from stoichiometry. The electrical properties of ZnO are hard to quantify due to large variations in quality of different samples. The background carrier concentration varies a lot in terms of the quality of the crystal layers but is usually about $10^{16}cm^{-3}$. The largest reported concentration in n-type doped zinc oxide is in the order of 10^{20} cm^{-3}, while for p-

type zinc oxide the largest reported concentration is approximately $10^{19}cm^{-3}$. [39,40] However, such high levels of p-conductivities are questionable and have not been experimentally verified. [37] It has been shown that zinc interstitials (Zn_I) rather than oxygen vacancies (V_o) are the dominant native shallow donors in zinc oxide with an ionization energy of about 30-50 meV. [41] However, this conclusion has been challenged by Kohan *et al.* who showed theoretically that both V_o and Zn_I have high formation energies in n-type ZnO, and furthermore, they are deep rather than shallow donors. [42] This theoretical prediction indicates that neither V_o nor Zn_I would exist in measurable quantities, and that even if one or the other were present, its ionization energy would be too high to produce free electrons. However, later on Zhang *et al.* reported that Zn_I is actually a shallow donor rather than a deep donor and this has also been observed via electron-irradiation experiments. [38, 43] The argument of V_o and ZnO as the dominant donors in as-grown ZnO was further challenge by Van de Walle's theoretical result that described hydrogen (H) is always a donor in ZnO, because it is easily ionized and that is has a low enough formation energy to be abundant. Therefore, Van de Walle suggested that hydrogen was likely to be a dominant background donor in ZnO materials that was exposed to H during grow. [44] Experimentally, this prediction has been confirmed, and that a shallow donor due to H exists in seeded chemical vapor transport (SCVT) growth of ZnO and can contribute significantly to its conductivity. [45] Even though Koha *et al.* and Van de Walle results seems conflicting, both of their results are valid since each theory deals with isolated defects, not complexes. Zinc oxide can achieve n^+ characteristics via doping with group III elements aluminum, gallium, and

indium to substitute zinc, or by doping with group VII elements chlorine and iodine to substitute oxygen. [46, 47, 48] Aluminum, gallium and indium have been used to create highly-conductive zinc oxide films. A conductive zinc oxide film has achieved a resistivity as low as 1.2×10^{-4} Ω-cm using metal-organic chemical vapor deposition. [49] P-type doping of zinc oxide is quite difficult, similar to dealing with wide band-gap semiconductors, since a high level of background n-type conductivity is presented in zinc oxide or other related wide band-gap semiconductors. P-type doping may be achieved by substituting zinc sites by group I elements such as lithium and sodium or by substituting oxygen sites by group V elements such as nitrogen, phosphor and arsenic. [50, 51, 52] Nitrogen should be a good acceptor dopant because it has an electronics core structure and ionic radius similar to that of oxygen thus it readily substitutes with oxygen. Many different growth methods have been applied to synthesize p-type ZnO, including chemical vapor deposition, pulsed laser deposition (PLD), molecular-beam epitaxy (MBE), metal-organic chemical vapor deposition (MOCVD), and sputtering. Recently, a MBE scheme utilizing temperature modulation has been employed to generate high quality p-type material, which has been used to fabricate homoepitaxial light emitting diode (LED). [53] Temperature modulation MBE growth initially deposits a thin layer of n^+ ZnO at low temperature and then a thin undoped layer is grown at higher temperature producing a crystal of higher quality. This process is cycled until the full layer is grown.

The bandgap of zinc oxide can be tuned from 2.8 to 4.0 eV by alloying with cadmium and magnesium. The bandgap of zinc oxide can be widened by alloying zinc oxide with magnesium oxide which has a wider bandgap of 7.7 eV, [54] or narrowed by alloying

with cadmium oxide which has a smaller bandgap of 2.3 eV. [55] The problem with zinc oxide/magnesium oxide alloying is the limited solubility of magnesium in zinc oxide (< 4 mol %). [56]

The thermal conductivity, κ (W/cm*K) of a semiconductor is an important property when considering high-power/high temperature devices. It is a kinetic property influenced by the vibrational, rotational, and electronic degree of freedoms, and is predominantly limited by phonon-phonon scattering in a pure crystal. ZnO, like most of the semiconductor, contains a large number of point defects, which have a significant effect on the thermal conductivity. The highest measured values of thermal conductivity come from a study done on vapor-phase grown samples which measured the conductivity on the polar faces of ZnO. [57] This study gives the values of κ=1.02±0.07 and 1.16±0.08W/cm*K from the Zn face of two different samples, and κ=1.10±0.09 and 0.98±0.08 W/cm*K from the O face of the two samples. These value are considerably higher than other values measured from ZnO which typically fall in the range of κ=0.6-1W/cm*K. [58]

Growth of ZnO nanostructures can be achieved by different methods like thermal evaporation, pulsed laser deposition, metal-organic chemical vapor deposition, and solution-based techniques which are the most popular methods. The various growth techniques of zinc oxide can be categorized based on the different growth mechanisms. For thermal evaporation growth, vapor-liquid-solid, vapor-solid, and catalyst-free self-nucleation process are the main growth mechanisms. Vapor-liquid-solid growth is perhaps the most widely used growth method, in which the metal catalyst particles are

used to assist the growth of the nanostructures. Transmission electron microscopy reveals the existence of metal nanoparticles on the top of the nanostructures synthesized via vapor-liquid-solid process. [59, 60 ,61] Various metals such as gold, silver, copper and transition metals can be used catalyst. [62, 63, 64] Due to the eutectic phase formed by the metal alloy, liquid alloy droplets are formed at the initial stage of the growth process. Following the formation of the liquid alloy droplets, gaseous species are absorbed onto the liquid droplets. Nucleation centers are formed upon the supersaturation of the liquid alloy. With continuous feeding of reactant species, nanostructures start to grow from the nucleation sites. The diameter of the nanowire synthesized via vapor-liquid-solid growth largely depends on the size of the liquid alloy droplet. [65] In the case of catalyst-free growth, zinc oxide nucleation takes place on the surface of the substrate. Epitaxy growth is possible on lattice-matched substrates. The growth rate of vapor-solid process is much lower than that of the vapor-liquid-solid process, due to the inefficient absorption of reactant at the nucleation sites. In vapor-solid process, crystal growth takes place at the interface of solid and vapor, whereas in vapor-liquid-solid process, it takes place at the interface of solid and liquid.

Pulsed-laser deposition (PLD) is a type of physical deposition, which is usually used for semiconductor thin film deposition. PLD have already been widely used for ZnO thin film deposition. Okada *et al.* reported a new method for synthesizing ZnO nanorods by applying the basic idea of PLD, which is so-called nanoparticle-assisted pulsed-laser deposition (NAPLD). [66] NAPLD, a non-catalyst growth method, is the method in which the species created by laser ablation are first converted into nanoparticles by

condensation in the background gas. Then, formed nanoparticles are transported onto a heated substrate where nano-structured crystals are synthesized. Since the nanoparticles require a lower melting temperature than in a bulk form; therefore, the ZnO nanostructures can be synthesized at a relatively lower substrate temperature. It is suggested that these particles are the trace of the aggregated nano-particles in the background gas that can be obviously detected by Rayleigh scattering technique. If the nanoparticles were deposited on a high temperature (~700°C) substrate, hexagonal ZnO nanocrystal will be uniformly observed and there is no trace of particles.[67,68]

Metal organic chemical vapor deposition (MOCVD) is a widely used technique for synthesizing semiconductor thin film, and has also been used for ZnO nanorod growth. MOCVD provides a non-catalyst growth ZnO nanorods technique, which produces high purity ZnO nanorods and easily fabricates of nanorod quantum structures. The catalyst free growth mechanism of ZnO nanorods has not been clearly investigated. The main reason for anisotropic growth is the anisotropic surface energy in ZnO. Moreover, high speed laminar gas flow in a certain growth condition may induce turbulent flow between the nanostructures, which results in adsorption of fresh reactant gases only on nanorod tips. Since more surface steps exist on nanorod tips, the nanorod growth rate is higher on nanorod tips than on side wall. Diethylzinc (DEZn) is used as the zinc precursor and high-purity oxygen is used as the oxidizer. [69] DEZn is introduced into the reaction chamber using Ar carrier through a bubbling cylinder kept at constant temperature and pressure. Convectional gas flow is suppressed by employing N_2 as the pushing gas forming an annular curtain gas flow around the reactor walls. The operating pressure is

around 2-3.5 kPa. Park *et al.* have studied the morphology change with respect to the change of growth temperature (T_g) of MOCVD. [70] The morphology of ZnO change dramatically with T_g. Figure 2.4 is the cross section SEM images of ZnO grown at different growth temperatures as reported by Park *et al.* At higher growth temperature of 260°C≤ T_g≤320°C, arrays of vertically well-aligned ZnO nanorods form, and at further higher temperatures of 320°C≤ T_g≤380°C, nanoneedle shaped ZnO forms. Finally, at T_g>380°C, ZnO nanowires begin to grow on top of a continuous ZnO layer. The growth temperature T_g is one of the key processing parameters and needs to be well-controlled within a narrow margin in order to grow the desired ZnO nanostructures using MOCVD technique.

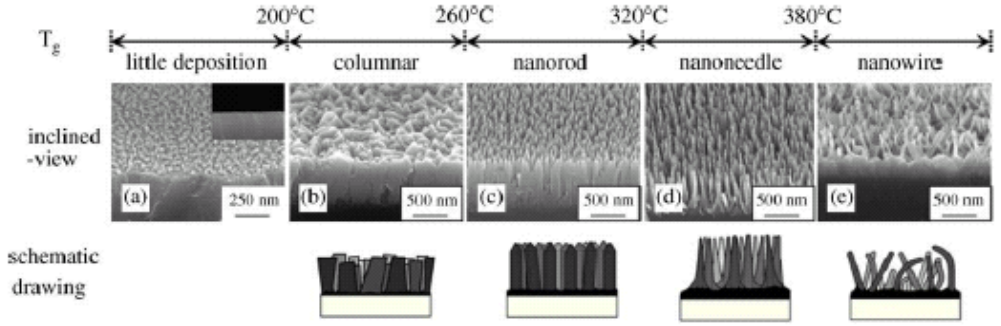

Figure 2.4: SEM cross section images of ZnO grown at various growth temperature (a) T_g≤ 200°C, (b) 200°C< T_g ≤260°C, (c) 260°C<T_g ≤320°C (d) 320°C < T_g ≤380°C, and (e) T_g> 380°C. The ZnO morphologies grown at these temperature regimes are schematically described. [68]

CHAPTER 3

GROWTH OF ZINC OXIDE NANOSTRUCUTRES

3.1 Introduction

Excellent and unique properties of 1D wide band gap metal-oxide semiconductors have attracted a broad spectrum of interest with regards to their applications in electronics, photophysics, and photochemistry. Among them, ZnO is one of the most intensively studied metal-oxide semiconductor materials in recent years due to its properties, namely its wide band gap energy (3.37eV), large exciton binding energy (~60meV), and relatively strong piezoelectric responses. As a wide band gap semiconductor, ZnO is considered to be the most promising candidate for solid state blue to UV optoelectronic device applications, including laser development. The ZnO nanostructure has been recognized as a new spotlight candidate for renewable energy conversion device like dye-sensitized solar cell [71], hybrid inorganic polymer solar cells [72], extreme thin absorber (ETA) solar cell [73], and so forth. In order to utilize ZnO for optoelectronics devices, it is necessary to grow ZnO nanostructures on top of transparent conductive oxide (TCO) substrates such as indium tin oxide (ITO).

In order to comprehensively study the properties of ZnO nanostructures, a variety of growth methods have been vigorous investigated, such as vapor-liquid-solid (VLS)

[74,75], metal-organic chemical vapor deposition (MOCVD) [76], pulsed laser deposition (PLD) [77], plasma-enhanced chemical vapor deposition [78], hydrothermal synthesis [79], and spray pyrolysis [80]. Among those growth techniques, nanoparticles of gold (Au) or nickel (Ni) are heavy utilized as the catalyst precursor. Even though utilizing the metal catalysts can achieve more controllable structures, ZnO will natively possess contaminants from the catalysts. ZnO nanowires have been successfully synthesized using thermal evaporation without applying metal catalyst. It was found that the properties of ZnO nanostructures can be significantly varied corresponding to different growth methods or morphologies that have been generated. Yao *et al.* has synthesized needle-like ZnO morphology by controlling the growth temperature at 750-800° *via* thermal deposition. [81] They also demonstrate that growth temperature is a critical parameter for controlling the morphologies of ZnO nanostructures when using thermal evaporation method. Figure 3.1 is the result of different nanostructural morphologies carried out at different temperatures. Wan *et al*. reported a method of rapidly heating zinc pallets at 900°C in a one end closed quartz tube under normal ambient air, which typically produces tetrapods like ZnO structure. [82,83] Lao *et al.* have produced nail-like nanorods at the growth temperature of 950-970°C using thermal evaporation and condensation.[84] However, those growth processes require a relatively high growth temperature, and there is a scarceness of optical and electrical properties of those samples reported. It was also found that a higher quality of ZnO nanostructures can be synthesized if a thermal gas-phase deposition method is employed. However, it needs a higher growth temperature and metal catalyst particles to enhance the nanowires growth. Growth

of aligned ZnO on silicon substrates can be easily achieved by different methods. However, only hydrothermal synthesis and MOCVD have been reported for low temperature growth on glass coated TCO substrates. Therefore, a more comprehensive investigation on the processing-structure-property relationship is useful and necessary in order for better controlled growth of highly oriented ZnO nanostructures.

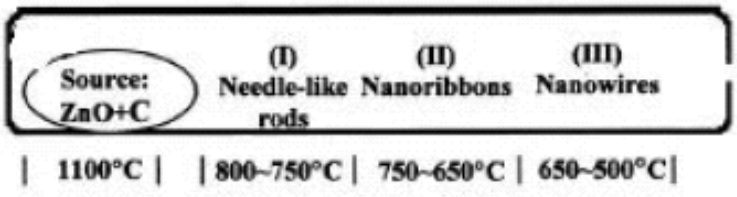

Figure 3.1 Schematic of different ZnO nanostructures grown at different temperature zone. [79]

The photoluminescence and Raman spectroscopy of ZnO nanostructures demonstrate different electric and optical characteristics from its bulk or thin film counterparts due to their very large surface-to-volume-ratio, the intrinsic defects presented in the materials, the strong electric field from band bending, and other unique properties. Quantum confinement effect becomes an issue as the dimensions of the nanostructures reach to a few nanometers or even smaller. Quantum confinements can affect to both the charge carriers and optical phonons, leading to emission or scattering peak shifts and broadening the luminescence and Raman spectrums. ZnO nanoneedles/nanorods have been considered as an excellent platform for field emission applications. ZnO nanostructures are unintentionally n-typed doped and possess good electrical conductivity, and their resistance to ion bombardment makes them especially attractive for field emission

applications in poor vacuums and low pressure air environments. [85] It is important to realize that optical and electrical properties of ZnO nanostructures are profoundly affected by their surface conditions, more specifically their ambient environment, and temperature.

In this work, we presented a method to synthesize ZnO nanostructures with different morphologies by conventional oxygen assisted pressure-controlled thermal CVD. A simple double-source-double-tube (DSDT) system is utilized to grow these ZnO nanostructures. ZnO nanostructures have been synthesized over a large area with/without using metallic catalyst. A systematic investigation of thermal CVD synthesis of ZnO nanostructure, such as nanorod, nanoflower, nanonail, nanocrown, on ITO substrates has been studied. Moreover, based on this setup system, well-aligned ZnO nanostructures can also be grown onto different substrates, like Si (100), without any catalyst applied. The morphologies of ZnO can be tuned by employing different processing parameters with a high level of reproducibility. The as-grown nanosructures are investigated in detail in terms of their structural and optical properties. Furthermore, the growth mechanism and the formation of the ZnO nanostrucutures will be described. The as-grown ZnO nanostructures were also analyzed by scanning electron microscopy and X-ray diffraction.

3.2 Thermal CVD Synthesis of ZnO Nanostructures

The synthesis of ZnO nanowires has been carried out using a single-zone resistive heating tube furnace (Lindberg, 54233). Silicon wafer was cleaned by the RCA (BCD) wafer cleaning process, dipped in deionized water for 15 min, and then dried by

compressed nitrogen. For catalyst-assisted VLS growth, Si substrates (100) were spin coated at 1500rpm for 30sec with $NiCl_2 \cdot 6H_2O$ (99.999%) or $HAuCl_4 \cdot 3H_2O$ solution (solution concentrations vary from 0.001 M to 0.1 M, Figure 3.2).

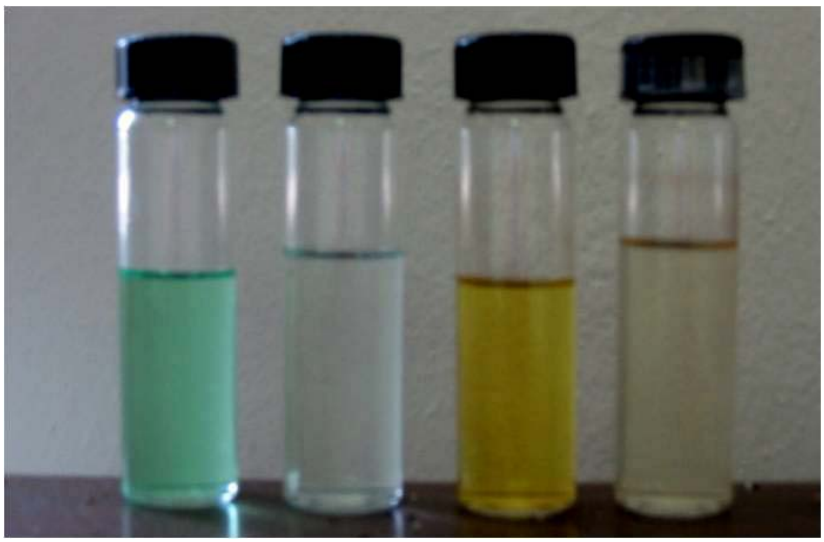

Figure 3.2 As-prepared metal catalyst solutions, from left to right: $NiCl_2 \cdot 6H_2O$ (0.1 M), $NiCl_2 \cdot 6H_2O$ (0.01 M), $HAuCl_4 \cdot 3H_2O$ (0.01 M), $HAuCl_4 \cdot 3H_2O$ (0.001 M).

Different kinds of substrates have different lattice mismatch values, which will directly affect the morphology of ZnO nanostructures and the growth parameters. Table 3.1 lists the lattice mismatch of different substrates with respect to ZnO. [86] There are four basic procedures for catalyst-assisted VLS synthesis of ZnO nanostructures: (1) $NiCl_2 \cdot 6H_2O$ or $HAuCl_4 \cdot 3H_2O$ ethanol solution is spinned coating onto a Si (100) wafer in order to originate a thin liquid film of catalyst solution on the substrate; (2) $NiCl_2 \cdot 6H_2O$ or $HAuCl_4 \cdot 3H_2O$ is thermally decomposed to form Ni or Au nanoparticles *via* the Ostwald ripening process while the furnace heats up to 450-500^oC [87] ;(3) Islands can be made of eutectic metal-Si alloy droplets with diameters of tens of nanometers [88]; (4) As the temperature is ramped above 420°C, Zn powder starts to vaporize around the Si

substrates; and then preferentially adsorbs and condenses onto the Ni or Au nanoparticles. The metal catalysts are used to reduce the surface free energy and enhance the ZnO growth for VLS process. The formation of eutectic alloy droplets occurs at each catalyst site, followed by the nucleation and growth of crystalline ZnO nanowire due to the supersaturation of the liquid droplet. The ZnO will preferentially grow along c axis due to the faster growth rate and lower surface energy than the other directions. Incremental growth of ZnO nanowires taking place at the droplet interface constantly pushes the catalyst particles upwards. Figure 3.3 shows the four procedures of VLS growth. [84] If the catalyst is not applied during the deposition, instead of a VLS process, the ZnO growth follows a Vapor-Solid (VS) process of which the zinc vapor and oxygen directly deposited onto the substrate to form ZnO crystals. [89] VS process usually synthesis a rich variety of nanostructures, including nanowires, nanorods, nanobelts and other complex structures, because it has poor morphology control and reproducibility.

Table 3.1 Lattice parameter of several epitaxy substrates. [84]

Material	ZnO	GaN	Sapphire	SiC	Si
Crystal structure	Wurtzite	Wurtzite	Hexagonal	Wurtzite	Diamond
Lattice constant (nm)	a=0.325 c=0.521	a=0.319 c=0.519	a=0.475 c=1.229	a=0.309 c=1.512	a=b=c=0.543
Epitaxial plane	(0001)	(0001)	$(11\bar{2}0)$	(0001)	(100)
Lattice mismatch	0	1.9%	0.08%	5.5%	18.6%

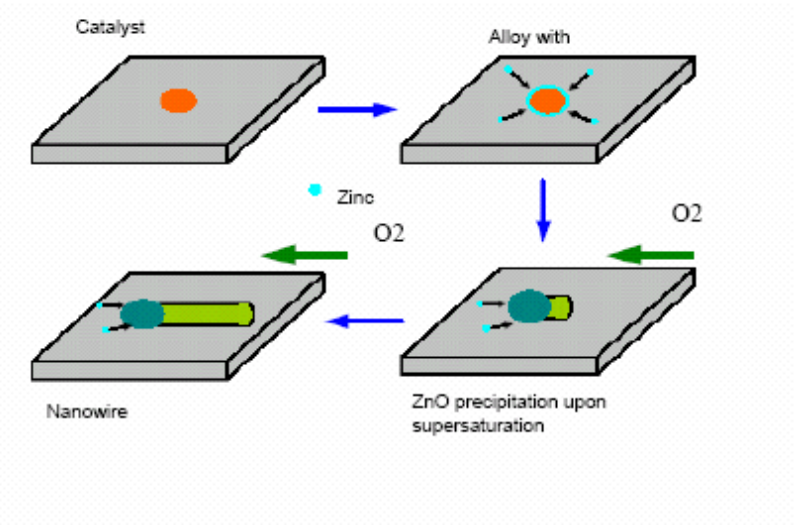

Figure 3.3 Schematic of ZnO nanowire growth by VLS process. [84]

For epitaxial growth, an ultra thin layer (approximately 20-30nm) of ZnO film was deposited onto pure cleaned ITO substrates by radio frequency (RF) magnetron sputtering at room temperature. A pure ZnO (99.999%) target was bombarded by reactive ions species that are ionized from the feeding gases of argon (Ar) and oxygen (O_2) and consequently deposit ZnO on the substrates. The deposition pressure is sustained under 8 mTorr with the gas mixture of Ar and O_2, and the gas flow rates are 33sccm and 11sccm, respectively. A thin layer of ZnO film generates more preferential and uniform nucleation sites for ZnO nanostructures growth. [90] A thin ZnO film is important for some optoelectronic device applications such as dye-sensitized solar cells (DSSCs) since this metal oxide film can greatly eliminate the charge recombination between the photo-generated free electron and the positive ion from the ITO substrate which will decrease the performance of the DSSCs. All the as-sputtered samples were cleaned in the pure methanol ultrasonic bath for 10 minutes followed by immersing the samples in the Zn

powder diluted methanol ultrasonic bath for another 30 minutes. The purpose for the Zn powder seeding is to further enhance the uniformity of first stage nucleation sites.

All the as-prepared samples are loaded on top of an alumina boat with a certain amount of Zn powder underneath it. Additionally, another smaller alumina boat containing very little amount of Zn powder was firstly inserted into the end of the smaller quartz tube before loading the samples. The small quartz tube was inserted into the center zone of the quartz tube furnace. Prior to the deposition of ZnO nanostructures, the reactor tube was pumped down to vacuum of 50 mTorr, and then purged with Argon gas. The temperature of the quartz tube was raised to 500ºC with the elevating temperature rate of 5ºC/min. Another homemade thermocouple feedthrough is inserted into the furnace with contact at the front of the small quartz tube in order to precisely measure the reaction teamperature. The pressure in the quartz can be controlled by a manually throttle valve or an automated exhaust valve controller (butterfly valve), which is connected to a mechanical pump, and a pressure gauge. Ar (carrier gas) and O_2 (reactant gas) are fed into the tube precisely using mass flow controllers to control the amount of the gas flow rate. Figure 3.4 is the schematic diagram of the DSDT system.

The temperature ramping rate cannot be too large since the melting temperature of the ITO glass slide is approximately 550-580ºC. ZnO nanostrucutres growth using thermal CVD method has been rarely reported due to the low melting point of the ITO glass substrate. Ar, served as the carrier gas, is firstly fed into the quartz tube when the temperature of the furnace exceedd the melting point of the Zn powder (419ºC).

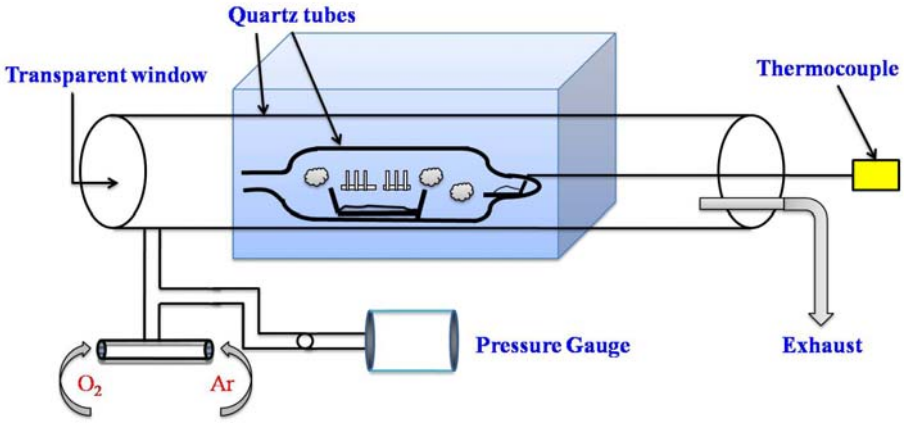

Figure 3.4 Schematic diagram of the thermal CVD growth system.

O_2, served as the reactant gas, is fed into the quartz tube 1 minute after the Ar is fed. Ar is firstly fed into the tube in order to generate supersaturated Zn vapor environment in the inner quartz tube. This allows the local Zn vapor above the ITO substrates to reach a quasi-equilibrium state before the O_2 is fed. The local Zn vapor pressure surrounding the substrates is an important key factor for synthesizing uniform and well-controlled morphology. The deposition of ZnO may take place along the entire length of the quartz tube, and white fluffy coatings were often found on the tube wall after deposition. Another extra benefit for the DSDT system is that the inner quartz tube can be easily replaced or removed out of the thermal CVD system for cleaning, without disturbing the system or breaking the vacuum sealing. In order to prodeuce different morphologies of ZnO, the flow rate and the relative gas flow rate ratio between the two gases can be tuned as well as tuning other growth parameters like growth pressure, temperature, catalyst, and growth time. Figure 3.5shows a photograph of the thermal CVD system. Precisely control the gas flow rate, temperature, and the duration of oxygen flow are the critical parameters regarding ZnO deposition. If oxygen gas is administrated to feed into the quartz tube too

early in which zinc vapor has not sufficiently formed on the substrate, oxygen gas simply react with zinc powder and the growth process terminates prematurely. Even though the zinc vapor is sufficiently stabilized on the substrate the growth process may also terminates prematurely if the oxygen flow rate is too high. Very little ZnO can be deposited on the substrate in this case, and dark-grey colored of zinc cover with a thin layer of oxidized zinc can be found in the alumina boat. If oxygen gas is fed into the tube too late, zinc powder has already been vaporized and exhausted away. In order to produce well-formed nanostructures, it is important that a small oxygen gas flow rate is used at the initial stage of the growth and the oxygen to argon flow rate ratio should been larger than (8:1) in order to dilute the surge of oxygen flow. A surge of oxygen flow usually results to the overgrowth of the nanostructures into microstructures or the formation of ZnO polycrystalline films; it also reduces the volatility of the zinc source thus making the deposition on substrates more difficult. Thick and dense depositions tend to result in whiter coloration than thin and sparse depositions.

The basic parameters that control all CVD processes are: (1) the rate of the mass transfer of reactant gases from the ambient gas stream to the wafer surface, and (2) the rate of reaction of those gases at the wafer surface. These are sequential processes and the observed deposition rate G is determined as:

$$G = A\frac{1}{\frac{1}{F}+\frac{1}{R}} \quad (1)$$

Figure 3.5 The thermal CVD growth system.

where A is a geometric constant, F is the mass transfer rate and R is the surface reaction rate. In order to achieve uniform deposition, it is necessary to ensure both rate condition are met. The rate of surface reaction depends on reactant gas concentration and temperature. The rate of mass transfer also depends on reactant gas concentration as well as diffusion across the boundary layer. The surface reaction at a given temperature is:

$$R = k_1 C_s \qquad (2)$$

where k_1 is the chemical reaction constant and *Cs* is the concentration of the reactant at the surface. *Cs* is proportional to the partial pressure of the reactant gas and is minimally affected by low pressure deposition. The mass transfer rates are strongly affected by a change in total pressure. The mass transfer rate is defined as:

$$F = (\frac{D}{d})\Delta C \qquad (3)$$

where D is gaseous diffusivity, d is the boundary layer thickness and ΔC is the reactant gas concentration gradient between the surface of wafer and the ambient gas stream. The diffusivity is inversely proportional to total pressure. [91] Nucleation density of ZnO is determined by the activation energy and temperature according to [92],

$$N = A\exp(\frac{-G}{RT}) \qquad (4)$$

here N is the nucleation density, T is growth temperature, $G=G_v+G_s$ is the activation energy of nucleation. G_v is the volume free energy which is related to the oxygen concentration as: $G_V \propto -\ln P(O_2)$. G_s is the surface free energy. Catalytic particles are introduced to change the local curvature on an otherwise flat surface, thus effectively lowering the surface free energy and total activation energy over those locations. On the other hand, the relatively low oxygen concentration in the reactor tube makes G_v the volume free energy fairly large.

The surface morphologies of the samples were estimated by field emission scanning electron microscopy (SEM, JOEL JSM-7000) with chemical analysis of energy dispersive spectrometry (EDS). The crystal structures of the samples were characterized by x-ray diffraction (XRD) using a Rigaku Miniflez powder x-ray diffrectometer of Cu Kα radiation. Room temperature photoluminescence (PL) and micro-Raman spectroscopy were performed using 325 nm and 441.6nm laser line from a He-Cd laser (Kimmon Electric) with a JY spectrometer embedded with 2400 and 3600 groove grating. The laser beam was focused onto a spot of approximately 10 μm in diameter on the sample surface.

Both spectra are collected using a spectrometer with a thermally-cooled charge coupled device (CCD) detector.

3.3 ZnO morphology and its growth mechanisms

A. Structural Characteristics

In order to confirm the structure, growth direction, and the purity of the ZnO film, a thicker ZnO film (approximately 700nm) was sputtered under the same sputter condition what was used to grow the ZnO nanostructures on ITO glass substrate. Figure 3.6 (a) shows a high resolution SEM image of this thicker ZnO thin film with a tilting angle of 30º. Many aggregated ZnO crystals with sizes int the range of 70-100nm can be observed. ZnO crystals first aggregate into a compact thin film and then start to growth in a certain direction.

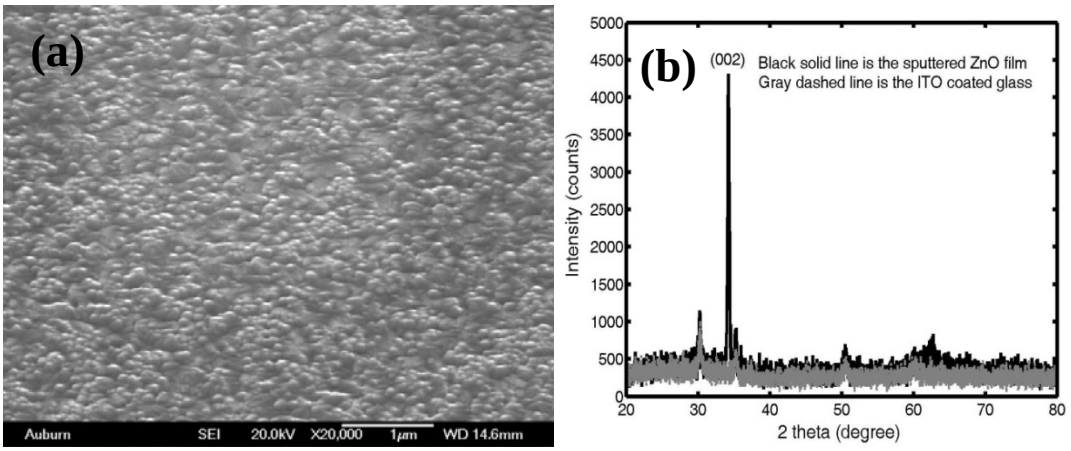

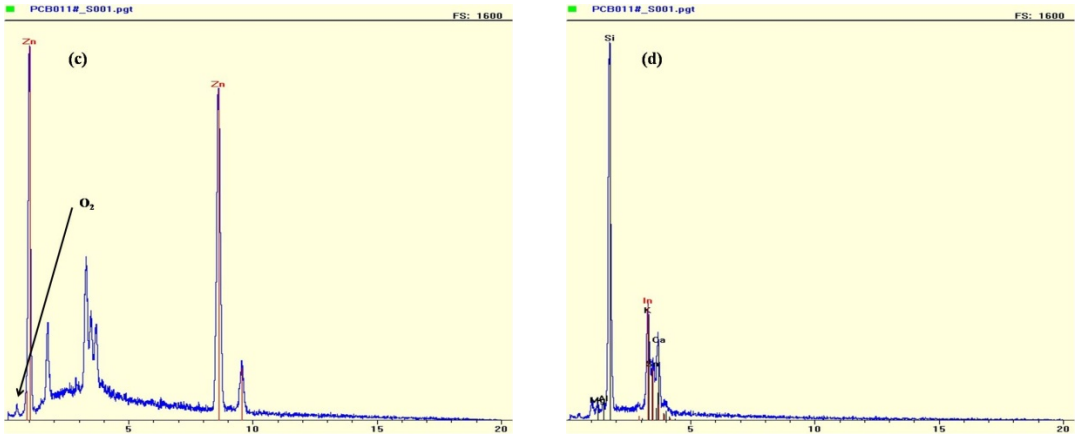

Figure 3.6 (a) SEM image of the as-sputtered ZnO thin film on ITO with a tilting angle of 30º. (b) XRD of the ZnO thin film, black solid line is the ZnO thin film and the gray dashed line is the ITO glass substrate (c) the EDS of the as-sputtered ZnO thin film (d) the EDS of the pure ITO substrate.

The XRD pattern shown in Figure 3.6 (b) confirms our assumption that the ZnO thin film grew in the dominant (002) orientation and a very weak peak between 60º and 70º is a little portion of ZnO crystal in the growth direction of (103). The solid black curve is the ZnO thin film and the dashed gray curve is the commercial bought ITO coated glass substrate. The other background XRD peaks from the ZnO film was originated from the ITO coated glass. Figure 3.6 (c) is the EDS diagnosis of the sputtered ZnO film. Three sharp Zn peaks have been detected with a small peak from the oxygen species. The magnitude of the zinc and oxygen peaks from the EDS results confirmed that ZnO were grew under the oxygen deficient environment. The rest of the background peaks are contributed from the ITO substrate which can be compared with Figure 3.6 (d).

For non-catalyst ZnO growth, the nanostructures are obviously nucleated via self-catalyzed mechanism. [93] A two-step pressure-controlled vapor reflected method allows

the synthesis of self-organized hexagonal crystalline or porous nanowire arrays on the stage of the previously grown nanorods [94]. However, even those sub-nanowires can be vertically synthesized on top of the nanorods; the whole structure including the sub-nanowires and the nanorods have not been reported to be well-aligned. The sub-nanowires were grown on the top facet of the ZnO nanorods which is similar to epitaxial growth process. Due to the greater tolerance in lattice mismatch it is easier to produce well-aligned nanorods.

The SEM photographs of the vertically well-aligned ZnO nanorods grown on top of different substrates without applying any catalyst are shown in Figure 3.7. These substrates are located adjacent to each other at a distance of 2mm on top of the alumina boat. Figure 3.7 (a) shows the SEM image of the well-aligned ZnO nanorods which are grown on top of a ZnO thin film deposited ITO glass substrate. Nanorods are 70-100nm in diameter and approximately 5μm in length. The growth of the nanorods was carried out at a gas pressure of 50 Torr with the Ar and O_2 flow rates of 100 sccm and 10 sccm, respectively. The growth duration is 45 minutes. Figure 3.7 (b) shows a higher density of ZnO nanorods growing on top of a (100) p-type Si wafer. The Si wafer has an ultra thin layer of Zn film sputtered on top of it. The as-prepared Zn thin film/Si wafers were heated at 1 atmosphere pressure in a furnace box at the temperature of 400ºC for 8 hours in air. The purpose of these two processes is to generate an ultra thin Zn film where upon heat up of the substrates, ZnO film would be reinforced to self-crystallize in air. This layer can serve as the seeding layer with more uniform and more highly crystallized nucleation sites for the growth of ZnO nanostructures. The hexagonal shape can be

obviously observed on the surface of the ZnO nanorods with a diameter of 100nm. The cross section of nanorod body is very uniformly distributed without any protuberant branch or feature. Figure 3.7 (c) and (d) are the low and high magnification SEM images of the well-aligned ZnO grown on top of the p-type silicon coated with a ZnO thin film. The shape looks like a nano-wine-bottle with a small cap on it. The smaller ZnO nanorods are grow on top of a ZnO crystal of a size of approximately 300-500 nm, and the large ZnO crystals are originated by the ZnO thin film. All of these aligned nanorods were produced over a large deposition area as shown from the scale bar.

By decreasing the growth gas pressure while keeping all other growth parameters the same, ZnO nanostructure with different kinds of morphologies can be generated. Figure 3.8 show the SEM images of 2D ZnO nanostructures synthesized on an ITO coated glass substrates at a lower growth pressure of 35 Torr. In Figure 3.8(a) and (b), 2D ZnO nanoplants with very sharp cactiformis tip arrays can be clearly observed.

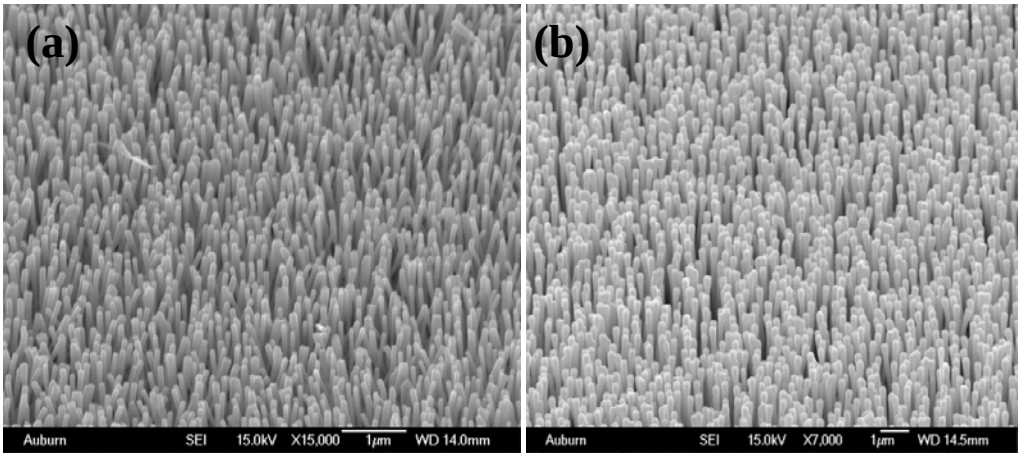

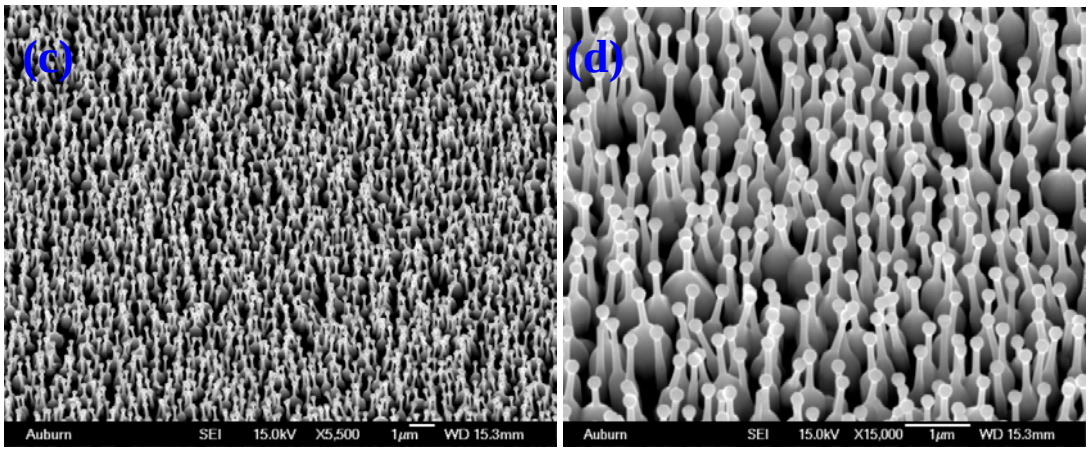

Figure3.7 (a) SEM image of vertically well-aligned ZnO nanorods grow on ITO substrate; (b) SEM image of vertically well-aligned ZnO nanorods grow on p-type silicon substrate with sputtered Zn thin film; (c) and (d) are low and high magnification SEM images of the well-aligned ZnO nano-wine bottle grown on top of the p-type silicon sputter coated with a ZnO thin film.

The tips of these nanoplants are approximately 50nm in diameter. The whole structure of the ZnO nanoplant is grown on top of a ZnO crystal and the end of the nanorod was sharpened into a tip shape due to the lower growth gas pressure and the suddenly terminated growth condition. The XRD result in Figure 3.8(c) reveals that the ZnO nanoplants have a fairly good crystal property with high crystallinity and typical wurtzite structure. The XRD result confirms our interpretation that the ZnO nanoplants have a dominant growth direction along the (002), and are also grown on top of the (002) face of ZnO crystal. The rest of the XRD peaks, such as (110), (103), and (004) should be contributed by tips of the nanoplants which extend in different directions. The nanoblooms structure in Figure 3.9(a) is grown under the same condition as the nanoplants structure. The SEM image in Figure 3.9(b) shows a similar nanopins structure

grown on top of the nanorod surface as Figure 3.8(b) with approximately the same tip dimensions but a smaller base stage of nanorod. The XRD result shows very consistent results compared to the XRD of Figure 3.8. These two sets of SEM pictures reveal that this specific growth setup method allows a highly precise and higher reproducible growth of 2D ZnO nanostructure arrays.

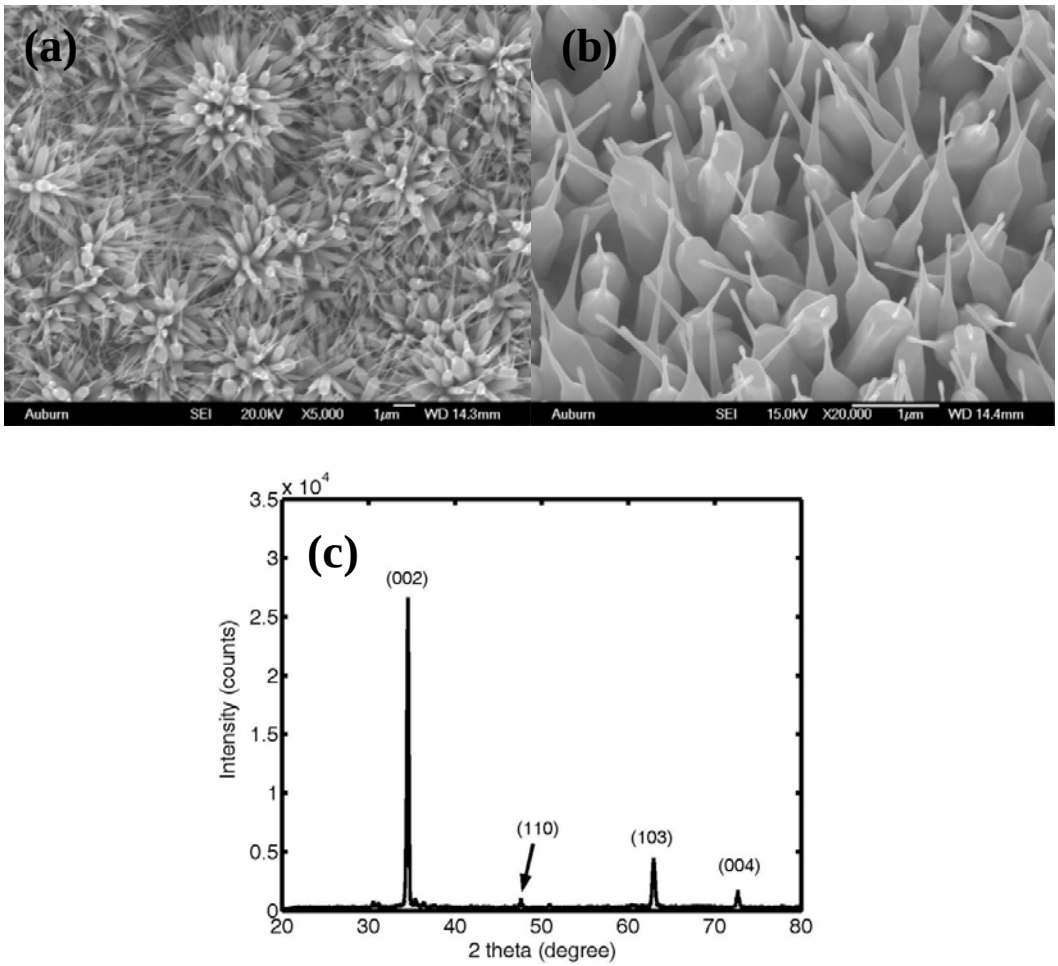

Figure3.8 (a) Low magnification SEM image of ZnO nanoplants with cactiformis tip arrays (b) High magnification of ZnO nanoplant (c) XRD results of ZnO nanoplant having a dominant peak at (002).

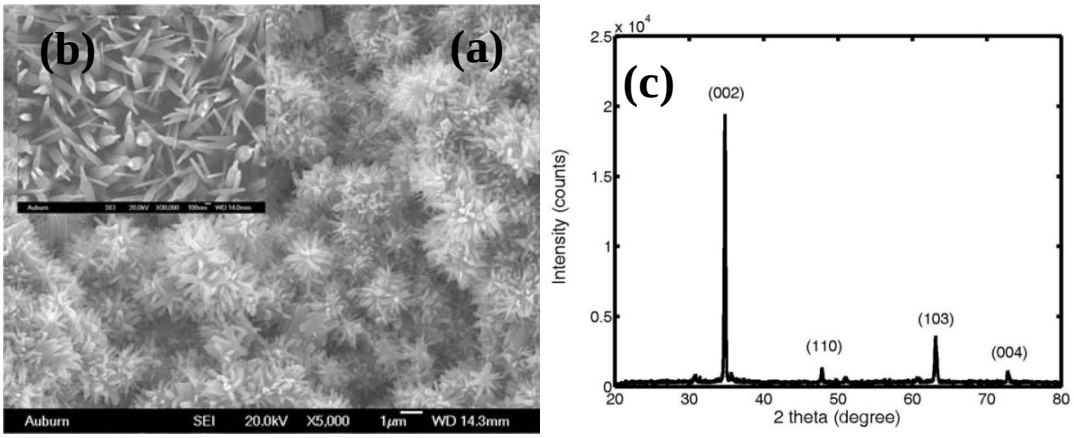

Figure 3.9 (a) Low magnification SEM image of ZnO nanobloom arrays (b) High magnification of ZnO nanobloom (d) XRD results of the ZnO nanobloom which has a dominant peak at (002).

If the growth pressure was decreased down to 25 Torr with all the other growth parameters held constant, ZnO with a needle-like structure can be synthesized. A large area of 2D ZnO nanoneedles is directly grown on top of the ZnO crystal as shown in Figure 3.10(a). It would be more difficult to control the ZnO nanostructures and the growth direction due to the lower growth pressure which correspond to a lower concentration of local ZnO vapor in the smaller quartz. The lower growth pressure will also cause a more intensive fluctuation and turbulence in the grown zone inside the CVD reactor as compared to the growth at a higher pressure. The local ZnO vapor in the small tube is also more difficult to reach a supersaturated state. Figure 3.10(b) shows that the ZnO nanoneedles have the tip size of approximately 35-40 nm in diameter, which is smaller than the tips synthesized under 35 Torr or higher gas pressures. Even though the XRD shown in Figure 3.10(c) shows the same peaks as that for ZnO grown at 35 Torr, the crsytallinity worsens while the intensity of the XRD peaks decreases. XRD data

reveals more random growth directions for ZnO nanostructures protroding out from the (110) and (103) crystal faces as compared to growth at higher pressures. The XRD shown in Figure 3.10(c) also insets the XRD curve of the ITO coated glass substrate, which can explicitly explain the background peaks generate from the ZnO nanoneedles. If the growth pressure was decreased further down to 15 Torr the growth of ZnO nanostructure arrays would be even more difficult. The uniformity and reproducibility will dramatically decrease as well as the crystallinity. The SEM of ZnO growth under 15 Torr (not shown) shows a smaller tip size of approximately 25-30nm. Sparse ZnO nanoneedles are grown on the ZnO crystals and the XRD shows worse results with lower count intensity and broader rocking curve corresponding to each peak position which is due to the lower growth pressure.

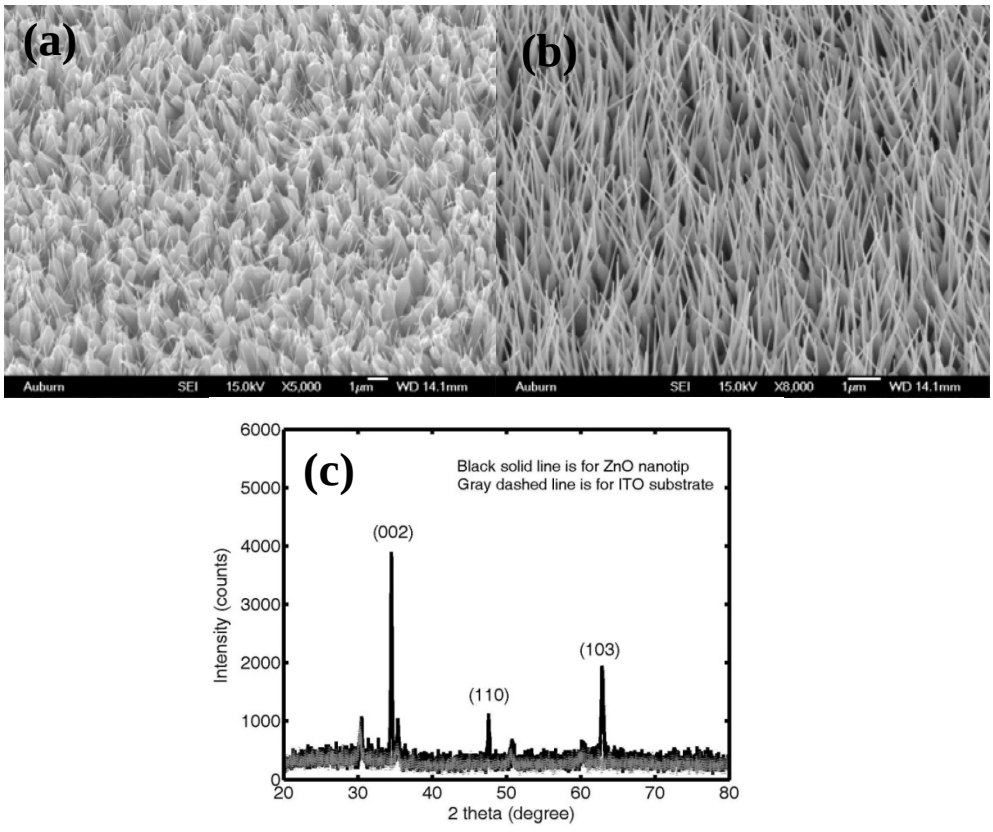

Figure3.10 (a) Low magnification SEM image of ZnO nanotip arrays with a tilting angle of 30º; (b) High magnification SEM of ZnO nanotips; (c) XRD of the ZnO nanotip arrays, black solid line is the ZnO nanotip arrays and the gray dashed line is the ITO glass substrate.

Since it is more difficult to control the growth morphology of ZnO at the pressure lower than 25Torr, two different kinds of metal catalysts, gold (Au) and nickel (Ni), are applied in order to lower the surface energy and enhance the growth of ZnO nanostructures at lower growth pressure. Figure 3.11 shows the result of applying Au catalyst to growth at a pressure of 15 Torr. The flow rate of Ar and O_2 were set to 100-105sccm and 7-10 sccm, respectively. 2D inverse nanotetrapods arrays morphology is displayed in Figure 3.11(a) & (b). The tips of the inverse nanotetrapods have an average size of 100nm with very uniform distribution. The XRD data shown in Figure 3.11(c) shows the inverse nanotetrapods each with three branches extending out uniformly in the (101), (102), and (103) directions. The (002) direction remains the dominant stem direction for these ZnO nanotetrapods. According to the results from the SEM images and the XRD data, these ZnO nanotetrapods structures are grown in the main arbor of (002) direction and equally spreading out in three directions with approximately the same length. An EDS spectrum analysis shown in Figure 3.11(d) has three main peaks of Zn element and a relatively small peak of oxygen, which is very reasonable due to the oxygen deficient growth environment, with the Ar to O_2 ratio being higher than 10:1. The other peaks in the EDS spectrum were generated from the ITO coated substrate.

High density and vertically well-aligned ZnO nanonails structures have been synthesized by applying liquid Ni metal catalyst under the same growth condition as the inverse ZnO nanotetrapod. The SEM image in Figure 3.12(a) shows a top view of the ZnO nanonail. The ZnO nanonail structure can be observed in Figure 3.12(b) by tilting the sample an angle of 30º.

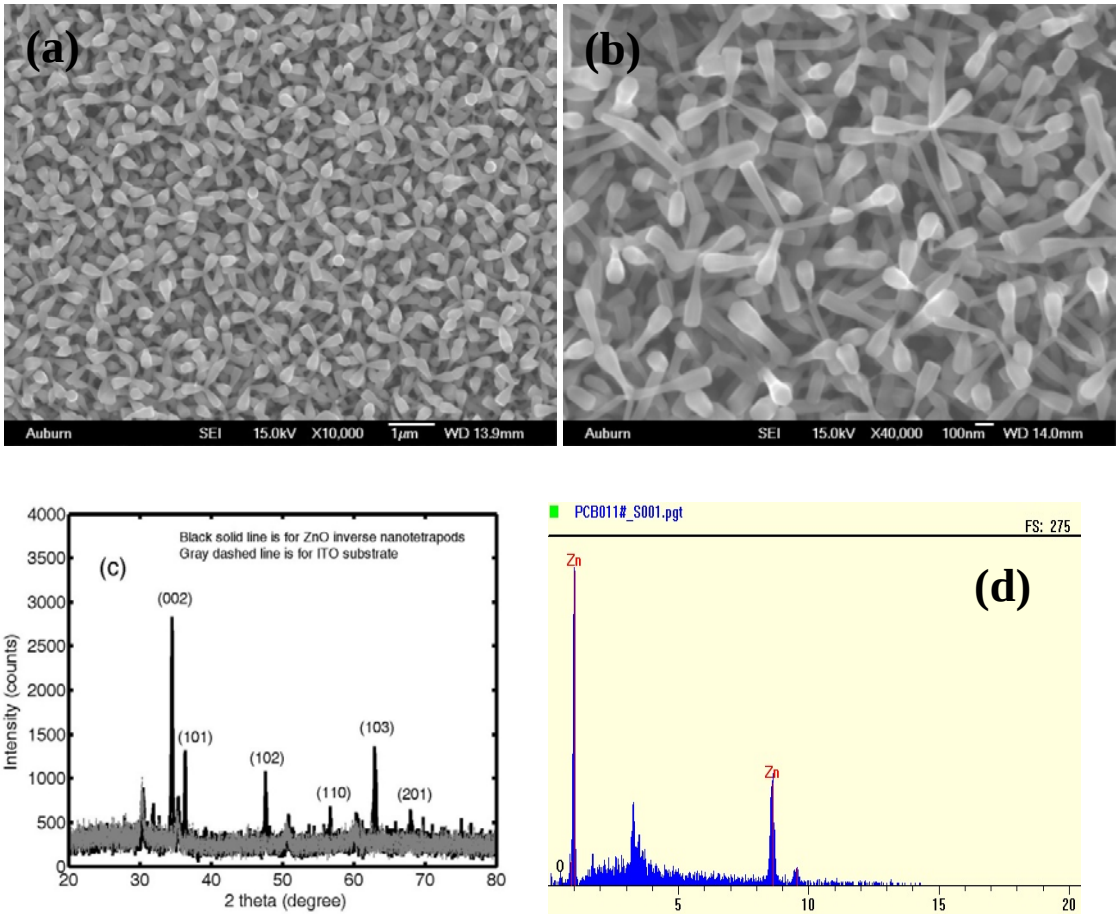

Figure3.11 (a) Low magnification SEM image of inverse ZnO nanotetrapod arrays (b) High magnification SEM image of inverse ZnO nanotetrapod arrays (c) XRD of the inverse ZnO nanotetrapod (d) EDS of the ZnO nanotetrapod.

It is apparently in Figure 3.12(b) that the hexagonal shape of well-aligned ZnO nanonails with a height of ~5μm was grown on top of the ZnO crystals. A highly single crystalline wurtzite structure with one dominant peak (002) is explicated by the XRD in Figure 3.12(c). The (004) and (002) peaks are in phase and the only extra peak is the very little small peak of (103) which is due to the sputtered ZnO thin film being crystallized at high temperature. Therefore, the 2D ZnO nanonail arrays are extremely well-aligned.

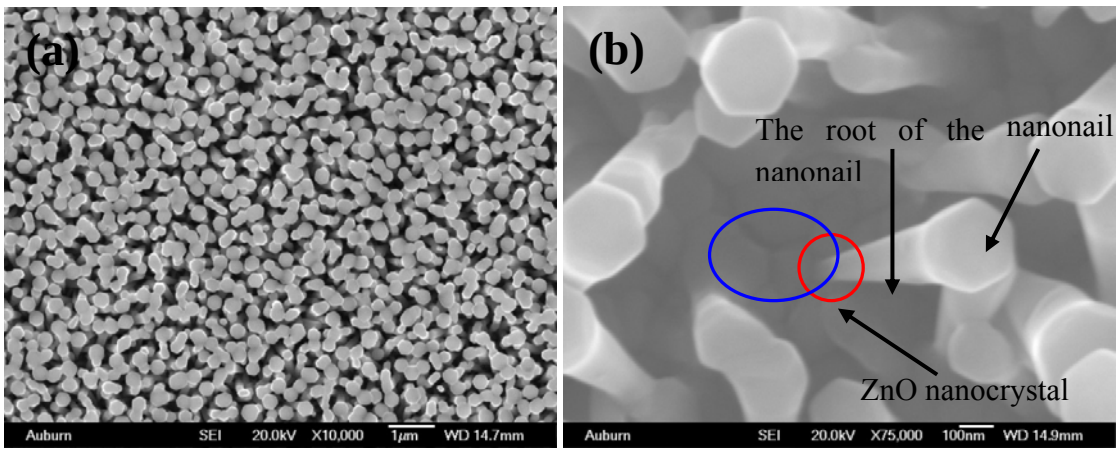

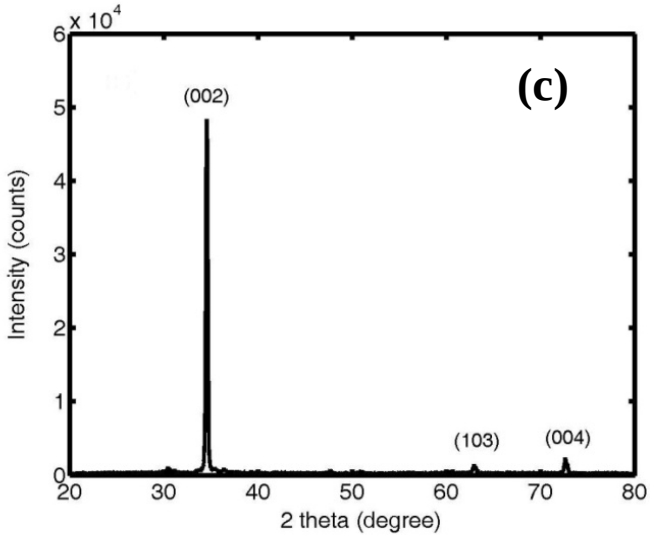

Figure 3.12 (a) SEM image of the top view vertically well-aligned ZnO nanonails (b) side view of the ZnO nanonails with a tilting angle of 30º (c) XRD of the well-aligned ZnO nanonails.

Figure 3.13 shows the well-aligned ZnO nanorods synthesized by applying Ni catalyst at the growth pressure of 35 Torr. A high magnification SEM image in Figure 3.13(b) shows the evenly distributed nanorods of the size approximately 70-100nm. The side view of ZnO nanorods in Figure 3.13(c) shows that the ZnO nanorods always grow vertically with respect to the ITO substrate. The red frame in Figure 3.13(c) shows that the well-aligned ZnO nanorods start to grow in a manner that follows the countour along the edge of the substrate. The XRD also reveals ZnO nanorods were grown in vertically-aligned direction with high crystallinity in Figure 3.13 (d). The (002) peak shows an intensity higher than one hundred thousand while the (103) peak has mostly been depressed. This indicates how aligned the ZnO nanorods are.

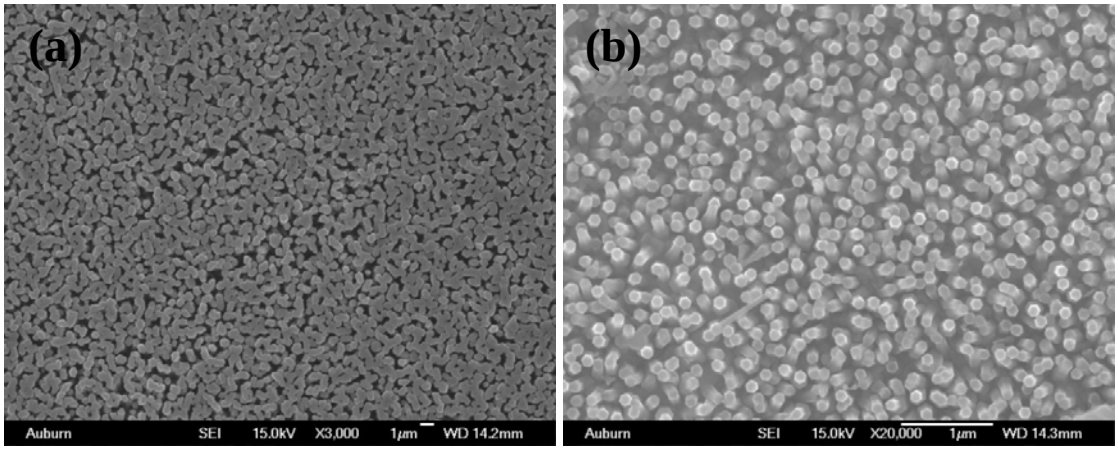

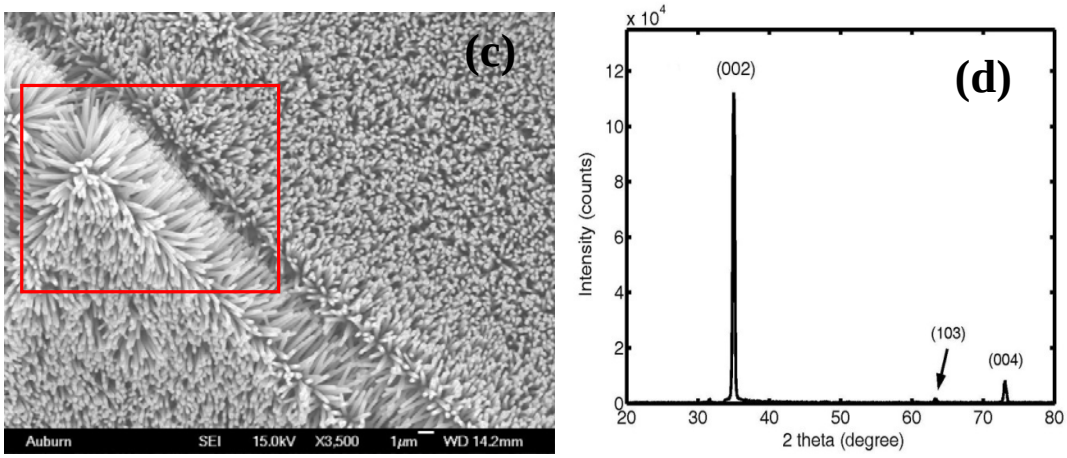

Figure3.13 (a) SEM image of the top view vertically well-aligned ZnO nanorods (b) higher magnification of the ZnO nanrods (c) corner view of the vertically well-aligned ZnO nanorods. (d) XRD of the vertically well-aligned ZnO nanorods.

The systematic morphology and corresponding XRD flow charts are shown in Figure 3.14(a) & (b). First, vertically well-aligned nanorod arrays are synthesized at 50 Torr using noncatalyst growth method. (002) and (004) are the only peaks that have been collected for this nanorods sample. As the growth pressure decreases to 35 Torr, the tip size of the ZnO nanostructure decreases from 100nm to 50nm while the nanoflower feature is created. Two more XRD peaks, (110) and (103), show up in the nanoflower morphology. At 25 Torr even though a sharper tip (approximately 35nm) can be generated, these tips start to grow randomly from the substrate while their density dramatically decreases as compared to the growth of aligned nanorods at 50 Torr. The relative peak intensity at (002) and (103) increased from less than 0.01 (aligned nanorod) to 0.16 (nanoflower) and then up to 0.5 for the quasi-aligned nanotip of these noncatalyst growth features by decreasing the growth pressure. As shown by the morphology and XRD chart for noncatalyst growth, the crystal quality decreases and the tip becomes

sharpter with decreasing growth pressure. Metal catalysts were added in order to enhance the growth at lower growth pressure. After applying Au and Ni catalysts, aligned inverse nanotetrapods and aligned nanonails have been produced at 15 Torr. The density of the ZnO features increases with the crystallinity after applying the metal catalyst for low pressure growth. The relative peak intensities of (002) and (103) decreases to 0.01 as compared to noncatalyst growth at the same growth conditions.

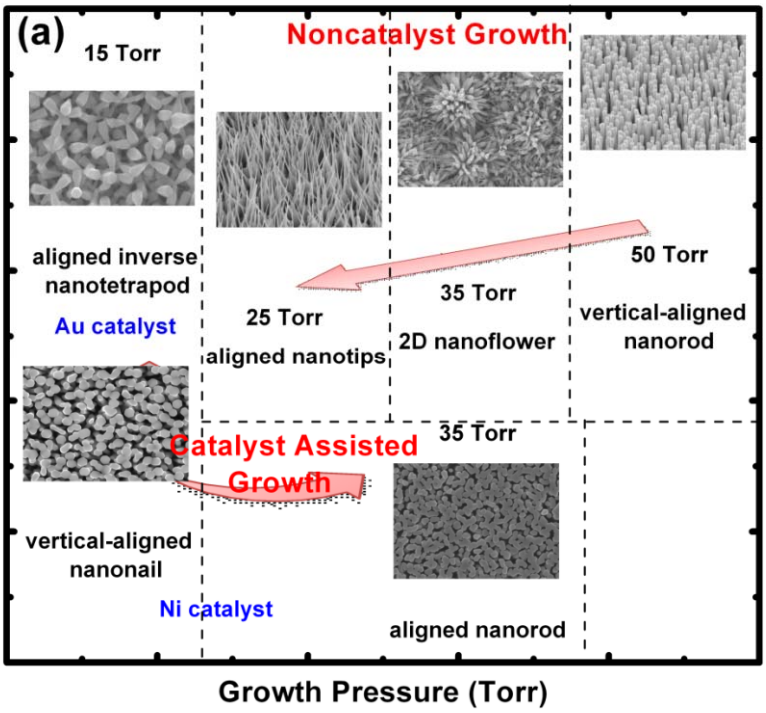

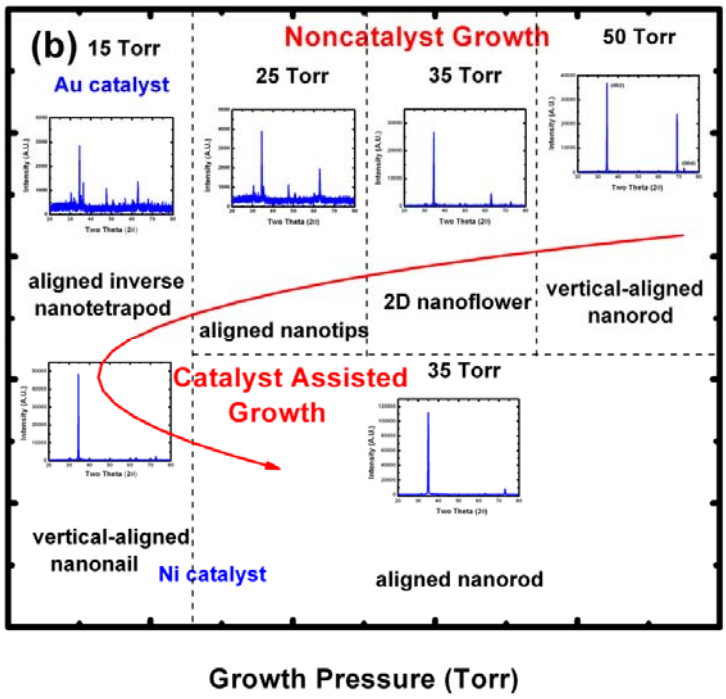

Figure 3.14 (a) Morphology flow chart of ZnO nanostructure with varying growth pressure and catalyst supplement. (b) XRD flowing chart of ZnO nanostructure with varying growth pressure and catalyst supplement.

B. Growth Mechanism

The growth mechanism of the ZnO nanostructure arrays can be explained based on growth parameters which are divided into two catalogs. The first part is the growth environments including dimensional of the smaller quartz tube, the carrier and the reactant gases, the gas flow rates, the ratio of growth rate between the two gases, and the

growth pressure. The second part includes the type of substrates for ZnO growth, such as ZnO/ITO, ZnO/Si, Zn/Si, the type of catalyst/noncatalyst, and the growth stages etc.

The first part can be clearly described by Figure 3.15(a). The actual geometry of the ZnO growth inner tube is shown in Figure 3.15 (b). The substrates are placed side by side with a separation of approximately 2mm on top of the alumina boat. Another small alumina boat containing a minute amount of Zn powder is inserted into the end of the quartz tube, which has a specifically designed dimension as shown in Figure 3.15(a). As the furnace temperature is elevated to the melting point of Zn powder, Zn vapor starts to form and diffuse out from the alumina boats. The Zn vapor diffuses upward (as indicates by the two bending gray arrows) and then spreads out from the large alumina boat towads the substrates placed on top of it. Another group of Zn vapor from the smaller alumina boat starts to diffuse toward the opened-end of the quartz tube (diffusing leftward). The arrows in Figure 3.15(a) indicate the directions of the Zn vapor flow. Therefore, the space above the substrates will quickly reach the Zn vapor quasi-equilibrium supersaturated state after the carrier gas Ar is introduced. One minute after Ar is introduced O_2 is also fed into the quartz tube. The O_2 will be decomposed and react with the Zn vapor at the region above the substrates. Ar and O_2 are fed into the tube with the flow direction toward the end of the tubes (rightward as indicated by the arrows). The Zn vapor generated from the small alumina boat at the end of the quartz tube will possess a much higher Zn concentration than the large alumina boat since the decomposed oxygen immediately reacts with the Zn vapor which is closed to the open end of the tube. Therefore, the Zn vapor generated from the small alumina has an opposite flow direction

to the flow of Ar and O_2. These two groups of flowing gases will oppose each other at a certain location near the two ends of the substrates. As these two groups of gases meet each other, a vertical gas flow direction will be generated in order to reach a balance point between these two groups of gases.

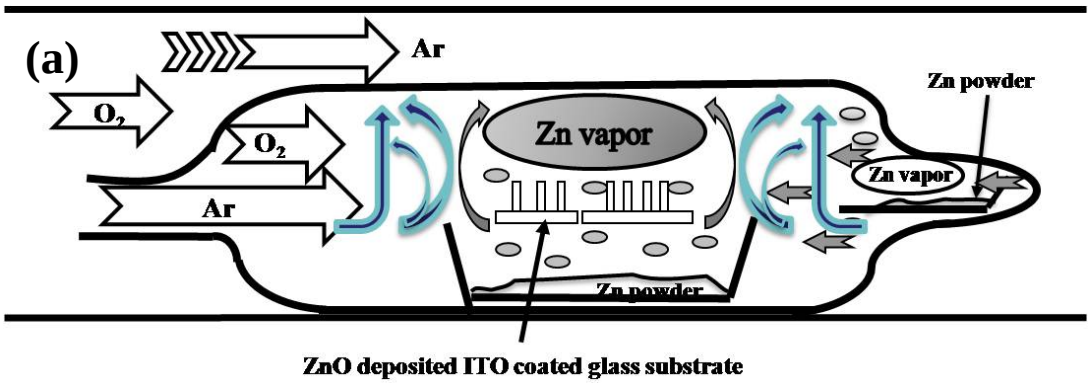

Figure3.15 (a) Schematic interpretation of the gas flow dynamic in the DSDT setup for ZnO nanostructures growth (b) actual geometry of the ZnO growth inner tube.

The two vertical bending arrows (as indicates by the two bending bluish arrows) at both sides of the substrates are used to indicate the other gas flow direction created by these two groups of gases. The ZnO nanostructures will be reasonably confined to physically grow in the vertical direction due to vertical flow condition at this location. Wang *et al.* reported using the vapor-reflected growth method in order to enhance the surface diffusion in the lateral direction with respect to the vertical direction by the

increased of convection. [92] However, in our custom specific setup, the ZnO vapor can reach a quasi-equilibrium state just above the substrates and thus ZnO structures can be confined to grow vertically against the substrates instead of laterally when using vapor-reflected growth method. The vapor-reflected growth method also demands a continuously dynamic gas flow and will be hard to control. Based on this DSDT growth method many different kinds of 2D ZnO nanostructured arrays can be synthesized with high crystallinity and high reproducibility onto different substrates.

Figure 3.16 is depicts the second part of the growth mechanism. For catalyst-assisted growth the ZnO growth mechanism is similar to vapor-liquid-solid (VLS) mechanism. VLS method can be found elsewhere. [95] For non-catalyst ZnO growth, ZnO nucleates via self-catalyzed mechanisms. [91] The glass ITO substrate was first coated with a thin layer of ZnO in order to minimize the lattice mismatch factor and generate uniform ZnO growth as shown in Figure 3.16(a). The as-sputtered ZnO/ITO substrate is immersed into the Zn powder diluted methanol ultrasonic bath in order to enhance the uniform nucleation sites. Figure 3.16(b) shows that Zn nanoparticles reside onto the ZnO/ITO substrate after the seeding procedure. The as-prepared samples are loaded into the furnace with the temperature being increased slowly. The sputtered ZnO thin film would start to crystallize, nucleate and then break/aggregate into small ZnO inlands due to the elevating temperature. Figure 3.16(c) reveals that the ZnO film nucleates first, and then Zn nanoparticles beside it start to melt as the furnace temperature is raised above the melting point of Zn. Simultaneously, Zn powder in the alumina boats would vaporize and reach the Zn vapor supersaturated condition at the region above the substrates. In Figure

3.16(d), as O_2 was fed into the tube, it reacts with the melting Zn nanoparticles and would directly create the first initial growth stages for ZnO nanostructure. Incremental growth of ZnO nanostructures takes place at the Zn melting nanoparticles interface and continuously pushes the Zn melting nanoparticles upward. Figure 3.16(e) shows ZnO nanostructures continually to grow as the furnace temperature rises to 500ºC. The structural formation of the hexagonal prismatic shape of ZnO rod-like crystals can be carried out by the different growth rates of various growth facets, following the sequence of $[0001] > [10\bar{1}1] > [10\bar{1}0]$. [96] Surface diffusion process is the most important rate-limiting step in the ZnO growth. The (0001) plane can easily disappear and be replaced by faces of higher Miller indices that possess lower specific surface energy to form a common tip. However, based on our DSDT setup the convection may enhance the lateral surface diffusion while also physically confining the growth along the vertical direction. Therefore, the (0001) planes are the favorably facets which remain without $[10\bar{1}1]$ after growth.

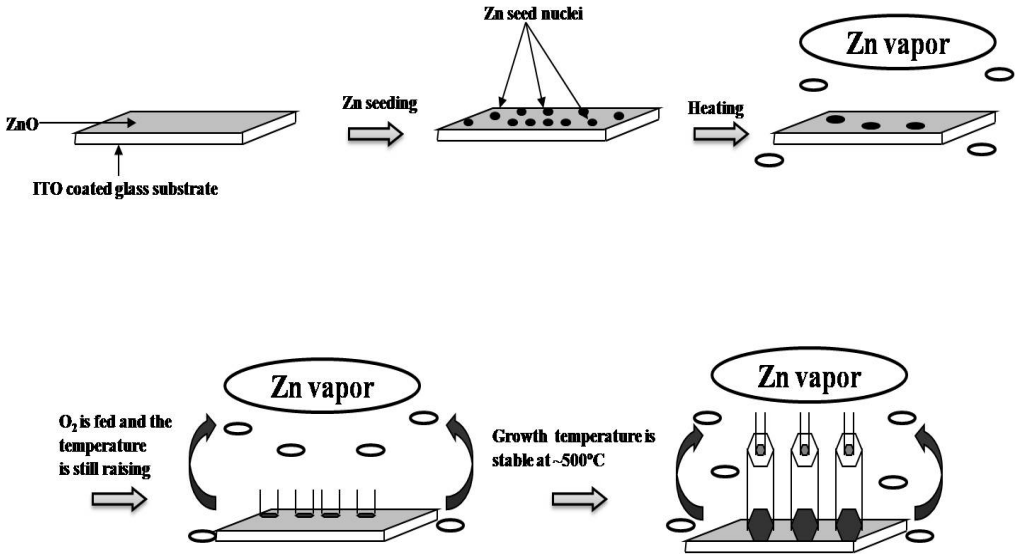

Figure 3.16 Growth mechanisms of the ZnO nanostructures (a) the as-sputtered ZnO/ITO glass substrate (b) Zn nanoparticles reside on top of the ZnO/ITO glass substrate by immersing it into Zn powder diluted methanol ultrasonic bath. (c) Zn nanoparticles start to melt and the Zn powder in the alumina boats start to vaporize when the furnace temperature rise above the melting point of Zn. (d) Oxygen was fed into the tube, the decompose oxygen species would recombine with Zn vapor to form ZnO nanostructures. (e) ZnO nanostructures were formed and tips are generated on top of the nanorods.

Even though plenty of different ZnO nanostructures morphologies can be successfully synthesized, they all share a common feature: all morphologies display a certain degree of axial symmetry (Figure 3.17). The symmetry axis of the ZnO crystal is the c-axis (0001), the ZnO nanostructures preferentially grow along this direction. The shape of the nanostructures is determined by the growth rate in the c-plane with respect to that along the c-axis at different growth stages. A uniform growth rate over the entire growth period will result in a rod-like structure with uniform cross-section. The diameter of the rod primarily depends on the size of the catalyst alloy droplet (in VLS process), while the aspect ratio of the rod depends on the relative growth rate perpendicular to and parallel to the c-axis respectively.

More complicated morphologies such tripods, tetrapods, comb-like structures and irregular branching structures can be broken down into smaller and simpler constituent structures. Figure 3.17(e) shows a certain growth route for a tetrapod structure of ZnO. The tetrapod structure has the main stem growth in the direction along (0001) (pointing out the paper), and three sub-branches extending away from (0001). This can be clearly

observed in the SEM images of Figure 3.11. ZnO nanostructures such as nanorings, helical nanosprings, nanobows, and etc. have been reported. [97, 98, 99] These nanostructures do not have a well-defined symmetry axis nor do they have any symmetry axis other than the c-axis of the crystal. Nevertheless, the c-axis is still the preferred growth direction for these nanostructures; their special shapes are formed by bending and twisting the c-axis so as to relieve the residual strain in the material structure. No such structures were synthesized using our thermal CVD system.

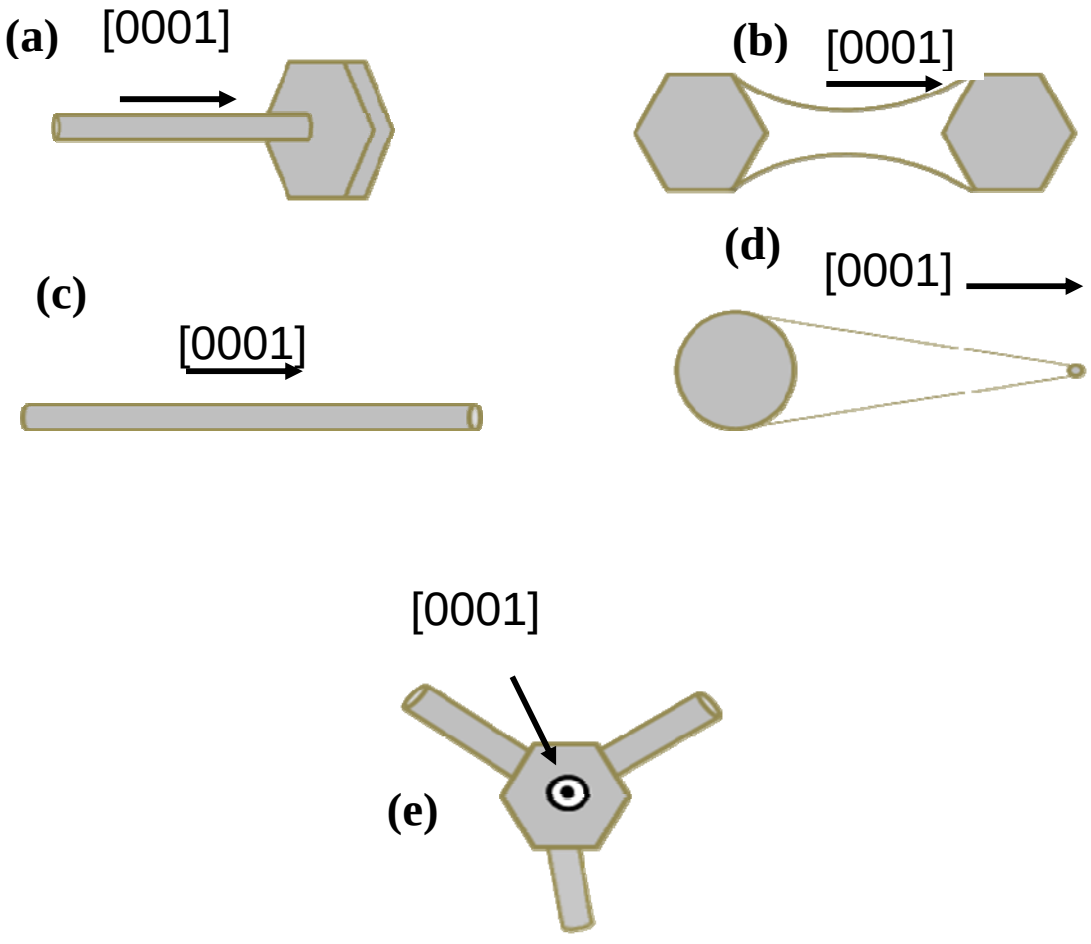

Figure 3.17 Schematic diagrams of several of the most common ZnO nanostructures synthesized by a thermal CVD system: (a) nanonail, (b) nanobone, (c) nanorod, (d) nanoneedles (nanotip), (e) nanotetrapod.

3.4 Photoluminescence Spectroscopy of ZnO Nanostructures

Both 325 nm line (20 mW) and 441.6 nm line (80 mW) from a He-Cd laser (Kimmom) were utilized to collect ZnO nanostrcutures' room temperature photoluminescence (PL) spectra. PL spectra was collected using a spectrometer (JY-Triax550) embedded with two 3-inch holographic gratings (2400 lines/mm, 3600 lines/mm), and a thermoelectrically-cooled charge coupled device (CCD) detector (2048 × 512 pixels). The resolution for 2400 and 3600 groove gratings are 0.775nm/mm and 0.516nm/mm, respectively. The UV laser beam was focused onto a spot approximately 10 μm in diameter on the sample surface using a ×27 lens (N.A.=0.4), which is typically the solid state micro-Raman setting. The spectra resolution of the system is approximately 0.1nm. A neutral density filter, within a range of 0.1%-20%, is located in front of the laser existence in order to reduce the laser intensity. The PL spectrums collected should be recognized as an ensemble spectra composed of several tens to several hundreds of nanostructures. The room temperature PL spectrums of ZnO nanostructures synthesized by the thermal CVD system are shown in Figure 3.18. These two spectrums are collected from two different samples deposited using the same growth conditions. Both spectrums have a near-band-edge (NBE) emission peak at about 3.21 eV (380nm) and a broad blue-green visible emission band at about 2.48 eV (450-500nm). The NBE emission is mostly due to the

excitonic transitions from the valence band to the conduction band, while the blue-green emission is due to electronic transitions between defect states like oxygen vacancies.

Broad visible emission bands may exist at the longer wavelength side of the blue-green emission band, but their intensity is weaker than that of the blue-green band. The FWHM of the NBE is about 0.1 eV. The peak of NBE is consisted of many emission lines and their longitudinal-phonon replica which cannot be resolved by room temperature PL spectrum. A relatively broad and homogenous NBE peak collected by room temperature PL is primary caused by a strong exciton-LO phonon coupling. Therefore, the FWHM of the NBE peak bears little indications on the quality of ZnO crystals.

The quantum confinement effect was not considered because the sizes of the ZnO nanostructures studied in this work are much larger than what is needed for quantum confinement effect to take place. Therefore, the inhomogeneous broadening in the luminescence bands due to the size variations in the nanostructures probed can be discarded.

The major difference of these two spectrums in Figure 3.18 is the relative intensity between the UV NBE emission peak and the blue-green band. It is found that these two samples have a similar size and morphology but the relative peak intensity of PL spectrum varied significantly.

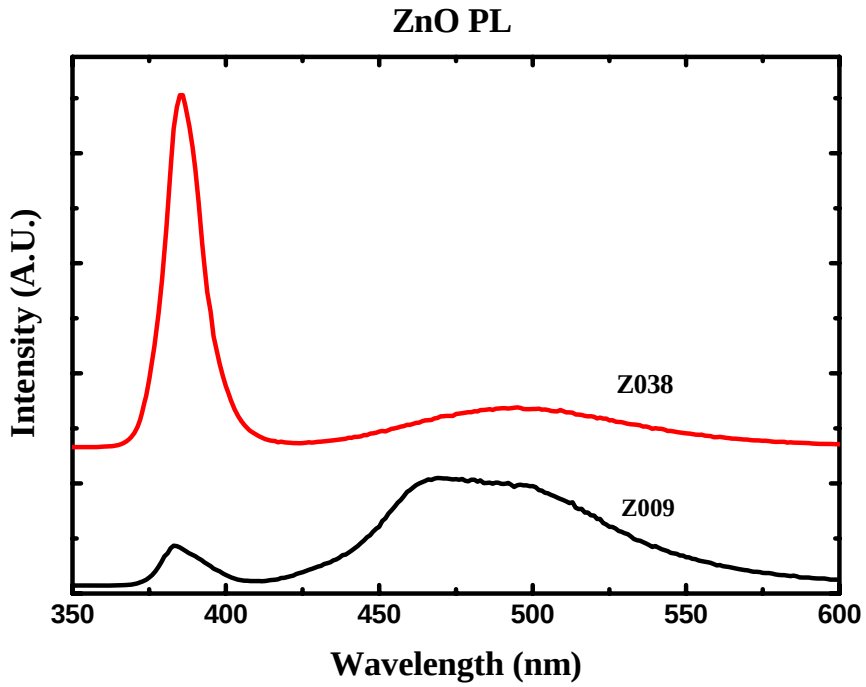

Figure 3.18 Room temperature PL spectrums of ZnO nanorods collected from two different samples synthesized by thermal CVD system.

It was often found that ZnO nanostructures with similar morphology and size possessed PL spectrum with quite different visible luminescence intensities, while similar PL spectrums may come from different nanostructures. Indicating that the morphology features as well as the size of the ZnO nanostructures are not the primary factors causing the visible luminescence; the ZnO PL is very sensitive to its surface conditions like the defect states, gas absorbents, and temperature etc. However, the PL spectra collected from different spots on the same sample were all similar to each other, indicating a good uniformity in terms of luminescence characteristics for samples prepared using this growth method.

It is well-known that temperature fluctuation causes the luminescence characteristic of ZnO nanostructure to change. The PL spectrums of two different ZnO nanostructures were collected at various temperatures are shown in Figure 3.19. One of the ZnO nanosrucutres' NBE emission peak underwent redshift as a result of the reduced band gap at elevated temperatures (Figure 3.19 (a)). [100] The NBE peaks were also broadened due to enhanced phonon scatterings (Figure 3.19). However, in Figure 3.19 (b), for the temperature dependent PL of the other ZnO nanostrucutres, the NBE peak underwent redshift but the NBE peaks did not have severe broadening. The intensity of the peaks remains consistent. As magnified in Figure 3.19 (c), the NBE peak of the ZnO tends to shift to longer wavelength at about ~10nm from 35°C to 200°C. The SEM images of PL spectrums in 3.19 (a) and (b) are shown in 3.19 (e) and (f). These visible luminescences may be caused by different deep level trapped defect states or different intermediate bands between the valence band and conduction band. While the ZnO sample's PL spectrum is taken under higher temperature (>>RT), the vibrations among the lattices will becomes much more severe as compared to room temperature lattice vibrations. Therefore, the severe lattice vibrations can provide a certain extra amount of momentum to cause the invisible transition to happen (as the case of the NBE intensity decrease in Figure 3.19(a)). However, the intensity of the NBE peak does not change in Figure 3.19(b), indicating that the transition that was caused by momentum does not take over as temperature increases, which may due to a larger required momentum. This is illustrated in the ϵ-k diagram of Figure 3.19(d). The momentum transition of Figure 3.19(d), Δp_1, can be used to explain the NBE transition of Figure 3.18(a). The lattice vibration due to

the elevating temperature can contribute extra momentum, more so than Δp_1. Therefore, the NBE decreases as the temperature increases. The momentum transition Δp_2 can be used to explain the NBE transition of Figure 3.19(b). Indicating that the momentum caused from elevating temperature is lower than Δp_2. Therefore, the NBE intensity keeps constant as temperature increases. The photon energy of the NBE as a function of temperature can be described by Varshini's empirical formula:

$$E_g(T) = E_o - \frac{\alpha T^2}{(T+\beta)} \qquad (5)$$

where E_o is the photon energy of the NBE emission at absolute zero. Equation (5) was used to fit the experimental data in Figure 3.20. The obtained α, β, and E_o are 1.5×10^{-3} eV/K, 244 K, and 3.38 eV, respectively. The obtained energy position at 0 K agrees well with the reported values for the energy position of the free exciton in ZnO. [101, 102] In Figure 3.19 (a), both the NBE and visible luminescence were quenched at increasing temperatures, but the intensity of visible luminescence decreased much faster. It was almost completely quenched at temperatures above 60^{o}C (Figure 3.21). For the blue-green emission band, no apparent shift can be observed while the temperature was increased, indicating that the defect levels involved in the blue-green luminescence were not associated with the band edges. [103] The electronic transitions of NBE emission take place among effective-mass like states and band edges. The thermal quenching behaviors of NBE and visible luminescence cannot be described by simple functional forms such as an exponential function. Nanostructures have small volumes and the lack of heat sink presents an entirely different condition compared to the thin film or bulk structures. The effective thermal conductivity of assembled ZnO nanostructures was greatly reduced

when compared to ZnO bulk strcutres. [104] The high power intensity of the focused laser beam and the strong absorption of UV laser light also elevate the local heating temperature of the illuminated nanostructure. Neutral density filters were progressively applied to reduce the power of the incident light until no more change was observed in the spectrum.

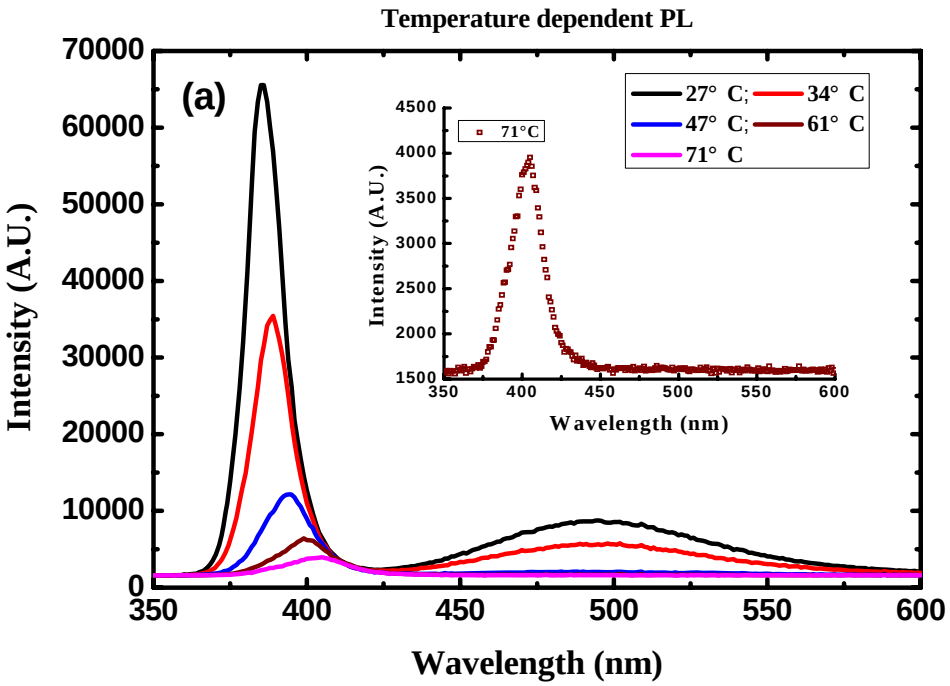

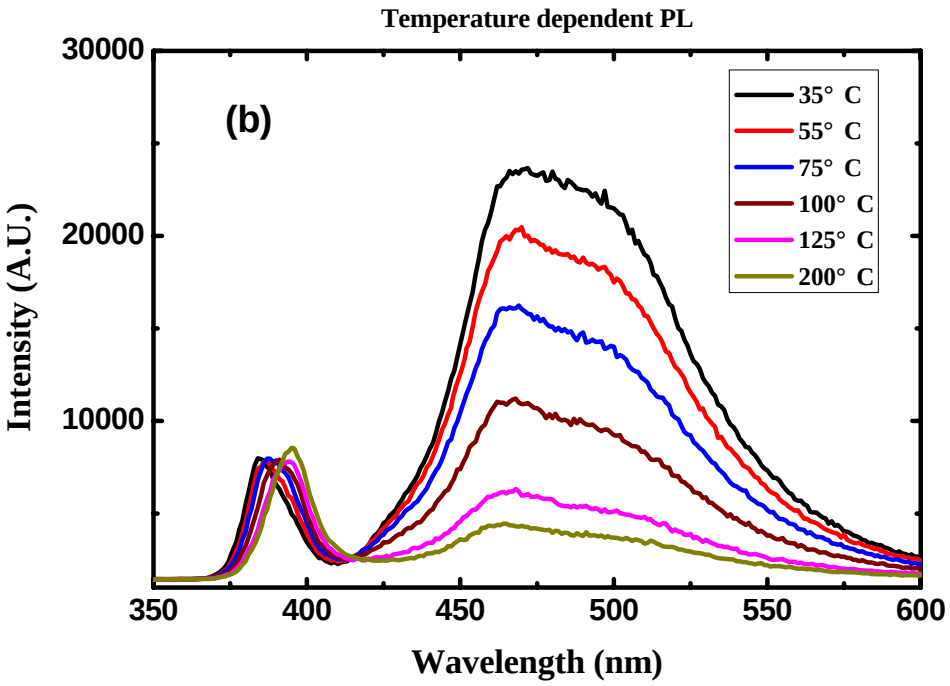
Temperature dependent PL
(b)
35° C
55° C
75° C
100° C
125° C
200° C
Intensity (A.U.)
Wavelength (nm)
30000
20000
10000
350
400
450
500
550
600

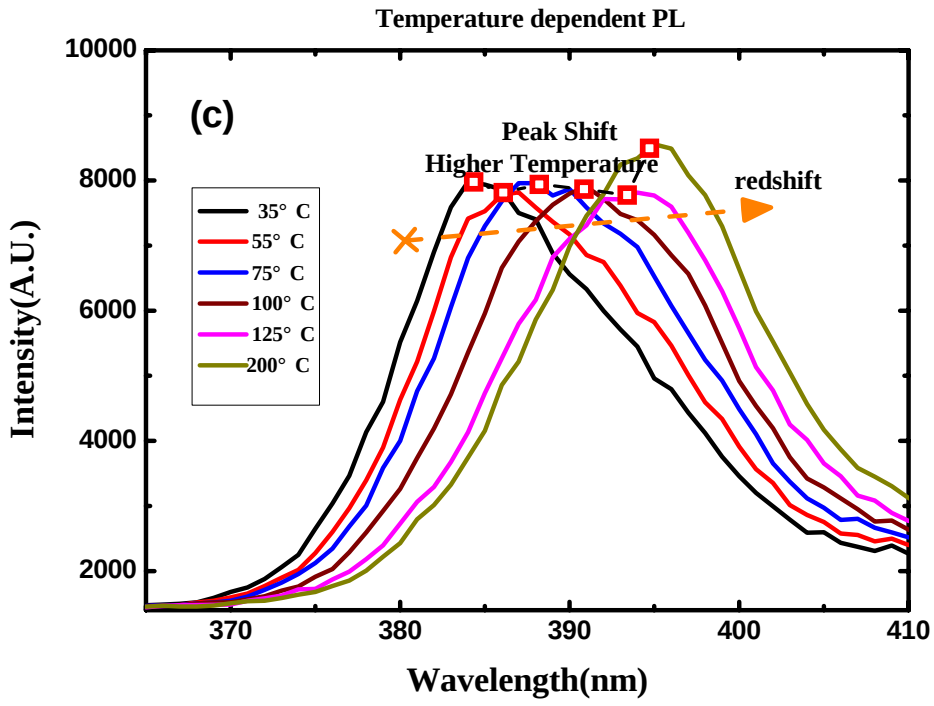
Temperature dependent PL
(c)
Peak Shift
Higher Temperature
redshift
35° C
55° C
75° C
100° C
125° C
200° C
Intensity(A.U.)
Wavelength(nm)
10000
8000
6000
4000
2000
370
380
390
400
410

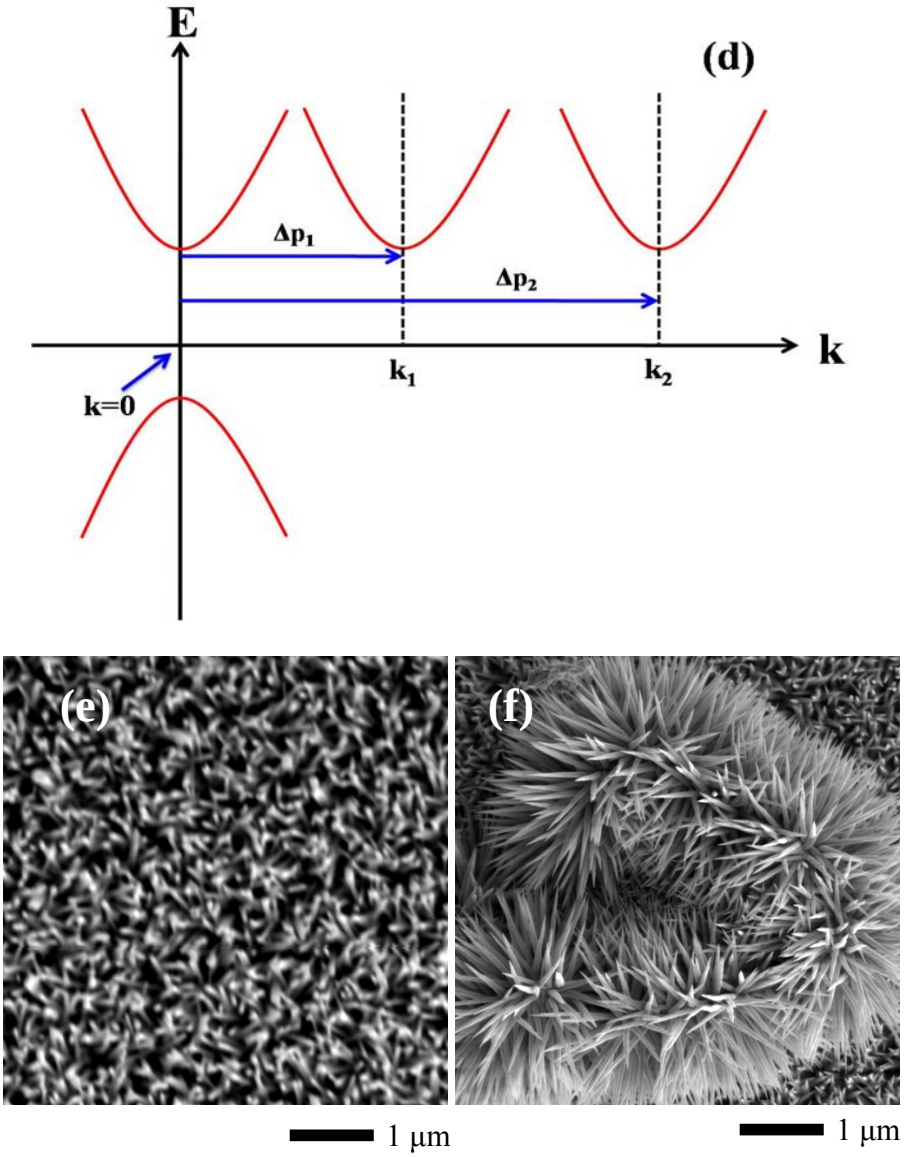

Figure 3.19 (a) PL spectrums of ZnO nanostructures collected at different temperatures from 27°C to 71 °C. Inset shows the PL spectrum collected at 71 °C at a higher magnification. [98] **(b)** PL spectrums of another ZnO nanostructures (Z009) collected at different temperatures from 35°C to 200 °C. **(c)** A higher magnification of the NBE mode peaks variation due to the elevating temperature of figure (b). **(d)** ϵ-k diagram to illustrate

the difference between the transitions cause by the momentum. **(e)** SEM image of the PL spectrum of Figure (a) **(f)** SEM image of the PL spectrum of Figure (b).

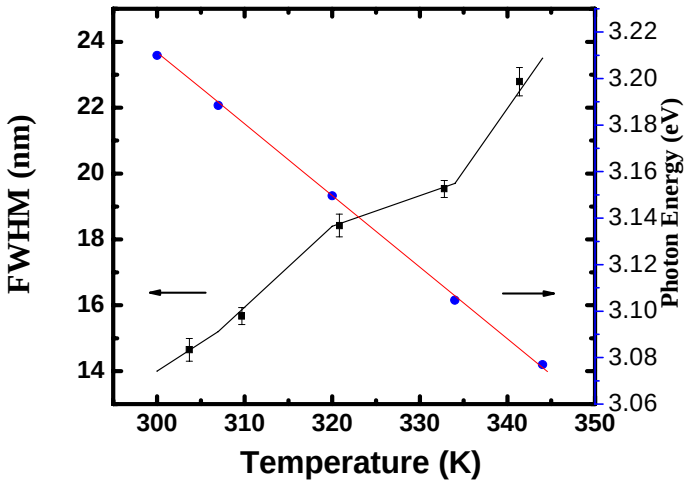

Figure 3.20 The FWHM and photon energy of NBE as a function of temperature. The red solid line is curve fitted by Varshini's function. [98]

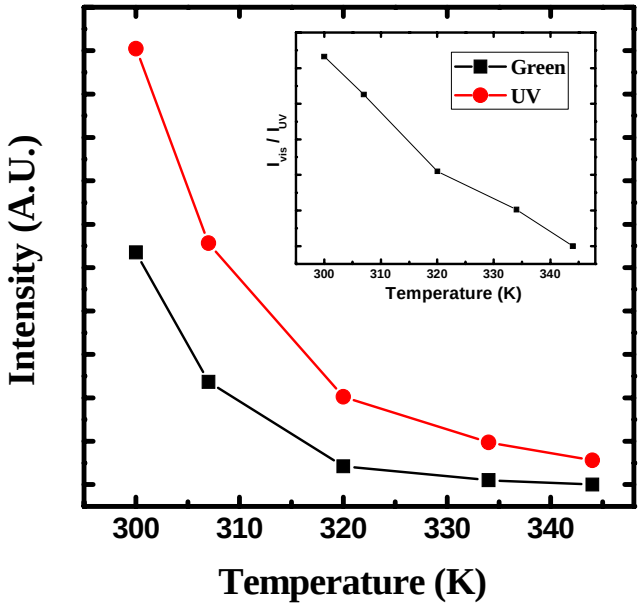

Figure 3.21 Intensity of NBE and visible emission as a function of temperature. The inset shows the ratio between the intensity of NBE and the intensity of visible emission at increasing temperatures. [98]

Figure 3.22 is the room temperature PL spectra of vertically well-aligned nanorods, inverse nanotetrapods, and nanoplants. All of these samples show a sharp ultra-violet NBE emission at 380 nm (3.26eV). The UV emission is generated by the recombination of free excitons through an exciton-exciton collision process. [105] The PL spectrum in Figure 3.22(a) shows a relatively high NBE peak and a small broad peak centered at 500nm. Studenikin *et al.* demonstrated that the green emission is typically related to oxygen deficiency, and the yellow/orange emission is associated with excess oxygen. [106] Vanheusden *et al.* reported that the green emission is due to the recombination of the electrons of singly occupied oxygen vacancies in ZnO, which is t the recombination of a photo-generated hole with an electron occupying the oxygen vacancies. [107] A further explanation of the visible luminescence of ZnO is arranged in the next section. Oxygen vacancies and Zinc interstitial related defects are the most possible factors causing green emission in our samples grown as the Ar to O_2 flow rate ratio higher than 10:1. The high NBE peak demonstrates that our vertically well-aligned ZnO nanorods possess highly crystalline qualitines. The inverse nanotetrapod shows a very similar PL spectrum with a lower NBE intensity compare to well-aligned ZnO nanorods. However, the PL spectrum of the nanoplant in Figure 3.22 (b) shows two shoulders, one centered at 460nm and the other centered 500nm. Cheng *et al.* claims that for tetrapodlike ZnO nanostructures the blue emission is originated from the oxygen vacancies due to the

significantly lower content of oxygen species during growth. [108] Even though the blue emission mechanism is still unclear, we believe that this emission is related to some kind of oxygen vacancy or related complexes.

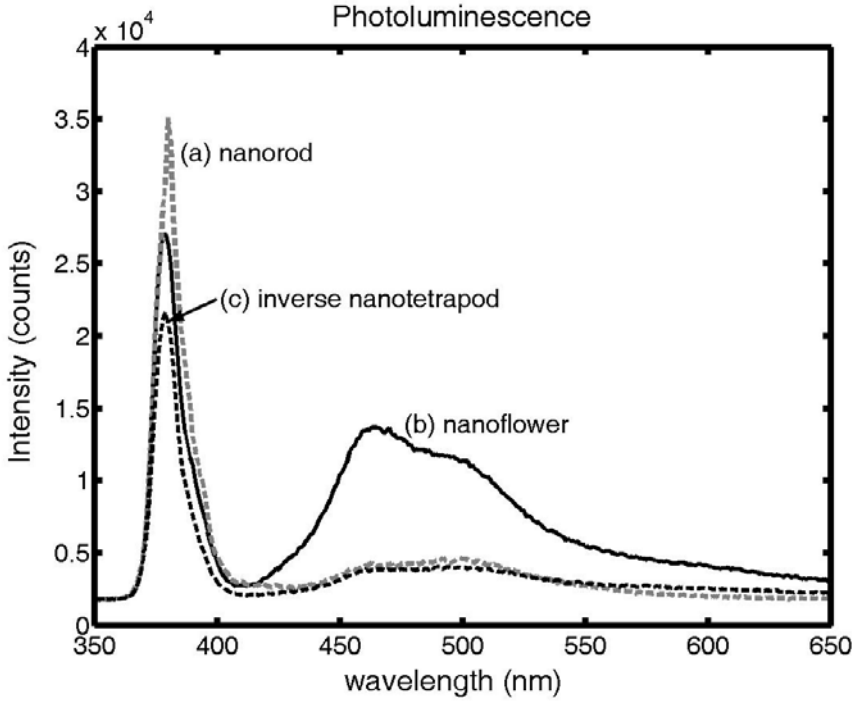

Figure3.22 PL spectra of the ZnO nanostructures (a) well-aligned nanorods (b) nanoflower (c) inverse nanotetrapod.

3.5 Visible luminescence from ZnO nanostructures

The room temperature PL spectrums of ZnO nanostructures synthesized by pressure controlled thermal CVD system are shown in Figure 3.23 (b) and (c). Spectrums b and c were collected from different locations on the same batch of sample. A typical PL spectrum, Figure 3.23 (a), of ZnO nanostructures synthesized *via* the oxygen-deficient thermal CVD system was also presented for comparison. All three spectrums showed the

ultra-violet near-band-edge (NBE) emission at about 3.21 eV. The visible emission from the sample deposited using oxygen-deficient CVD system was dominated by a broad blue-green emission band at about 2.48 eV. For samples deposited using the pressure controlled CVD system, the blue-green emission band at 2.48 eV was either greatly or completely reduced. Spectrum c in Figure 3.23 shows a dramatically different PL spectrum: the blue-green band has given away to very strong violet-blue emission bands as well as broad bands at yellow-orange-red range.

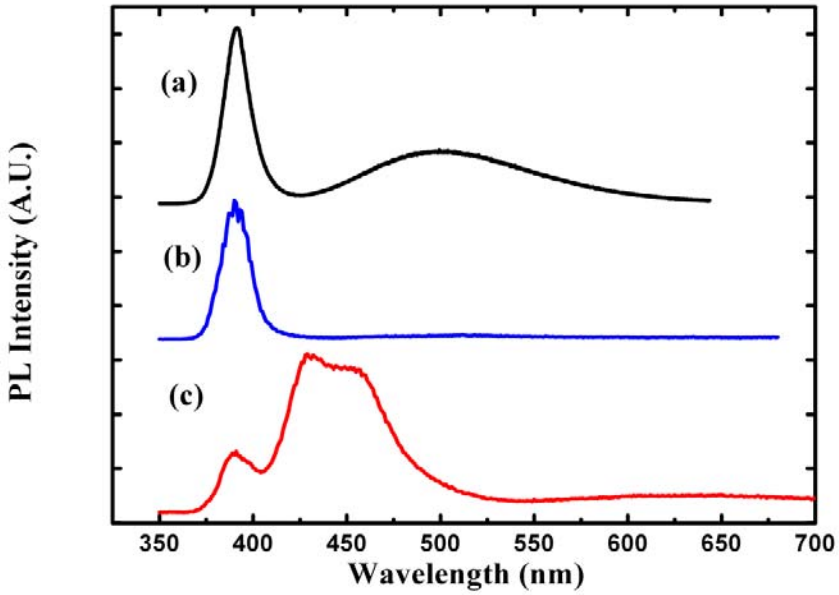

Figure 3.23 Room temperature PL spectrums of ZnO samples deposited using the oxygen-deficient CVD system (a), and the pressure-controlled CVD system [(b) and (c)]. Note that spectrums (b) and (c) were collected from different locations on the same sample.

Generally, the blue-green emission band was a result of oxygen deficiency during the growth process, while the yellow-orange emission bands were presented in samples grown with excess oxygen supply. [104,109,110] Therefore, it is expected that the blue-green emission band should dominate over other visible emission bands in the PL spectrum collected from samples synthesized by the oxygen-deficient CVD system (spectrum a in Figure 3.23). On the other hand, the PL spectrum of ZnO nanostructures synthesized in oxygen-controlled condition (spectrum b and c in Figure 3.23) should display suppressed blue-green emission and enhanced yellow-orange emissions. When the balance between zinc and oxygen was reached and the defects due to the non-stoichiometry minimized, the PL spectrum was essentially free of visible emission as shown in spectrum b of Figure 3.23. The PL spectrum of our ZnO samples are also in accord with the observation that the blue and the yellow-orange emission band always appear together, while the blue-green emission band doesn't coexist with the other emission bands. [111,112]

As demonstrated in the PL spectrums presented above, the PL characteristics of the ZnO samples deposited using the pressure-controlled CVD system were much less uniform as compared with those samples deposited using the oxygen-deficient CVD system. Quite different PL spectrums were often found at locations in close proximity (<0.5 mm apart), despite the fact that the morphology and size of the nanostructures are similar at these locations. We believe that the large variation in the PL characteristics is possibly related to the gas flow turbulence and vortex formed around the small quartz tube, which causes large ratio variation between the local oxygen and the zinc vapor

concentrations. Therefore, even though the morphology and the size are the same the visible region of the ZnO PL spectrum will be totally different.

It has been shown that the intensity of the blue-green emission was strongly influenced by the surface condition of the ZnO nanostructures. [113 ,114, 115] We have shown that through surface band bending the chemisorbed oxygen played a crucial role in the recombination process of the blue-green emission. [116] Equivalently important is the concentration and the spatial distribution of the defect states at which the recombination process of the blue-green emission takes place. It is believed that the recombination process happens between two defect-levels, and one of them involves the interstitial zinc or its complex. [117, 118, 119]

Since the oxygen-rich growth environment will lead to a more pronounced surface adsorption of oxygen, one should expect a strongest blue-green emission in the sample grown using the highest flow rate of oxygen, provided that the concentrations and distributions of the defect states of blue-green emission are similar among the three samples grown using different oxygen content. Therefore, the absence of the blue-green emission in the two samples grown with oxygen flow can be ascribed to the reduced concentration of defect states at which the blue-green emission takes place. The presence of other emission bands in the sample grown with high oxygen flow-rate can thus be explained as a result of the introduction of intrinsic defects such as interstitial oxygen and zinc vacancies.

In Figure 3.24 the PL spectrum of the sample deposited with a higher oxygen content was fitted with multiple Lorentzian peaks. Total seven emission bands were obtained:

ultra-violet (3.21 eV), violet (2.9 eV), blue (2.71 and 2.6 eV), green (2.19 eV), yellow (2 eV), red (1.8 eV). PL spectrum of the same sample collected using the 441.6 nm line of the He-Cd laser (Figure 3.24 b) only shows a red emission band. To the contrary, no emission bands were observed for the other two samples when the 441.6 nm line was used as excitation. The inability to generate the blue-green emission (~ 2.48 eV) by below-band-gap excitation [120], can be attributed to the nature of the recombination process which happens between a shallow donor level and a deep defect level. [121] Whereby, electron-hole pairs need to be generated by above-band-gap excitation first, so that later the photo-generated electrons and holes can be trapped by the shallow and deep level defect states respectively. The fact that the red emission can be generated by below-band-gap emission implies that it does not depend on the generation of conduction electrons and holes. The recombination process of red emission either happens between photo-generated holes bound at a deep-level state and free electrons in conduction band, or photo-generated electrons bound at a deep-level state and free holes in valence band. Since our ZnO samples are n-type material, the latter scenario is unlikely to happen. Another scenario is that the red emission process takes place in between the ground state and the excited state of a defect level, thus does not involve transitions of electrons in the conduction and valence band. It has been reported that the green (2.19 eV) and yellow (2 eV) emission bands can be generated by photons with an energy higher than 3eV [122], thus they were not observed in the PL spectrum (Figure 3.24 b) collected using 441.6 nm line as an excitation.

Our experimental results show that the ZnO sample characterized by blue-green PL emission is synthesized by an oxygen deficiency growth environment. With a slightly increased oxygen concentration presented during the growth, the blue-green emission can be greatly suppressed. The blue-green band has given away to relatively strong violet-blue emission bands and broad bands in the yellow-orange-red range. A red emission band was observed in PL collected using belowed-band gap excitation. The mechanisms of blue-green and red emission bands were analyzed using Lorentzian curve fitting and electronic transitions among defect levels.

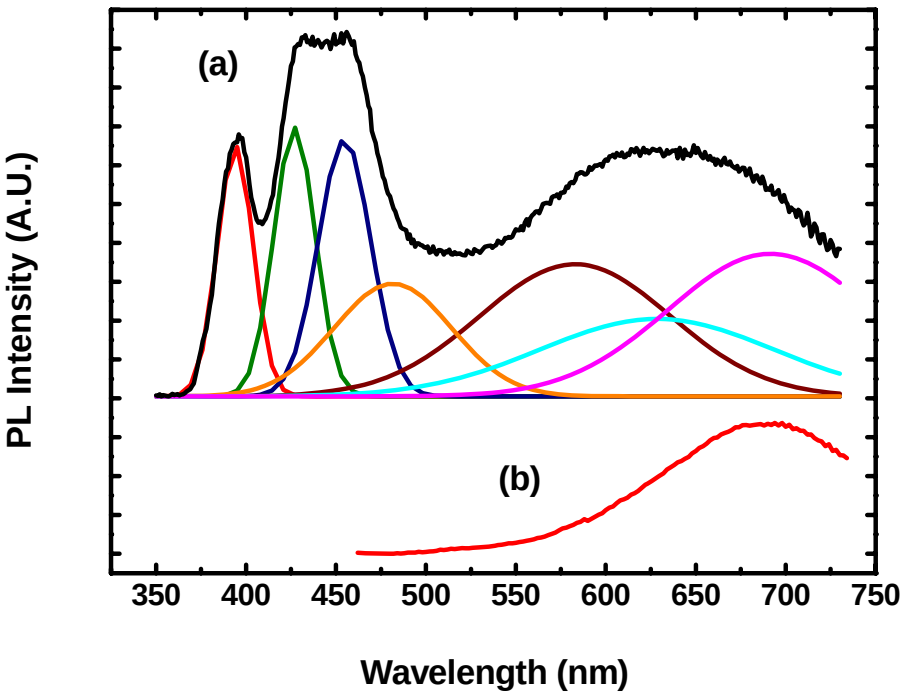

Figure 3.24 Room temperature PL spectrum of the sample deposited with high oxygen flow-rate collected using 325 nm line (a) and 441.6 nm line (b) of He-Cd laser. The thin

solid lines are emission bands obtained by curve-fitting multiple Lorentzian peaks to the PL spectrum.

3.6 Raman spectroscopy of ZnO Nanostructures

Room temperature Raman spectroscopy was performed using 441.6 nm line from a He-Cd (Kimmom) laser (80 mW). Raman spectra were collected using a spectrometer (JY-Triax550) equipped with two 3-inch holographic groove gratings (2400 lines/mm, 3600 lines/mm), and a thermoelectrically-cooled charge coupled device (CCD) detector (2048 × 512 pixels). The laser beams were focused onto a spot with ~5 μm in diameter on the sample surface using ×50 or ×100 lens (N.A.=0.45). The spectral resolution of the system is approximately 0.2 cm^{-1} as the 3600 groove grating is performed. For 2400 groove grating the spectral resolution is approximately 1cm^{-1}. Micro-Raman spectroscopy was carried out using a backscattering geometry z(-,-)z. The ×50 lens is used in order to carrier out a backscattering geometry spectroscopy setup. However, the ×100 lens can collect the Raman signal approximately 4 to 5 times higher than the ×50 due to the large collection angle but losing backscattering geometry design. The incident beam was linearly polarized and the polarization states of the scattered beam were not analyzed. An interference filter, acts as the band-pass filter, is located in front of the laser existence in order to purify the laser light matter. Typically, the entrance slit of the spectrometer was kept at 100μm wide in order to minimize the artificial broadening of the Raman scattering peaks induced by the finite slit size. [123]

ZnO crystal is one of the most important wurtzite crystals, exhibiting one of the simplest uniaxial structures. Wurtzite structure belongs to the space group C_{6v}^4 ($C6_3mc$) with two formula units per primitive cell and with all atoms occupying C_{3v} sites. [124] Group theory predicts the lattice phonons as [122]: an A_1 branch of which the Raman active phonon is polarized in the z direction and which is infrared active in the extraordinary ray; an E_1 branch in which the phonon polarized in the xy plane can be observed in the infrared in the ordinary ray spectrum and is also Raman active; two E_2 branches which are Raman active; and two silent B_1 modes. The Porto index is used to specify the scattering direction, such as x(-, -)y, the symbol inside indicates the polarization of the incident and of the scattered light matter, while the ones to the left and right of the parenthesis are the propagation directions of the incident and of the scattered light matter.

Our Raman setting is set to backscattering geometry of z(-,-)z, the x and y directions used in the measurements do not correspond to any specific crystal orientations. If only the c-plane ZnO is specified then the direction of x, y axis can be determined by using scattering geometry: z(u,z)v , where u and v are two directions in c- plane perpendicular to each other. If the u-axis is aligned with x-axis, we then have scattering geometry: z(x,z)y (as shown in Figure 3.25(a)) . If the v-axis is aligned with the y-axis we have z(y,z)x geometry, in either case only E1(TO) and no E1(LO) mode can be observed.

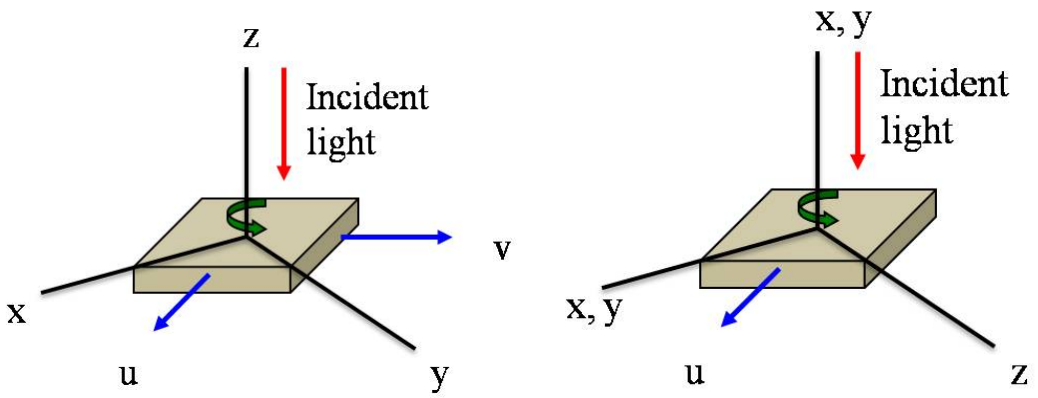

Figure 3.25 (a) scattering geometry of c face ZnO (b) scattering geometry of a face or m face ZnO.

If either the a-plane or the m-plane is specified then the direction of the z, y or z, x axis can be determined by using scattering geometry: x(u,u)x or y(u,u)y, where u is in the a-plane or m-plane. If the u-axis is aligned with the z-axis we then have a scattering geometry : x(z,z)x or y(z,z)y, in either case only the A_1(TO) mode can be observed. If the u-axis is aligned with the x-axis or y-axis we have a scattering geometry of x(y,y)x or y(x,x)y, in either case only the A_1(TO) and E_2 mode can be observed. In between those two extremes a E_1 mode will also appear.

The Raman spectrums (Figure 3.26(a)) of the undoped ZnO bulk crystals (Eagle Picher, Inc.) were collected for the purpose of comparison and reference. Three spectrums were collected: one from the c-plane and the other two from the a-plane of the crystal. Both spectrums in Figure 3.26 (a) & (c) were collected in the back-scattering geometry, thus the scattering geometry is Z(-,-)$\underline{Z}$ and X(-,-)$\underline{X}$ for c-plane and a-plane scattering respectively. According to the selection rule, the E_2 and A_1(LO) modes are the allowed modes in Z(-,-)$\underline{Z}$ scattering geometry, while the A_1(TO), E_1(TO) and E_2 modes are the

allowed modes in X(-,-)X scattering geometry. By rotating the a face ZnO 90°, the E_2 mode has been greatly suppressed and the E_1(TO) mode can be clearly observed. No mode mixing should be observed in both cases provided that the scattering geometries were strictly followed. The appearance of longitudinal acoustic (LA) overtone and quasi-LO mode is probably due to the miscut of the ZnO wafer. The frequencies and linewidth of the Raman modes were obtained by fitting the spectrums with Lorentzian functions, the results are shown in Table 3.2.

Table 3.2 Frequencies and FWHM of the Raman modes of a ZnO bulk crystal.

	A_1(TO)	E_1(TO)	E_2	LA overtone	A_1(LO)
Frequency (cm^{-1})	377.48	409.78	437.57	540.85	573.9
Linewidth (cm^{-1})	13.17	15.23	10.06	-	9.97

The room temperature Raman spectrum of the ZnO nanorods is shown in Figure 3.26(b). All Raman active modes were observed due to the random orientation of the nanorods. The overtone of the LO phonon mode is shown in Figure 3.26(c). The frequencies and FWHM of the Raman modes were obtained by fitting the spectrum with Lorentzian functions, the results are shown in Table 3.3.

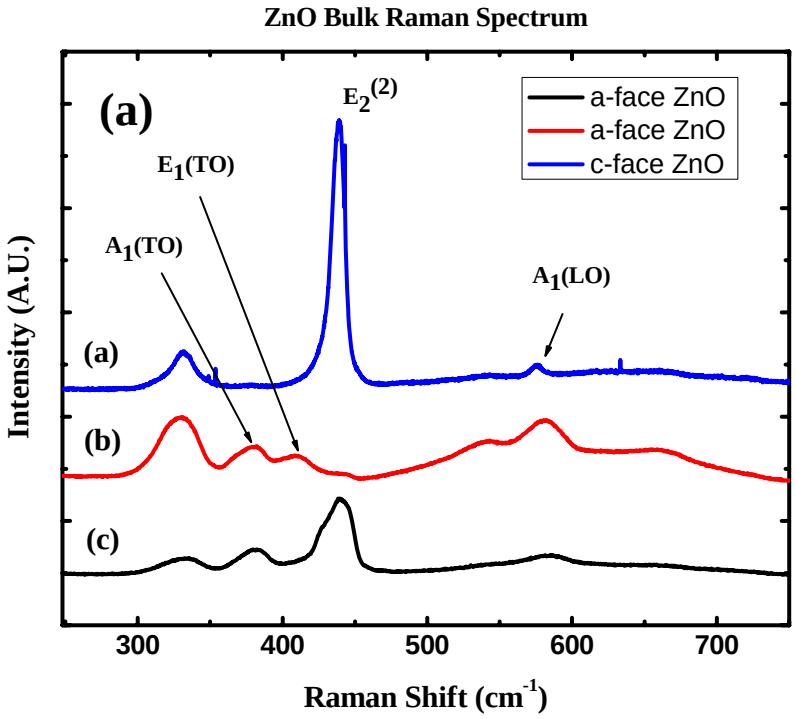
ZnO Bulk Raman Spectrum
(a)
$E_2^{(2)}$
a-face ZnO
a-face ZnO
c-face ZnO
E_1(TO)
A_1(TO)
A_1(LO)
(a)
(b)
(c)
Intensity (A.U.)
300
400
500
600
700
Raman Shift (cm^{-1})

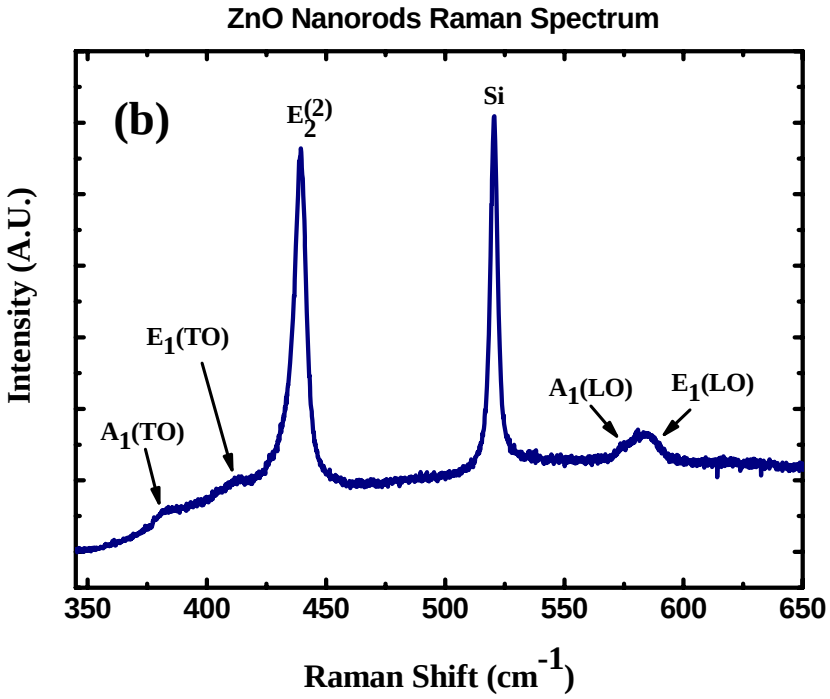
ZnO Nanorods Raman Spectrum
(b)
$E_2^{(2)}$
Si
E_1(TO)
A_1(TO)
A_1(LO)
E_1(LO)
Intensity (A.U.)
350
400
450
500
550
600
650
Raman Shift (cm^{-1})

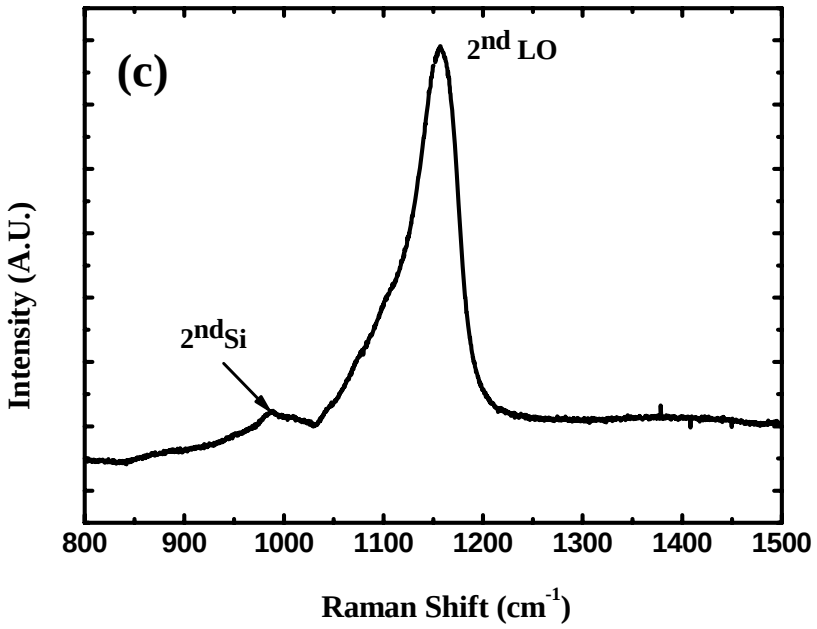

Figure 3.26 Room temperature Raman spectrum of (a) c-face and a-face ZnO bulk, (b) ZnO nanorods measured at low wavenumber region, and (c) ZnO nanorods measured at the high wavenumber region.

Table 3.3 Frequencies and FWHM of the Raman modes of ZnO nanorods.

	Quasi-(TO)	E_1(TO)	E_2	LA overtone	Quasi-(LO)
Frequency (cm^{-1})	380.5	409.3	436.4	1160	583.3
Linewidth (cm^{-1})	13.2	8.1	6.5	52	20.5

The FWHM of A_1(TO) (or precisely quasi-TO) and quasi-LO phonon mode are significant larger than the linewidth of the E_2 mode. The broadening in the A_1(TO) mode is largely caused by the mode mixing rather than the different phonon lifetime. The

broadening in LO phonon mode is caused by both the mode mixing and the plasmon-LO phonon coupling effect. It is well known that when the direction of phonon propagation is between the c-axis and the c-plane, a mixing of A_1 and E_1 modes will occur in wurtzite crystals where the long-range electrostatic force dominate over the anisotropic short-range force. [122, 125] As a result of mode mixing, the quasi-LO mode (QLO) obtained a frequency in between E_1(LO) and A_1(LO) modes, and the quasi-TO (QTO) mode adopts a frequency in between the E_1(TO) and A_1(TO) modes, while E_1(TO) remains unaffected. [118, 119, 126, 127]

$$\omega^2_{QLO} = \omega^2_{E1(LO)} \sin^2\theta + \omega^2_{A1(LO)} \cos^2\theta \qquad (7)$$

$$\omega^2_{QTO} = \omega^2_{E1(LO)} \cos^2\theta + \omega^2_{A1(LO)} \sin^2\theta \qquad (8)$$

where θ is the angle between the c-axis and the direction of phonon propagation. A larger angle θ will cause quasi-TO and quasi-LO modes to up-shift towards the E_1(TO) and E_1(LO) modes. Assuming that the nanorods are randomly orientated, the c-axis of the rod may take any angle between 0 and 90^{o}C, thus giving rise to mode mixing.

The frequencies of the E_1(TO) and E_2 mode of ZnO nanorods are very close to those of the bulk crystal. There is an approximately 1 cm^{-1} blueshift of the E_2 mode of the ZnO nanorods as compared to the bulk. The peak position of the E_2 mode is greatly affected by the biaxial stress in the c plane of the wurtzite crystal. Therefore, the biaxial stress, which is averaged stress over the entire length of the nanorod, was mostly released, assuming that the undoped bulk crystal is stress free. Given the frequencies of quasi-TO, A_1(TO) and E_1(TO) listed in Tables 3.1 and 3.2, equation 8 gives an effective angle θ of 15^o for the nanorods. Note that the effective angle only gives a rough estimation of the

overall orientation of the nanorods. The overall broadening in the ensemble spectrum depends on the homogenous broadening of the quasi-TO mode from an individual nanorod and the inhomogeneous broadening due to the different orientations in different nanorods. The analysis of the quasi-LO mode is further complicated by the effect of plasmon-LO phonon coupling. Unless the charge concentration of the nanorods is very low ($<3\times10^{16}$atoms/cm^3), the angle θ or the frequency of the quasi-LO mode cannot be estimated from equation 7. A detailed description of plasmon-LO phonon coupling is given in Chapter 4.

Temperature effects that causes the peak shift and symmetrically line broadening in the Raman spectrum cannot be ignored. Figure 3.27 (a) illustrates the line shape and peak shift changed *via* ramping up the temperature .However, the problem is less severe while using visible laser source in Raman experiments due to much weaker visible light absorption by ZnO. The same experiment protocol can be applied to reduce the thermal effect: the laser power can be progressively reduced until no change can be observed in the spectrum. Unfortunately, because of the inherently weak Raman signal, incident laser light has to be very intense in order to have sufficient signal to noise ratio. With the reduced laser excitation, usually only the E_2 mode was still detectable. In this way, the temperature induced peak shift in E2 mode can be readily obtained. The ZnO bulk E_2 mode peak shift due to the elevating temperature is shown figure 3.27 (b). A more detailed technical description for the correction of temperature effect in all Raman modes is described in Chapter 4.

In polar semiconductor, collective excitation of free carriers (plasmon) can interact with longitudinal-optic (LO) phonons *via* longitudinal electric field, and form LO-phonon-plasmon coupled (LPP) modes. In other words, the ling-range electrostatic coupling of LO phonos with the charge density wave of an injected plasma (plasmon) results in the formation of two hybrid excitations with deeply modified static and dynamic properties as compared to their parent modes. A detail study of the LO phonon modes is described in Chapter 4. Raman scattering of the LPP modes has been intensively studied in III-V, II-IV and IV-IV compound semiconductor. [128] The LO phonon mode scattering is due to the electric field induced effect, the LO phonon to E_2 phonon scattering intensity ratio was determined by the strength of the electric field in the depletion layers and by the surface to volume ratio of the nanostructures. [98] Even though Raman scattering took place in the entire volume of the nanostructures, only a fraction of the total scattering volume was affected by the electric field. In some cases, the relative intensity of the E_2 mode and the LO mode varied significantly for the same sample at different spots. However, the morphology and size of the nanostructures at two separate locations were similar; and the ratio of the field affected scattering volume to the total scattering volume was also similar. In addition, since the two locations were in close proximity on the same sample, and both had undergone identical process/storage conditions, the extent of oxygen adsorption at the surface of the nanostructures should be similar as well. Because the band bending is determined by the extent of the oxygen adsorption, it is reasonable to assume that there was no big difference in the electric field

among the nanostructures on the same sample. In view of these facts, the extent of the electric field effect should also be similar for the nanostructures at two locations.

It can be concluded that while a large difference in the intensity of LO phonon scattering was detected; it is most likely caused by the difference in the concentration of the energy levels formed in the band gap. These energy levels, in all probability, were formed by native defects created in the crystal during growth. They may play roles in the visible luminescence processes as well. Although the same defect states may participate in both Raman scattering and visible luminescence processes, no simple correlations between the characteristics of Raman and PL spectrums could be found. Nevertheless, it was always found that if Raman spectrums display a large variation at different locations on a certain sample, the PL spectrum will also display a large variation at those locations. [98] In other words, any statement regarding the uniformity of the optical properties of a certain sample is applicable to both Raman and PL spectrums.

Figure 3.28 is the Raman spectra for different kinds of 2D ZnO nanostrucutres arrays such as inverse nanotetrapods, nanoplants, nanorods, nanonails, and nanotips. All ZnO nanostructures show a clear E_2 mode peak at 435cm^{-1} and a A_1(LO) peak at 574cm^{-1} demonstrating the typical wurtzite structure with high crystallinity. Curve (a) in figure 10 shows the Raman spectrum for ZnO inverse nanotetrapods. The more pronounced background may be largely due to the enhanced diffusive scattering by the tetrapod structure causing a stronger stray light in the optical system. The A_1(TO) peak for this sample has been covered by the background signal. The rest of the ZnO nanostrucutres

have a shoulder at 380 cm^{-1} which corresponds to the A_1(TO) peak. The extra shoulder located at 321 cm^{-1} is contributed by the ITO thin film.

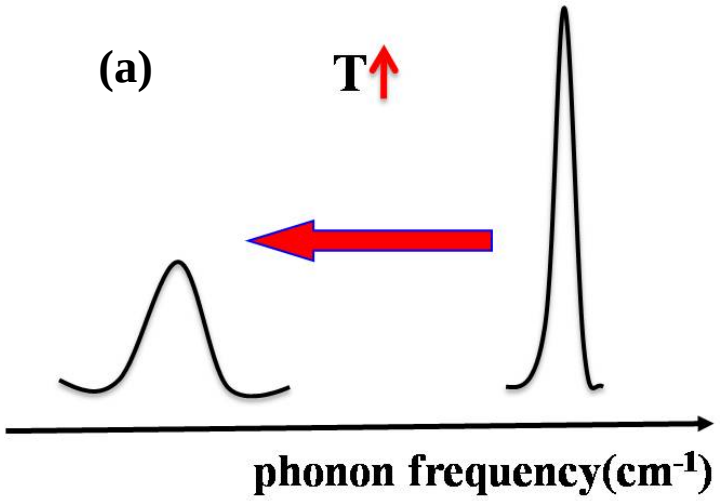

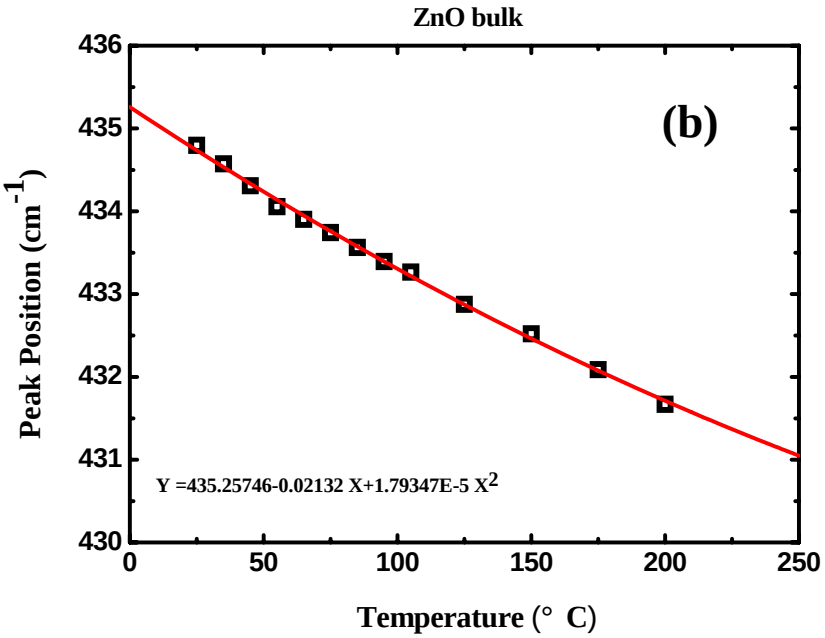

Figure 3.27 (a) Illustration of the line broadening and peak shift of the Raman spectrum due to the elevating temperature, (b) The ZnO bulk E_2 mode peak shift due to the elevating temperature.

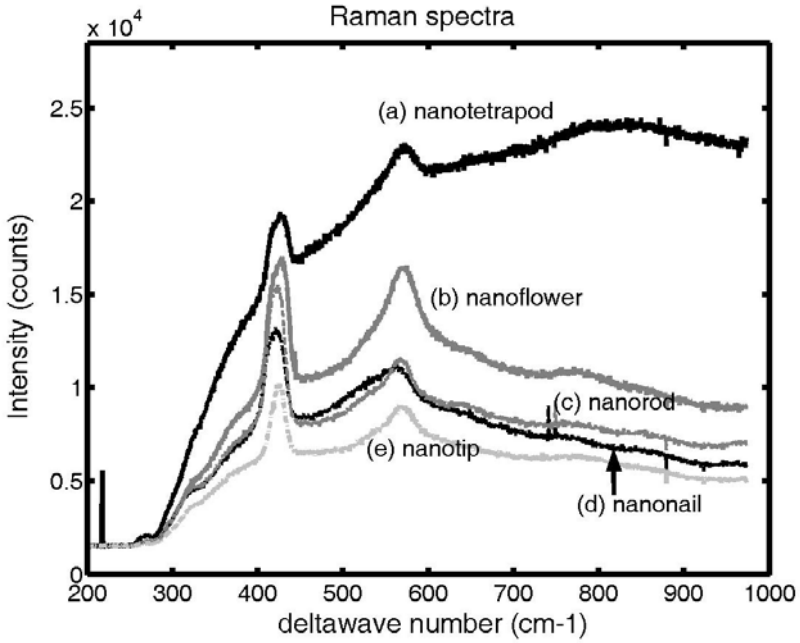

Figure3.28 Raman spectra of the ZnO nanostructures (a) inverse nanotetrapod (b)nanoflower (c) nanorods (d) nanonail (e) nanotip.

3.8 Conclusion

In summary, we have demonstrated an advanced growth setup method based on traditional thermal CVD growth. This DSDT setup method can greatly improve the reproducibility and controllability of different well-aligned morphologies of ZnO nanostructures growth on different substrates like ITO and Si. Typically, ZnO nanostrucutres grown by thermal CVD method can achieve relatively high crystallinity, but it is difficult to control the ZnO morphologies. We have successfully synthesized

several morphologies, such as nanorods, nanotips, nanoflowers, nanonails, and inverse nanotetrapod, with high crystallinity, high controllability, and highly reproducibility. We have also showed that the tip size of the ZnO nanorods would decrease from 100nm to ~30nm as the growth pressure decreased by using non-catalyst growth method. We also found that it is harder to control the growth morphology at low growth pressure, but applying some metal catalysts can enhance the growth and generate different growth morphologies. ZnO nanostructures are allowed to be grown under lower pressure (e.g. 15Torr) with different morphologies like nanoplants, nanonails and nanoflowders by applying certain liquid metal catalysts. The visible luminescence of the nanostructures synthesized in oxygen-deficient environment has a dominant blue-green band. The ZnO nanostructures were found to be mostly stress-free by the Raman experiment. Various broadening and enhancement effects in different Raman modes were discussed. No general correlations could be found between the morphologies and the luminescence/Raman characteristics of the nanostructures. Room temperature PL shows a strong and dominant UV emission at 380 nm that reveals good optical properties for these as-grown ZnO nanostructures. It is important to achieve the synthesis of ZnO nanostructures onto TCO substrates in light of future optoelectronic device applications such as solar cells, LEDs and photodetector sand so on.

CHAPTER 4

RAMAN SCATTERING OF LO PHONON-PLASMON-COUPLED MODES IN BULK ZINC OXIDE AND ALIGNED ZINC OXIDE NANORODS

4.1 Introduction

Recently, one dimensional (1D) semiconductor nanorods have been considered as promising building blocks for nanoscale photonics devices and circuits. [129,130,131] Among these semiconductor nanorods, 1D zinc oxide (ZnO) is one of the most intensively studied nanorod materials. ZnO is a wide band-gap semiconductor which possesses a direct band gap of 3.37eV and room temperature exciton binding energy of 60meV. ZnO has been considered the promising candidate for sub-wavelength waveguide, ultraviolet (UV) laser diodes, UV photodetectors, white light emitting diode, solar cell, and other types of optoelectronics devices. Room temperature stimulated excitonic emission and optically pumped laser action are observed from high quality ZnO thin film, the optical gain of the stimulated emission is primary due to an excitonic-excitonic collision process; therefore, ZnO is suggested to be suitable candidate for UV laser applications. [132, 133] Exciton-based ZnO laser is expected to have better performance over GaN-related materials. [134] 1D ZnO nanostructure attracts numerous research surges due to its good crystal qualities and photonic properties. It is significantly

important to characterize the electronic properties of the 1D ZnO nanorods in order to precisely fabricate the nanorod-based electronic and optoelectronic device with a desired performance. Electrical characterization techniques such as Hall [135] and impedance [136] measurements are contact methods to measure carrier concentration, and mobility. On the other hand, optical measurement such as Raman spectroscopy provides a non-contact method to measure the electronic parameters. Optical method is more useful than electrical counterpart when analyzing low-dimensional materials system due to difficulty in preparation of the contact to nanostructure.

Raman characteristic of LO-phonon-plasmon coupled (LPP) modes is used to demonstrate the combined of phonon confinement and crystal orientation, both of which become significantly importance with decreasing dimensionality. LPP modes have been intensively investigated in wide band-gap polar semiconductors using Raman spectroscopy. [137,138] In polar semiconductors, the long-range electrostatic Coulomb force interacts with LO phonons and the fluctuated charge-density wave of an injected plasmon resulted in the formation of two hybrid excitations of the LO-phonon-plasmon coupled modes. The LO-phonon-plasmon coupled modes mediate the carrier-lattice energy exchanges and play a central role in carrier relaxation and transport. [139, 140, 141, 142, 143, 144] If the plasma energy lies in the order of magnitude as the LO phonon energy, the resulting phonon-plasmon modes show a distinct energy shift as compared with the uncoupled excitations while the TO phonons remain unchanged. Gallium arsenide (GaAs) was the first semiconducting material from which the LPP mode has been observed by Raman spectroscopy. [135] The relative energy shift and line-width

broadening of the phonon modes are directly influenced by the concentration and the mobility of free charge carriers, respectively. Both LPP modes can be observed if the damping of plasmon is sufficiently small. However, only the high frequency LPP^+ mode can be observed while large plasmon damping is detected. Previously, LO phonon-plasmon coupled modes in aligned GaN nanorods were observed using Raman spectroscopy. [145] However, LO phonon-plasmon coupled modes of ZnO nanorods have not been investigated. Therefore, in this work, we have studied LPP modes in ZnO nanorods systematically. As a comparison, the LPP modes collected from single crystal bulk ZnO wafer was also investigated.

Electronic properties of undoped bulk zinc oxide (ZnO) and vertically well-aligned ZnO nanorods have been investigated using micro-Raman spectroscopy. The carrier concentration as well as the mobility have been characterized using A_1(LO) phonon-plasmon coupled mode line shape analysis. The local laser temperature heating and the stress effects were considered before analyzing the A_1(LO) coupled mode. The mobility and carrier concentration of the undoped bulk ZnO obtained from the line shape analysis were 108.87cm^2/V-s and $1.94\times10^{17}/cm^3$, respectively. The carrier concentration of the undoped ZnO obtained from the C-V measurement further confirmed the results obtaining form A_1(LO) mode line shape analysis. The mobility and carrier concentration of well-aligned ZnO nanorods were 84.76cm^2/V-s and $3.76\times10^{17}/cm^3$, respectively. The mobility of well-aligned ZnO nanorods is about 20% lower than that of undoped bulk ZnO can be regarded as the enhanced surface scattering.

4.2 Experiment

Vertically aligned ZnO nanorods were grown on p-Si substrate using thermal chemical vapor deposition (CVD). An ultra thin layer (with thickness of ~20nm) of zinc was sputtered on the p-type Si substrate before synthesizing the ZnO nanorods. The as-sputtered samples were loaded into a furnace box at the temperature of 400°C for 8 hours at one atmosphere in order to further generate nucleation sites. All the samples were ultrasonically cleaned in pure methanol for 10 minutes, followed by immersing the samples in methanol with a suspension of zinc nanopowder for additional 30 minutes. No special metal catalysis was used in nanorod growth for minimizing the contamination. All the as-prepared samples were loaded on top of an alumina boat containing a small amount of Zn powder. Meanwhile, additional alumina boat containing very little amount of Zn powder was inserted into the end of a smaller quartz tube before loading alumina boat with the samples on it. Then, the temperature of the CVD reactor was elevated to 500°C at a ramping rate of 5 °C/ min. Argon (Ar) and oxygen (O_2) were used as the carrier and reactant gases for ZnO nanorods growth, respectively. The flow rate of Ar and O_2 were 88sccm and 8sccm, respectively. The growth of ZnO nanorods was performed at 50 Torr for 60 minutes.

The surface morphologies of the samples were studied using a field-emission scanning electron microscope (FE-SEM, JOEL JSM-7000). The crystal structures of the samples were characterized by X-ray diffraction (XRD) using a Rigaku Miniflez powder x-ray diffrectometer with Cu Kα radiation. Photoluminescence (PL) and micro-Raman spectroscopy were performed at room temperature using 325 nm and 441.6nm laser line

from a He-Cd laser (Kimmon Electric) with a JY spectrometer integrated with a diffraction grating with 3600 line groove density. In the case of Raman scattering measurement, backscattering geometry was used. The spectral resolution of the grating is 0.2 cm^{-1}. The laser beam was focused onto a spot of approximately 5 μm in diameter on the sample surface. Both the spectra were collected using a spectrometer with a thermally-cooled charge coupled device (CCD) detector.

4.3 Results and Discussion

The SEM images of the vertically aligned ZnO nanorods synthesized using thermal CVD is shown in Figure 4.1. The low magnification SEM showed in Figure 4.1(a) reveals that the well-aligned ZnO nanorods were uniformly grown on a relatively large area of the Si substrate. Figure 4.1(b) shows the high resolution SEM image of the ZnO naorods. The hexagonally-shaped crystal with an average nanorod size of 100-150nm can be clearly observed. The XRD pattern shown in Figure 4.2 also reveals high crystallinity and c-axis preferential growth of these ZnO nanorods. Only the X-ray diffracted peaks corresponding to the (0002) and (0004) planes can be seen.

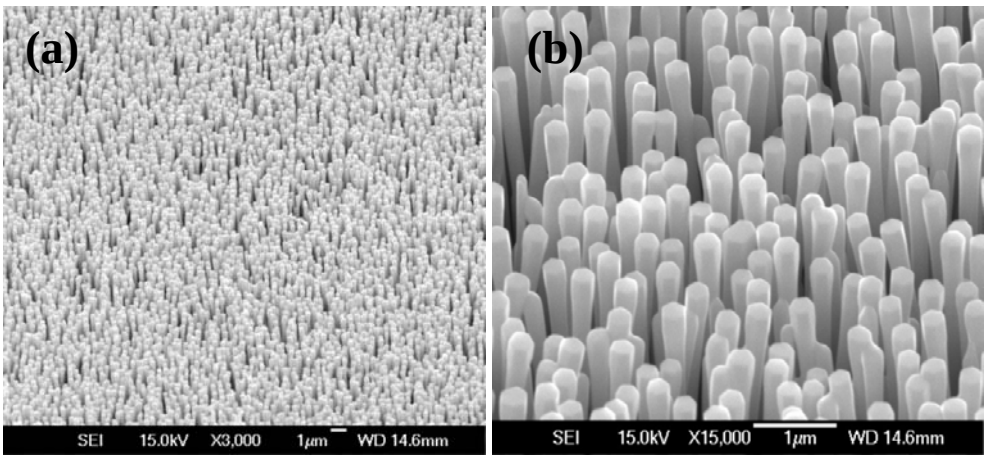

Figure 4.1 (a) Low magnification SEM of aligned ZnO nanorods; (b) high magnification of ZnO nanorods.

Thermodynamically stable ZnO crystallite possesses a wurtzite structure and belongs to the space group of C_{6v}^4. Group theory predicts that the material with C_{6v}^4 space group is expected to have $A_1(z)+2B_1+E_1(x,y)+2E_2$ optical phonon modes at the Γ point of the Brillouin zone. [146] Among these optical phonon modes, the A_1 mode is both infrared and Raman active, and is polarized in the z-direction. The E_1 mode is also infrared and Raman active but the phonon is polarized in xy plane. The two B_1 modes are silent and the two E_2 modes are Raman active. A_1 and E_1 are two polar modes which can be influenced by the long-range macroscopic electric field. Therefore, these two polar phonon modes would split into longitudinal optical and transverse optical branches. The local long-range macroscopic electric field serves to stiffen the force constant of the phonon, and raise the frequency of LO over that of the TO. [140] The consequence of this process on the static dielectric constant of the crystal is determined by the well-known Lyddane-Sachs-Teller relationship [147]:

$$\varepsilon_0 = \varepsilon_\infty \left(\frac{\omega_{LO}}{\omega_{TO}}\right)^2$$

Raman modes that can be observed in a spectrum are strongly dependent on the Raman selection rules which take into consideration of the orientation of the crystal with respect to the directions of propagation and polarization of the incident and Raman scattered light. The matrix formation of each phonon modes is expressed below:

$$A_1(z)=\begin{pmatrix} a & 0 & 0 \\ 0 & a & 0 \\ 0 & 0 & b \end{pmatrix},\quad E_1(x)=\begin{pmatrix} 0 & 0 & c \\ 0 & 0 & 0 \\ c & 0 & 0 \end{pmatrix}$$

$$E_1(y)=\begin{pmatrix} 0 & 0 & 0 \\ 0 & 0 & c \\ 0 & c & 0 \end{pmatrix},\quad E_2=\begin{pmatrix} d & d & 0 \\ d & -d & 0 \\ 0 & 0 & 0 \end{pmatrix}$$

Since the z(x,-)z backscattering geometry was employed and the c-axis of ZnO is along the z-direction, only the Raman peaks of A_1(LO), $E_2^{(1)}$, and $E_2^{(2)}$ modes can be observed according to the Raman selection rule. According to the selection rule, ZnO nanorods must be grown along the c-axis for pure A_1(LO) mode collection. If the nanorods are tilted in a certain angle, quasi-modes arised from mode mixing can be collected. The phonon frequency of the quasi-LO mode lies in between those of E_1(LO) and A_1(LO) modes. The frequency of quasi-LO mode (ω_{QLO}) can be described using the following equation;

$$\omega_{QLO}^2 = \omega_{E1(LO)}^2 \sin^2\theta + \omega_{A1(LO)}^2 \cos^2\theta\,, \qquad (1)$$

where θ is the angle between the c-axis and the direction of phonon propagation. Therefore, in order to collect pure LO Raman peak, the nanorods with c-axis orientation should be used for Raman measurement.

Two phenomena need to be considered first before fitting the Raman spectrum; one is the Raman peak shift due to the stress and the other is the peak shift due to the laser heating of the nanorods. The peak position and the full-width-at-half-maximum (FWHM) of Raman $E_2^{(2)}$mode of updoped ZnO bulk and aligned nanorods were determined by fitting the mode using Lorentzian function. The Raman spectra of the undoped bulk ZnO

crystal was also collected for comparison. As shown in Figure 4.3, the peak position and full-width-to-half-maximum (FWHM) of the undoped ZnO bulk are 435.32cm^{-1} and 12.50, respectively.

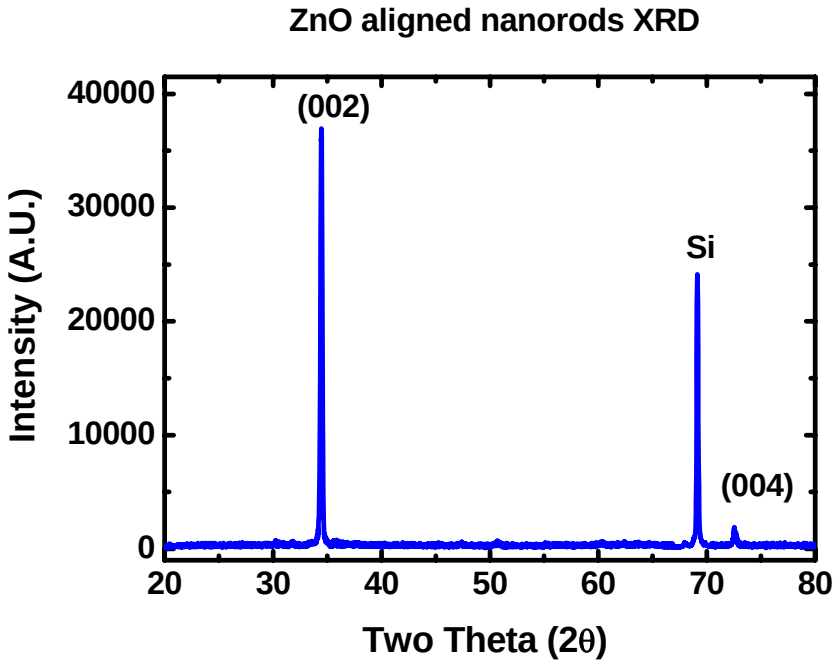

Figure 4.2 XRD pattern of high crystallinity vertically well-aligned ZnO nanorods preferential growth along c-axis direction.

The peak position and FWHM of the aligned ZnO nanorods are 435.18cm^{-1} and 12.27, respectively. Since $E_2^{(2)}$ mode is sensitive only to stress, this peak was used to study if the samples are under stress. Compressive and tensile stress of the sample will shift this peak to a higher and a lower wavenumber, respectively. Assuming that the ZnO bulk crystal is stress free and neglecting the hydrostatic stress contribution from the point defects, the $E_2^{(2)}$ peak position difference between the ZnO bulk and the aligned ZnO nanorods is downshift 0.14 cm^{-1}. However, the spectral resolution of the monochromator we have used is 0.2 cm^{-1}. Therefore, the difference in frequency of the $E_2^{(2)}$ mode for

bulk ZnO and the aligned ZnO nanorods can be reasonably neglected, and the ZnO nanorods can be considered as stress free.

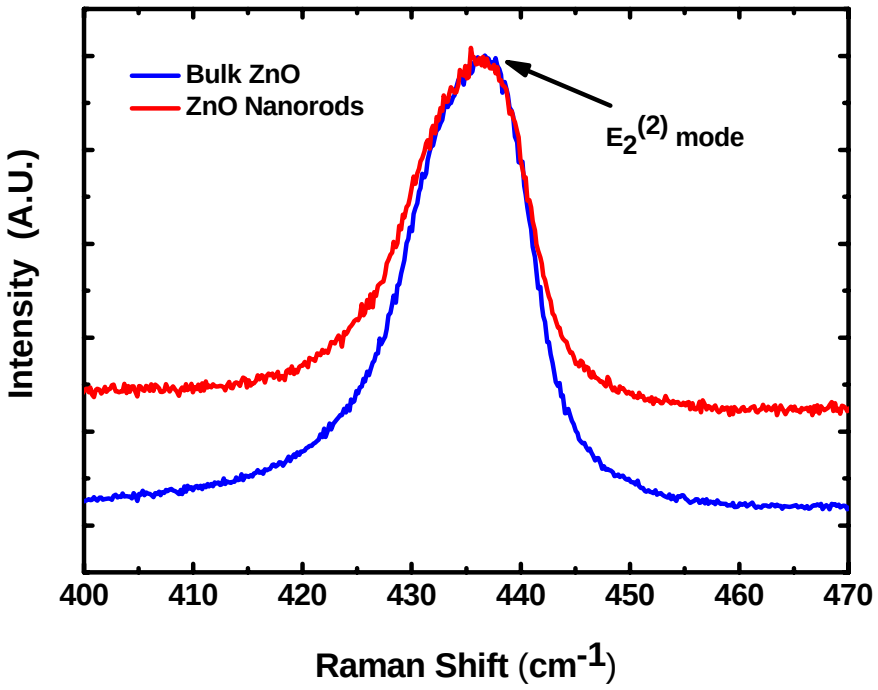

Figure 4.3 The $E_2^{(2)}$ mode peak position and FWHM of undoped bulk ZnO and well-aligned ZnO nanorods.

Upon illumination of the sample by a focused laser beam, the local temperature of the sample can be elevated up to several hundred degrees Celsius, which cause the downshift and broadening of the Raman peaks. The laser heating effect can be even more severe in micro- and nano-structured materials due to their reduced thermal conductivity [148] and a large surface-to-volume ratio. Both the Stokes and anti-Stokes part of Raman spectra were collected for the undoped bulk ZnO and aligned ZnO nanorods in order to estimate or eliminate the Raman peak shift due to the local laser heating. The ratio of the

integrated intensity of the Stokes (I_s) E_2 mode to that of the anti-Stokes (I_{AS}) E_2 mode were determined, and the intensity ratio is a function of temperature as follows [149,150] :

$$R = \frac{I_S}{I_{AS}} = \gamma\left(\frac{\omega_l - \omega_p}{\omega_l + \omega_p}\right)^4 \frac{\alpha_l + \alpha_s}{\alpha_l + \alpha_{AS}} \exp\left(\frac{\hbar\omega_p}{k_B T}\right), \qquad (2)$$

where α_l, α_{AS}, and α_S are the absorption coefficient for laser, anti-Stokes, and Stokes spectra, respectively. ω_l , and ω_p are frequencies of the laser and the E_2 phonon mode, respectively. The 4th power term is considered the different scattering cross section for Stokes and anti-Stokes light, while γ is the factor that demonstrates the detection efficiency of the optical system. [148] If the difference in temperature (ΔT) of the two samples is concerned, then equation (2) can be further simplified by eliminating all the other parameters except for the exponential term:

$$\frac{R_1}{R_2} = \exp\left[\frac{\hbar\omega_p(T_2 - T_1)}{k_B T_1 T_2}\right] \approx \exp\left(\frac{\hbar\omega_p \Delta T}{k_B T^2}\right), \qquad (3)$$

where R_1 and R_2 is the Stokes to anti-Stokes ratio of undoped bulk ZnO and aligned ZnO nanorods, respectively. Figures 4.4(a) and (b) show the collected Stokes and anti-Stokes Raman spectrum for undoped ZnO bulk wafer and aligned ZnO nanorods for estimating the corresponding peak shift due to the local laser heating. Assuming that the laser heating of the undoped bulk ZnO crystal is neglected (letting T=300K in equation 3) the temperature difference between the bulk ZnO and the aligned ZnO was found to be 2°C. The approximation used in the equation can be justified since the temperature difference (ΔT) is significantly smaller than the square the temperature (T^2) in the denominator. Temperature-dependent Raman peak shift of wurtzite ZnO bulk and nanorods was

studied and the Raman peak shift due to the estimated temperature difference was calculated to be less than 0.2cm^{-1}. Therefore, the Raman peak shift due to the local laser heating can be neglected. However, the profiles of the peak shift correspond to the heating temperature of bulk, nanorod and nanopowder ZnO were performed and showed in Fig 4.5.

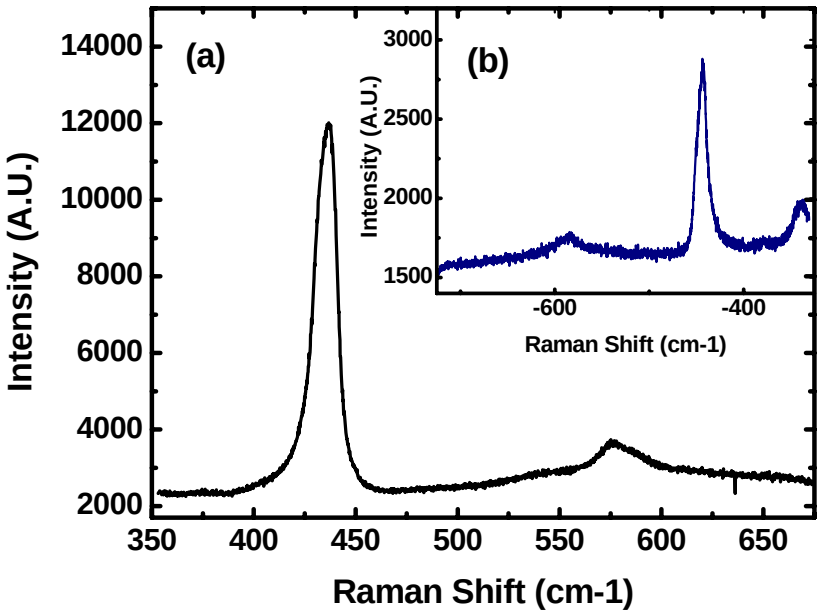

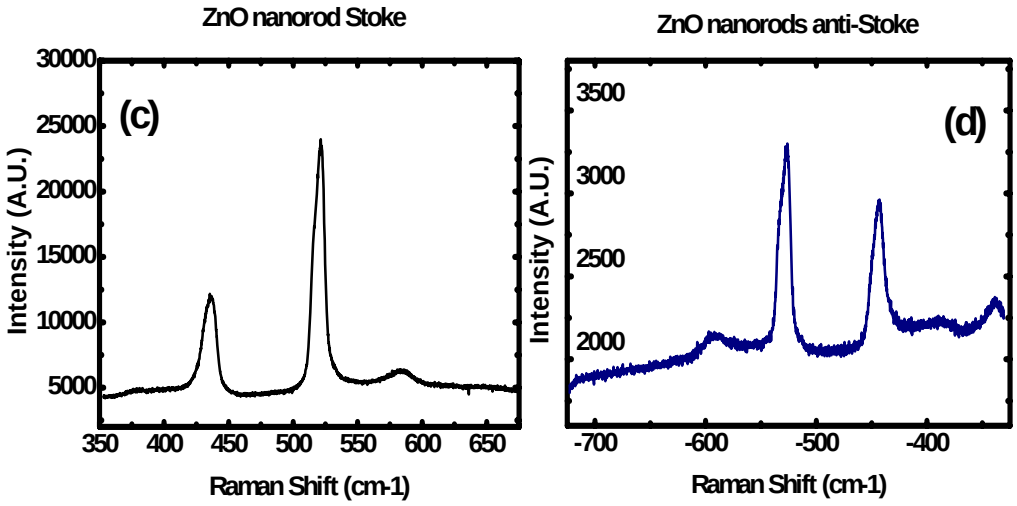

Figure 4.4 (a) and (b) show the collected Stokes and anti-Stokes Raman spectra of undoped ZnO bulk wafer; (c) and (d) show the Stokes and anti-Stokes spectra of aligned ZnO nanorods in order to estimate the corresponding peak shift due to the local laser heating.

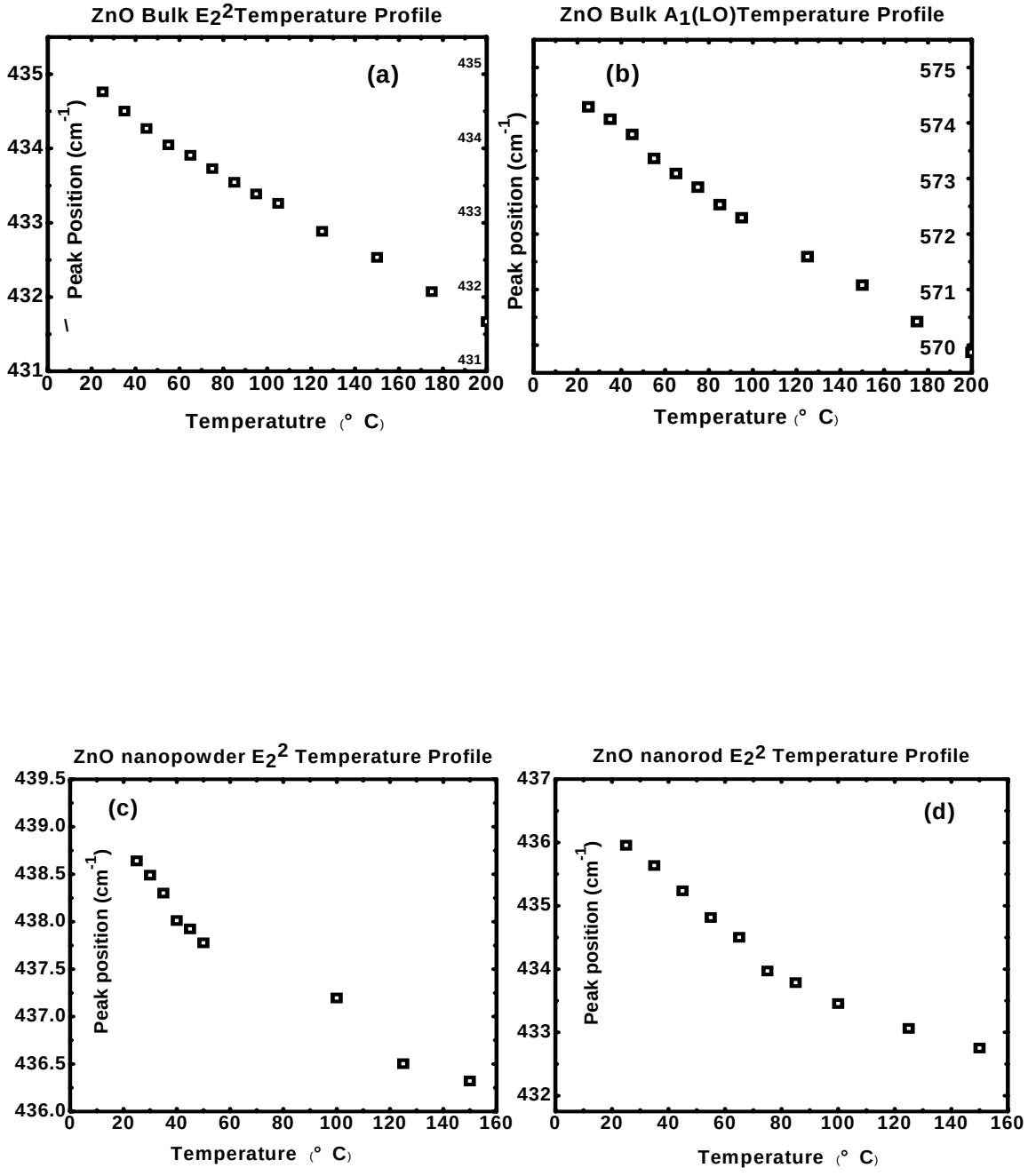

Figure 4.5 Corresponding phonon peak shift temperature profile of (a) bulk ZnO $E_2^{(2)}$

mode (b) bulk ZnO A_1(LO) mode (c) ZnO nanopowder E_2^2 mode and (d) aligned ZnO nanorods E_2^2 mode.

When the plasmon frequency ω_p approaches the frequency of LO phonon mode ω_{LO}, the collected oscillation of free-electron gas begins to couple with the LO phonon *via* its associated longitudinal electric field. The LO phonon plasmon coupled mode splits into two branches; high and lower frequency LPP modes are referred to as LPP^+ and LPP^- modes, respectively. Only the LPP^+ mode can be detected if the plasmon is under over-damped condition, i.e., $\omega_{p<}\gamma$. The LPP^+ mode in Raman spectrum shifts to higher frequency and an asymmetrical broadening occurs as the concentration of free electron increases. Therefore, the carrier concentration and can be extracted by analyzing Raman spectrum. The LO phonon interacts with laser beam via electro-optic mechanism and deformation potential and with plasmon through electro-optic mechanism and charge density fluctuation. The plasma frequency can be determined by fitting the coupled A_1(LO) plasmon-phonon peak through the following equation;

$$I(\omega) = const \bullet A(\omega) \bullet \mathrm{Im}[-\varepsilon(\omega)^{-1}], \qquad (4)$$

where ω represents the relative Raman shift, ϵ(ω) is the dielectric function, and A(ω) is the term that corresponds to the deformation potential and the electro-optic mechanism [138], and is expressed as follows;

$$A(\omega) = 1 + 2C\frac{\omega_{TO}^2}{\delta}[\omega_p^2\gamma(\omega_{TO}^2 - \omega^2) - \omega^2\Gamma(\omega^2 + \gamma^2 - \omega_p^2)] + C^2\{\omega_p^2[\gamma(\omega_{LO}^2 - \omega_{TO}^2) + \Gamma(\omega_p^2 - 2\omega^2)] + \omega^2\Gamma(\omega^2 + \gamma^2)\} \times \left(\frac{\omega_{TO}^4}{\delta(\omega_{LO}^2 - \omega_{TO}^2)}\right), \qquad (5)$$

where,

$$\delta = \omega_p^2 \gamma[(\omega\Gamma)^2 + (\omega_{TO}^2 - \omega^2)^2] + \omega^2\Gamma(\omega^2 + \gamma^2)(\omega_{LO}^2 - \omega_{TO}^2), \qquad (6)$$

where C is the Faust-Henry coefficient which can deduced from the ratio of the intensity of the LO to TO phonon modes in undpoed ZnO using the following equation [151];

$$\frac{I_{LO}}{I_{TO}} = (\frac{\omega_l + \omega_{LO}}{\omega_l + \omega_{TO}})^4 \frac{\omega_{TO}}{\omega_{LO}} \{1 + \frac{\omega_{TO}^2 - \omega_{LO}^2}{C\omega_{TO}^2}\}, \qquad (7)$$

where ω_l is the frequency of the laser, ω_p is the plasma frequency, ω_{LO} and ω_{TO} are the LO and TO phonon frequency for A_1 mode, respectively. Γ and γ represent the phonon and plasmon damping constants, respectively. The dielectric function $\epsilon(\omega)$ in equation (4) indicates the contributions from both the phonon and plasmon:

$$\varepsilon(\omega) = \varepsilon_\infty (1 + \frac{\Omega^2}{\omega_{TO}^2 - \omega^2 - i\omega\Gamma} - \frac{\omega_p^2}{\omega(\omega + i\gamma)}), \qquad (8)$$

Ω^2 is the simplification of ω_{LO}^2-ω_{TO}^2 and ϵ_∞ is the optical dielectric constant.

Equation (4) can be fully expressed and simplified by substituting the equations (5), (6) and (8) into it. The tunable parameters, ωp, γ, and Γ, can be obtained by fitting the experimental data with the equation (4). All the fitting result ωp, γ, and Γ need to be positive for meaningful physical definitions. The carrier concentration can be determined from the plasmon frequency ω_p by using the following expression;

$$\omega_p = \sqrt{\frac{4\pi n e^2}{\varepsilon_\infty m^*}}, \qquad (9)$$

where m* is the effective mass of the free carrier and is determined to be 0.23 m_e for ZnO. [152] Finally, mobility of electron can be obtained from plasmon damping constant γ as follows;

$$\gamma = \frac{e}{m^* \mu}, \qquad (10)$$

Table 4.1 shows the summary of the frequency of the ZnO Raman modes collected by other research group and ours. The frequencies of the TO and LO phonon modes were set to 378cm^{-1} and 574cm^{-1}, respectively, and the optical dielectric constant was set to 3.68[153] and C=6.4[154].

E_2-low	E_2-high	A_1(TO)	Quasi-A_1(TO)	E_1(TO)	Quasi-E_1(TO)	A_1(LO)	Quasi-A_1(LO)	E_1(LO)	Quasi-E_1(LO)	Ref.
101	444	380	395	398	413	579	585	591	585	[138]
102	439	379	--	410	--	574	--	591	--	[155] a-face
--	436	--	--	--	--	582	--	--	--	[147] QD
102	438	380	--	409	--	--	--	587	--	[156] film
102	437	379	--	410	--	--	--	591	--	[148] bulk
101	437	380	--	407	--	574	--	583	--	[157]
--	441	381	--	407	--	--	--	583	--	[158]
98	437.5	378	--	409.5	--	576	--	588	--	[145]
--	436	383	--	--	--	--	--	584	--	[159]
--	437	380	--	--	--	583	--	--	--	[160]
--	439	379	--	407	--	--	--	583	--	a-face ZnO bulk
--	436	375	--	--	--	576	--	--	--	c-face ZnO bulk

Table 4.1 Comprehensive **s**ummary of the frequency of the ZnO Raman phonon modes collected by other research group and ours.

The curve fitting results for the undoped bulk ZnO and the aligned ZnO nanorods are shown in Figure 4.6(a). The line shape analysis of the undoped bulk ZnO reveals a relatively low carrier concentration of $1.94\times10^{17}/cm^3$. This is corresponded to the $A_1(LO)$ frequency and FWHM of the coupled mode as shown in Figure 4.6(a). The frequency of the $A_1(LO)$ mode for the aligned ZnO nanorods shift to higher frequency of 585.18 cm^{-1} and the line shape becomes asymmetrically broadened to have the FWHM of 22.91 cm^{-1}. The fitting parameters and results are summarized in Table 4.2. The carrier concentration and mobility of the undoped bulk ZnO determined from the line shape analysis are $1.94\times10^{17}/cm^2$ and $108.87cm^2/V\text{-}s$, respectively. The carrier concentration and mobility of aligned ZnO nanorods obtained from the line shape analysis are $3.76\times10^{17}/cm^2$ and $84.76cm^2/V\text{-}s$, respectively.

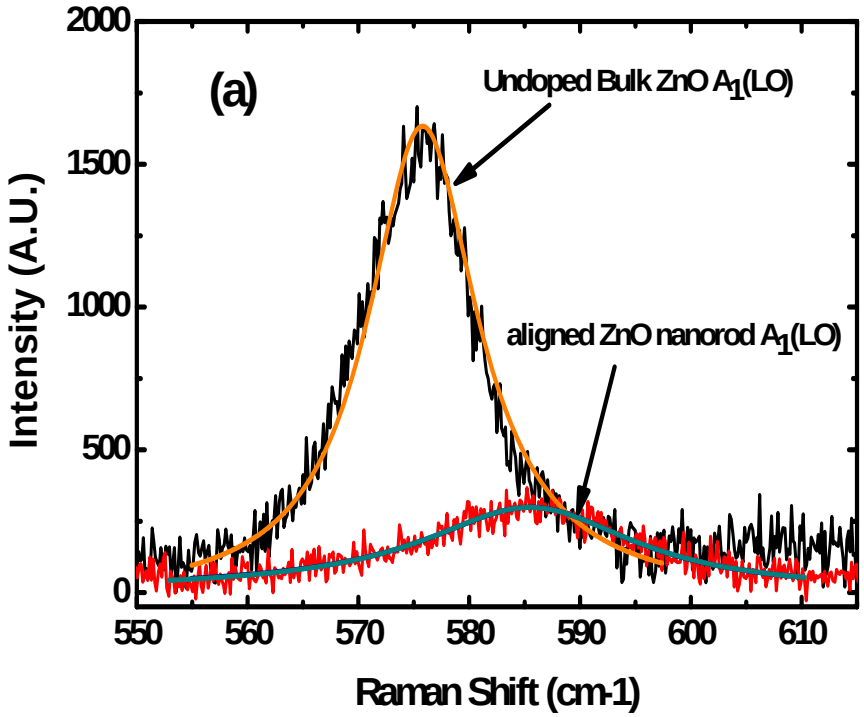

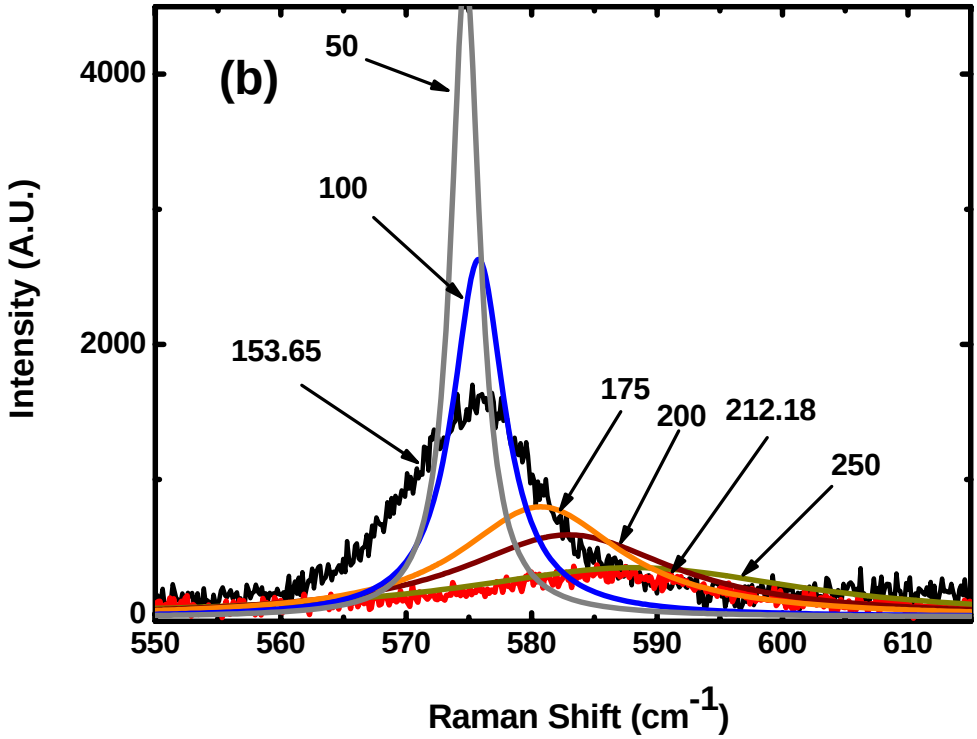

Figure 4.6 (a) The curve fitting results for the undoped bulk ZnO and the aligned ZnO nanorods; (b) experimental curve fitting results were studied by theoretical line analysis shape of LPP mode as a function of the plasma frequency.

	ω_p	Γ	γ	n_e (10^{17} cm^{-3})	μ (cm^2/V-s)	FWHM	A_1(LO)peak
Undpoed bulk ZnO	153.65	62.95	427.03	**1.94**	**108.87**	12.56	575.47
Aligned ZnO nanorods	212.18	8.19	548.22	**3.76**	**84.76**	22.92	585.18

Table 4.2 The fitting parameters and results of undoped bulk ZnO and aligned ZnO nanorods.

The mobility of the aligned ZnO nanorods is about 20% lower than that of the undoped bulk ZnO, which can be attributed from the enhanced surface scattering. Motayed *et al.* have studied this phenomena using electron backscattered diffraction (EBSD) and suggested that the mobility decreases in observed in the nanowire with intermediate diameter (120-180nm) might be related to grain boundary scattering. [161] The experimental curve fitting results were further studied by theoretical line shape analysis of LPP mode as a function of the plasmon frequency in Figure 4.6(b). The peak of the A_1(LO) reached its lowest limitation of 574cm^{-1} while ω_p is 50 cm^{-1} which correspond to the concentration of 2×10^{16}/cm^3. The LPP mode line starts to shift to higher frequency and asymmetrical line shape broadening occurs when ω_p is larger than 100cm^{-1}, as shown in Figure 4.6(b). The theoretical simulated curves as a function of different plasma frequency showed an excellent agreement with the experimental data. In order to understand what factor in the LPP curve fitting formula (eq. (4)) governs the line shape broadening and what factor dominants the peak shift due to increasing the plasma frequency. Equation (4) can be separated into an imaginary part that is responsible for dielectric function $\epsilon(\omega)$; and a real part, const•$A(\omega)$, that $A(\omega)$ corresponds to the deformation potential and the electro-optic mechanism. As the real part of equation (4) is varied by increasing the plasmon frequency and the imaginary part is set to a constant, shown in Fig. 4.7 (a), the slopes of the curve become larger as ω_p increases from 50 to 300 cm^{-1}. If the real part is set and the imaginary part was adjusted by increasing the Plasmon, as shown in Fig. 4.7(b), the shape of the curve starts to broaden as Plasmon frequency increases. Fig. 4.7 (c) is the LPP curve simulation as a function of plasmon

frequency. To sum up, the real part of the LPP equation mainly responsible for the peak shift due to increasing plasmon frequency and the imaginary part is the dominant factor of curve broadening.

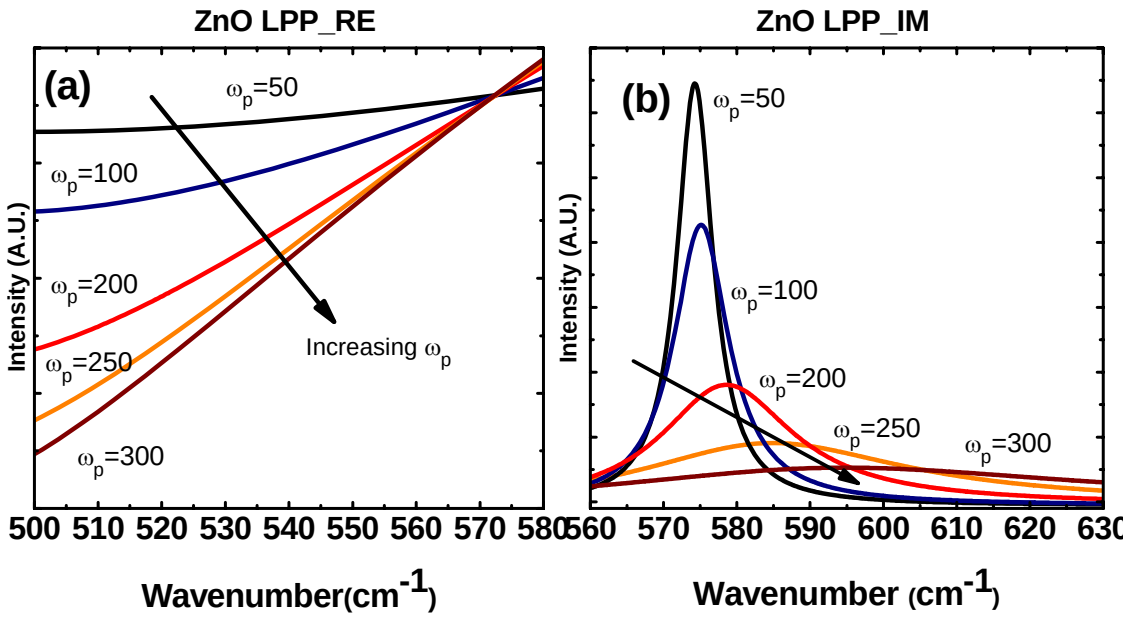

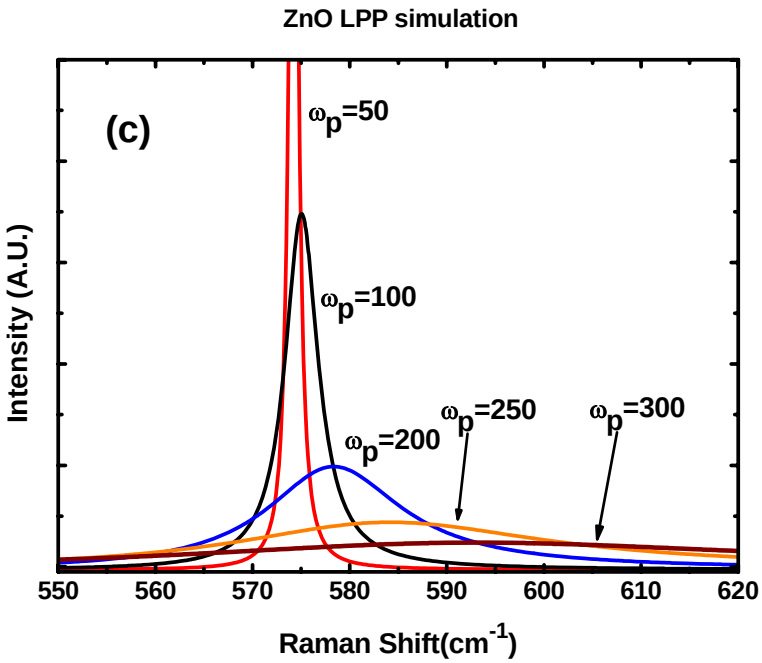

Figure 4.7 LPP curve simulation as a function of plasmon frequency from 50 to 300 cm^{-1} (a) Real part curve simulation of LPP equation; (b) imaginary part curve simulation of LPP equation; (c) Real and imaginary parts of LPP curve simulation.

Furthermore, Capacitance-Voltage (C-V) measurement in Figure 4.8 of undoped bulk ZnO was also performed to compare the carrier concentration results obtained from both Raman scattering and C-V electrical measurement methods. The bulk sample used for this work was Zn-terminated n-type ZnO substrate purchased from Eagle Picher. Prior to metal deposition and patterning, the bulk ZnO sample surfaces were ultrasonically degreased in trichloroethylene (TCE), acetone, and methanol, and rinsed in de-ionized water for 5 min in each step (referred to here as "conventional cleaned"). The conventional cleaned ZnO sample was further treated using a boiling hydrogen peroxide (referred as "surface treated"). [162] The Platinum (Pt) Schottky contacts with three

different dot sizes, 50μm, 150μ, and 300μm, were fabricated through photolithography lift-off process. The Pt layer with the thickness of 100nm was sputtered under the condition of 100W, 25sccm Ar, 5.1 mTorr, for 300sec at room temperature. Ti/Au contact was used as backside ohmic contact. [163] The carrier concentration of undoped bulk ZnO was in the range of 1.25-2.5×10^{17}/cm^2, which confirmed that the LPP fitting result is very reliable.

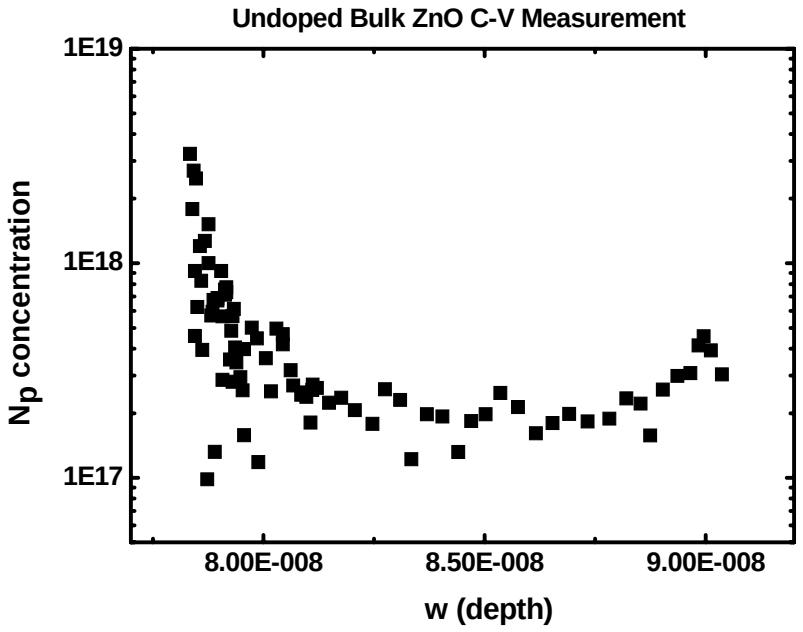

Figure 4.8 Carrier concentration profile of undoped bulk ZnO measured using C-V method.

Conclusion

Electronic properties of undoped bulk ZnO and well-aligned ZnO nanorods have been investigated using micro-Raman spectroscopy. It was found by Raman spectroscopy that

the ZnO nanorods are stress-free. The carrier mobility as well as the carrier concentration of undoped bulk ZnO and the aligned ZnO nanorods were determined by the line shape analysis of the A_1(LO) phonon-plasmon coupled mode. The local laser heating effect was considered using the ratio of E_2 mode Stokes to anti-Stokes Raman peak intensity. It is important to carefully consider laser heating effect in determining the frequency of the uncoupled LO phonon mode before performing the line shape analysis since the LO phonon peak position depends on both the temperature and the LO phonon-plasmon coupling. The mobility and carrier concentration of the undoped bulk ZnO obtained from the line shape analysis are 108.87cm^2/V-s and $1.94\times10^{17}/cm^3$, respectively. The mobility and carrier concentration of aligned ZnO nanorods obtained from the line shape analysis are 84.76cm^2/V-s and $3.76\times10^{17}/cm^3$, respectively. The C-V measurement of undoped bulk ZnO carrier concentration also further confirmed the concentration result obtained from LPP mode line shape analysis. The mobility of the aligned ZnO nanorods is about 20% lower than that of undoped bulk ZnO, which can be as attributed to the enhanced surface scattering due to a low-dimension of the nanorod structure.

Chapter 5

Micro-Raman diagnosis of phonon lifetime of bulk ZnO, one Dimensional Vertically aligned ZnO nanorods, and ZnO nanopowder

5.1 Introduction

Group III-V and II-IV wide band gap compound semiconductors have been considered as the promising materials for nano-scale electronics and optoelectronics device applications. Numerous scientific investigations issues of improving the crystal quality as well as diagnosis techniques of those wide band gap semiconductors have been intensively proceeded in order to well-controlled those wide band gap related devices fabrication and their performance. The special interest in ZnO has been restrengthened by its potential applications in transparent electronics and UV optoelectronic devices. Its large exciton binding energy of 60meV makes it highly attractive for applications as ultraviolet light emitting emitter, where it may become an advantageous alternative to GaN. [164] Profound knowledge of the vibrational properties of this material is necessary to determine the transport characteristics and interaction of phonon with the free carrier, both of which have great impact on optoelectronic device performance. Optical spectroscopy analysis is very powerful technique since it provides non-contact measurement and easy operations. Raman spectroscopy has been widely used for

analyzing the wide band gap semiconductors properties such as carrier concentration, phonon interaction and dynamics. [165,166,167,168] The interaction between phonon and free carriers degrades the performance of the devices; however, the phonon interactions can also be utilized to engineer certain laser devices. [169,170] The phonon lifetime of wide band gap semiconductors is important to be characterized and one convenient method is to employ Raman spectroscopy since the phonon lifetime can be obtained from the Raman phonon linewidth. Crystalline diamond, gallium nitride (GaN), silicon (Si), and indium nitride (InN) are the materials that have been diagnosed via their Raman linewidth. [163,165,171,172] Bergman *et al.* have reported the phonon lifetime of AlN and GaN wurtzite structure. They claimed that the lifetimes of the Raman phonons of GaN and AlN exhibit two regimes: the long lifetime range of the E_2^1 phonons and the much shorter lifetime regime that includes E_2^2, E_1(TO), and A_1(TO) phonons. Their results are also consistent with the A_1(LO) mode lifetime model that predicts a three-phonon anharmonic process in which the A_1(LO) decays into an E_1(TO) phonon and a LA phonon.[163]

The theory of spectral line shape of a collected spectrum signal in a dispersive media predicts the line shape to be Lorentzian and the linewidth, which is a parameter determining the damping effect, to be inversely proportional to the lifetime of the spectrum signal.[173] The line shape is expected to be infinitesimally narrow for an ideal harmonic crystal. However, experiments have shown that the Raman linewidth of most materials exhibits a finite width indicating the presence decay channels that shorten the phonon lifetime. [174,175] The main lifetime shortening mechanism in semiconductor is

via anharmonic interaction. [172] The principle of anharmonic interaction is caused by the cubic anharmonicities that results in the splitting of an optical phonon into two acoustic phonons of opposite momentum. An optical mode can interchange energy with other lattice modes and maintain the thermal equilibrium energy constant because of the anharmonicity of the lattice force. In this concept, an optical mode behaves similarly to an acoustic mode. The rate at which an acoustic mode approaches equilibrium can be related to relaxation time which enters the explanation for the thermal conductivity; optical modes, however, do not contribute substantially to thermal conductivity. [173] The relaxation time of optical phonon mode determines the linewidth in infrared absorption spectrum, in Raman spectrum, and in inelastic neutron scattering experiments. Impurities and defects are contained in all semiconductors and it was found that those imperfactions affect the Raman line width. Therefore, the contributions of impurities and defects of lifetime shortening need to be taken into consideration.

In polar semiconductors, carriers are excited high above the conduction band edge and relax toward their ground state mainly by Frohlich interaction with the longitudinal optical phonons. [176] This dynamics of the phonon population strongly affects the performance of high speed optoelectronic devices. For materials with a sufficiently long longitudinal optical (LO) phonon lifetime, “hot phonon” effects greatly slow down carrier relaxation, as is the case in GaAs.[5] ZnO belongs to wurtzite type crystal structure of the space group C_{6v}^4 with two formula units in the primitive cell. The zone center optical phonons can be classified as $\Gamma_{opt}=A_1+E_1+2E_2+2B_1$. The A_1 and E_1 are polar modes and are both Raman and infrared active. The E_2 modes are nonpolar and Raman active only.

The B_1 modes are silent modes. The Raman modes investigated in this study are the $E_2^{(2)}$, $E_1(TO)$, $A_1(TO)$ and $A_1(LO)$. The $E_2^{(2)}$ mode exhibits a visibly asymmetric line shape which can be attributed to anharmonic interaction with transverse and longitudinal acoustic phonon combinations in the vicinity of K point, where the two-phonon density of states displays a sharp edge around the $E_2^{(2)}$ frequency. [177] The high frequency $E_2^{(2)}$ mode is mainly involves O motion, and O is nearly isotopically pure. However, the low frequency $E_2^{(1)}$ mode result is not shown here because the limitation of the apparatus. The low frequency $E_2^{(1)}$ mode, involving mainly Zn motion, exhibits an extremely narrow phonon linewidth. The lattice dynamics of ZnO is still rather limited, as few experimental data are available on phonon dispersion in this material. Detailed measurements of the optical phonon branch by inelastic neutron scattering are still lacking. Only recently, theorectical have *abinitio* density-functional theory (DFT) calculations of lattice dynamical properties have been published. [178] Recently, the low-frequency E_2 phonon lifetime has been measured in ZnO by means of impulsive stimulated Raman scattering experiment and has been found to be longer than 200ps at low temperature. [179] This extraordinary characteristic has been considered to have special applications in quantum cryptography and quantum computing. [176] In this work, we present the study of the room temperature phonon lifetimes of the Raman phonon modes in undoped bulk zinc oxide (ZnO) single crystal, aligned ZnO nanorods, and nanopowder. We observed that the $E_2^{(2)}$ mode Raman linewidth broadens as the dimensionality decreases from bulk to one dimensional nanorods and then to nanopowder.

The $E_2^{(2)}$ mode phonon lifetime decreases from 0.6ps to 0.5ps and then 0.4 ps as the dimensionality of the ZnO decreased.

5.2 Experiment

Vertically aligned ZnO nanorods were grown on p-Si substrate using a thermal chemical vapor deposition (CVD). An ultra-thin layer (with thickness of ~20 nm) of zinc was sputtered on the p-type Si substrate before synthesizing the ZnO nanorods. The as-sputtered samples were loaded into the furnace box at the temperature of 400°C, and were annealed for 8 hours at 1 atmosphere in order to oxidize Zn layer to form ZnO. All the samples were ultrasonically cleaned in pure methanol for 10 minutes, followed by immersing the samples in methanol with a suspension of zinc nanopowder for additional 30 minutes. No special catalysis was used in nanorod growth. All the as-prepared samples were loaded on top of an alumina boat containing a small amount of Zn powder. Meanwhile, additional alumina boat containing very little amount of Zn powder was inserted into the end of a smaller quartz tube before loading alumina boat which has the samples on it. Then, the temperature of the CVD reactor was elevated to 500°C with a ramping rate of 5 °C/ min. Argon (Ar) and oxygen (O_2) were used as the carrier and reactant gases for ZnO nanorods growth, respectively. The flow rate of Ar and O_2 were 88 sccm and 8 sccm, respectively. The growth of ZnO nanorods were performed at 50 Torr for 60 minutes. The undoped a-face and c-face bulk ZnO single crystal were purchased from Eagle Picher. The ZnO nanopowder of the size smaller than 5nm is purchased from Sigma Aldrich. Table 5-1 below is the summery of allowed Raman modes for the scattering geometry.

Scattering geometry	E_2	$A_1(LO)$	$A_1(TO)$	$E_1(LO)$	$E_1(TO)$
$z(xx)\bar{z}$	**A**	**A**	--	--	--
$z(xy)\bar{z}$	**A**	--	--	--	--
$x(yy)\bar{x}$	**A**	--	**A**	--	--
$x(zy)\bar{x}$	--	--	--	--	**A**
$x(zy)y$	--	--	--	**A**	**A**

Table 5-1 Symmetry allowed Raman modes for the scattering geometries.

The surface morphologies of the samples were studied using a field-emission scanning electron microscope (FE-SEM, JOEL JSM-7000). The crystal structures of the samples were characterized by X-ray diffraction (XRD) using a Rigaku Miniflez powder x-ray diffractometer with Cu Kα radiation. Micro-Photoluminescence (PL) and micro-Raman spectroscopy were performed at room temperature using 325 nm and 441.6 nm laser line from a He-Cd laser (Kimmon Electric) with a spectrometer (Jobin-Yvon) integrated with a diffraction grating with a 3600 lines/mm groove density. Both the spectra were collected using a spectrometer with a thermoelectrically-cooled charge coupled device (CCD) detector. The laser beam was focused onto a spot of approximately 5 μm in diameter on the sample surface. Backscattering geometry was used for Raman scattering measurement. The spectral resolution of the grating is 0.2 cm^{-1}.

In order to observe the phonon lifetime via the Raman spectrum linewidth, the linewidth has to be calibrated for the contribution of the instrumental bandpass

broadening. The Raman spectra had been collected at successive slit width ranging from 50μm up to 400μm. The measured linewidth values W_M are plotted as a function of the slot width W_S and extrapolated to the zero-slit value W_P via the relation, [180,181]

$$W_M = \sqrt{W_P^{\,2} + (W_S \times MLD)^2}\,, \quad (1)$$

The second term in Eq. (1) is the instrumental bandpass, i.e., the slit width multiplied by the monochromator linear dispersion (MLD), 0.022 cm^{-1}/mm. Eq. (1) is an approximation that can only be applied when the line shape of the instrument bandpass can be approximated by a Gaussian and hat of the phonon by a Lorentz. [178, 179] The zero-slit Raman phonon linewidth arises from a convolution of all broadening mechanisms in which mainly due to the lifetime shortening mechanisms occurring in a given crystal.

5.3 Results and Discussion

Figure 5.1 (a) and (b) are the SEM images of the as-grown vertically aligned ZnO nanorods grown by using thermal CVD process The SEM reveals that the well-aligned ZnO nanorods were uniformly grown on a relatively large area of the p-type Si substrate. ZnO is a wurtzite crystal possessing hexagonal crystal structure and the hexagonal shape can be clearly observed with higher resolution SEM micrograph.

PL behavior of ZnO exhibits a band edge UV emission peak and a broad visible emission band due to the deep level intrinsic and/or extrinsic defects. [182] The mechanism of the broad visible emission, especially the blue-green emission, is intended to be explained by oxygen vacancies (V_O), *i.e.*, singly ionized [183] or doubly ionized oxygen vacancy. [184]

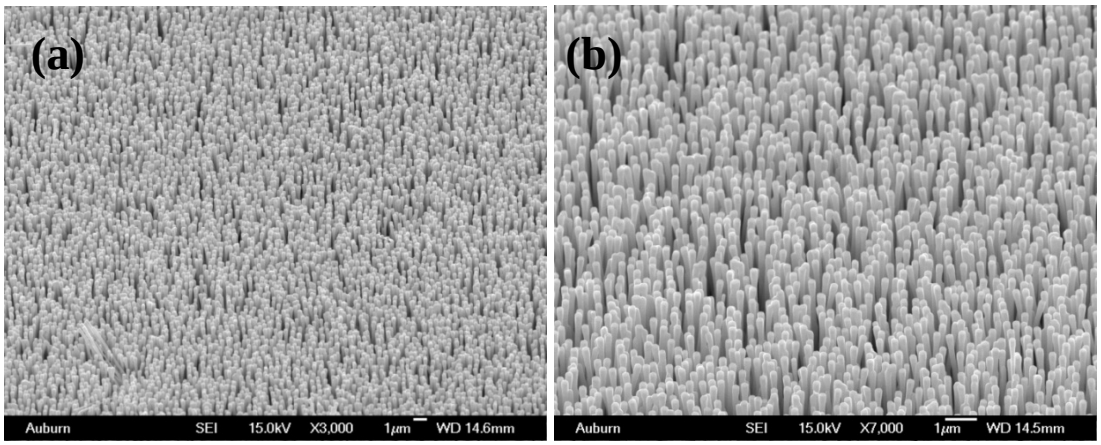

Figure 5.1 SEM images of well-aligned ZnO nanorods with (a) low resolution and (b) high resolution.

The green visible luminescence at 500nm (2.48eV) is relative to the growth environment, the oxygen content during the growth, and the oxygen defect levels originated from crystal incubation. Primarily, the visible emission from the sample deposited without using oxygen gas was dominated by blue-green band emission at 2.34 eV. However, the blue-green band emission was greatly reduced to zero (free green band) when oxygen gas was induced during the deposition. A high local oxygen concentration will result in a significantly different photoluminescence spectrum: the blue-green band has given away to relatively strong violet-blue emission bands and a broad band at yellow-orange-red range. It was usually observed that the blue-green emission band was a result of the oxygen deficiency during the growth process, while the yellow-orange emission bands were presented in samples grown with excess oxygen supply. [185, 186] The PL spectrum of aligned ZnO nanorods is shown in Figure 5.2. A strong ultra-violet near band edge (NBE) emission is observed at 382 nm and no visible luminescence was collected. It further demonstrated that our aligned ZnO nanorods are nearly defects free

since no broad visible emission is observed. The FWHM of the ZnO nanorods is approximately 15.31 nm which is 3.38 nm broader than the undoped bulk ZnO wafer. However, in the visible region from 450 to 600 nm, ZnO nanorods PL spectrum shows no broad band in the visible regime as compared to the PL spectra of bulk ZnO and nanopowder.

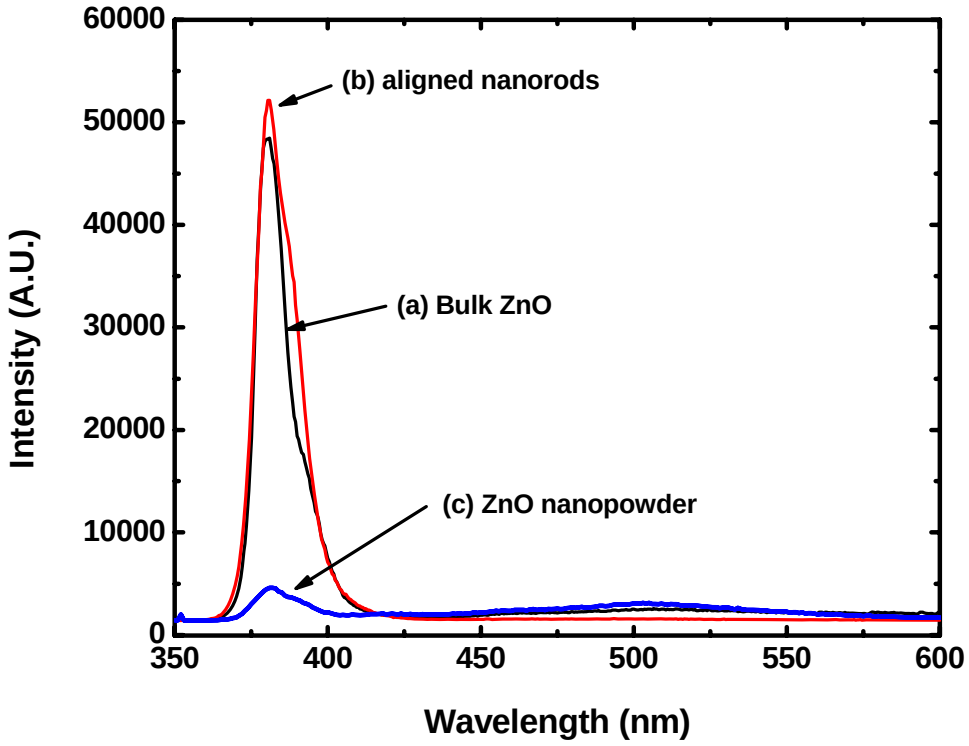

Figure 5.2 PL spectra of (a) undoped bulk ZnO (b) aligned ZnO nanorods (c) ZnO nanopowder.

Due to the extremely large surface-to-volume ratio of nanopowder the local heating from the laser beam is intensively severe. A natural density filter (NDF) needs to apply in front of the laser existence port in order to reduce the laser intensity. Figure 5.3 shows the

spectra of ZnO nanopowder without NDF added, with 5% NDF and a 0.1% NDF added. The NBE UV emission peak shifts from 380.5 nm to 415.3 nm while the NDF is added or not. The emission peak shifts to higher wavelength corresponding lower energy level is due to the temperature elevating on the surface of the nanopowder up to hundreds of Celsius degree that provides high enough thermal energy. The higher the thermal vibrational energy is the easier the emission peaks shifts to the right.

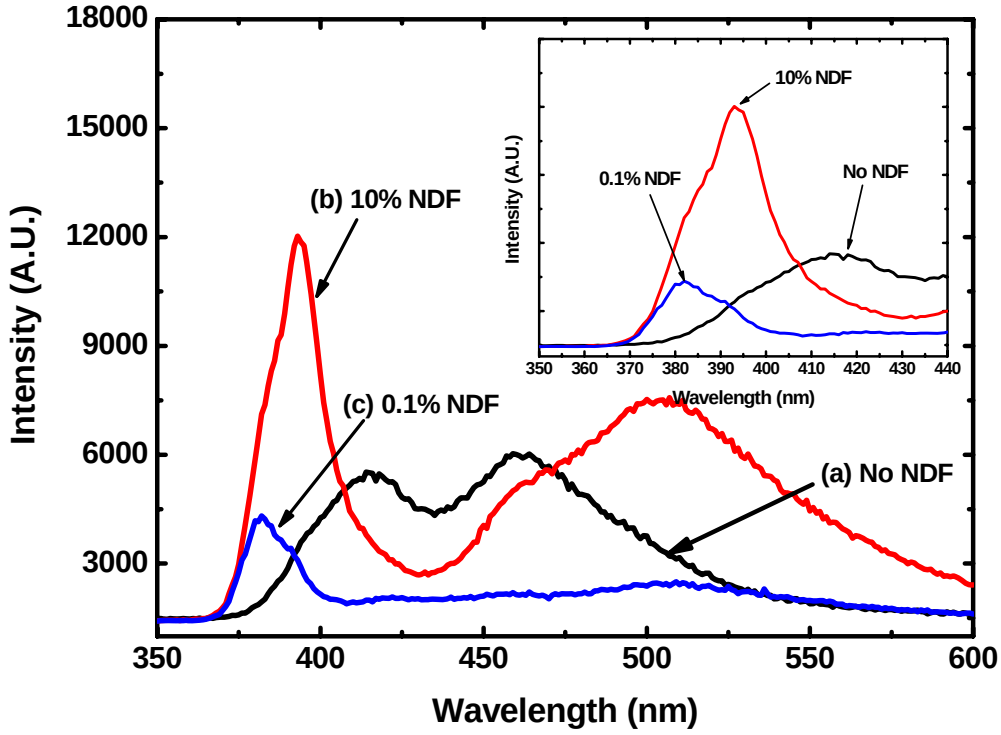

Figure 5.3 PL spectra of ZnO nanopowder using (a) no NDF (b) 10% NDF and (c) 0.1% NDF. The inset of the PL magnified the NBE emission of three different types of NDF conditions.

Ramon Cusco *et al*. have reported a table of the first and second-order Raman frequencies that is shown in Table 5.2. [174,187] The wave vector conservation restricts the phonons involved in first-order Raman scattering to those with **k**≈0, phonons from the entire Brillouin zone take part in second-order Raman scattering. Second-order Raman spectra usually exhibit feature-rich structures that are demonstrated by the phonon density of state (DOS) and by the selection rules of the two-phonon scattering processes. [174] Selection rules for two-phonon Raman scattering in wurtzute structure crystal were reported by Siegle et al. [188]

Frequency (cm^{-1})				
Our data	Ref. [185]	Symmetry	Process	Brillouin zone points/lines
99	101	E_2	E_2^{low}	Γ
203	208	$A_1,(E_2)$	2TA; $2E_2^{low}$	$L,M,H;\Gamma$
284		A_1	$B_1^{high}-B_1^{low}$	Γ
333	332	$A_1,(E_2,E_1)$	$E_2^{high}-E_2^{low}$	Γ
378	380	A_1	A_1(TO)	Γ
410	408	E_1	E_1(TO)	Γ
438	437	E_2	E_2^{high}	Γ
483		A_1	2LA	*M-K*
536	541	A_1	$2B_1^{low}$; 2LA	$\Gamma;L,M,H$
574	574	A_1	A_1(LO)	Γ
590	584	E_1	E_1(LO)	Γ
618		A_1	TA+TO	*H,M*
657		E_1,E_2	TA+LO	*L,H*
666		A_1	TA+LO	*M*
700		A_1	LA+TO	*M*
723		A_1	LA+TO	*L-M*
745		A_1	LA+TO	*L-M*
773		A_1	LA+TO	*M,K*
812		A_1	LA+LO	*L,M*
980	990	A_1	2TO	*L-M-K-H*
1044		A_1	TO+LO	*A,H*
1072	1080	A_1	TO+LO	*M,L*
1105		A_1	2LO	*H,K*
1158	1160	A_1	$2A_1$(LO),$2E_1$(LO); 2LO	Γ;*A-L-M*

Table 5.2 Room temperature frequencies and symmetries of the first- and second-order Raman spectra observed in ZnO and their assignments. Parenthesis indicates symmetries

that although being present in the spectra display a much lower intensity than the dominant one. [174]

The $E_2^{(2)}$ mode possesses a visibly asymmetric line shape with a low frequency tail, which can be clearly clarified in Figure 5.4. This type of line-shape broadening is then mostly determined by anharmonic phonon-phonon interactions. This can result in strongly distorted peaks when resonant interaction with a band of second-order combinations takes place (Fermi resonance), as is the case for the GaP TO mode, where the presence of van Hove-type singularities in the DOS of the TA+LA combination band gives rise to a highly asymmetric TO mode. [189,190] A similar situation occurs for the ZnO $E_2^{(2)}$ mode, while the frequency lies close to a ridge-like structure of the two-phonon DOS corresponding to TA+LA combinations in the vicinity of the K point. [191]

The A_1(LO) and E_1(LO) phonon modes of ZnO is very close to each other. Their line shape analysis is not affected by variations of the phonon self-energy and a simpler model can be used to analyze their temperature dependence Raman spectra. Inspection of the phonon dispersion curves [192] suggests that the main decay channel for these phonon modes involve the decay of the longitudinal optical mode into a mode of the transverse acoustic branches and a mode of the transverse optical branches. The anisotropy of the force constants in the wurtzite structure causes the transverse branches to split along the main symmetry lines of the Brillouin zone. Therefore, modes from different split TO and TA branches can provide decay channels for both the A_1(LO) and E_1(LO) phonon modes. In the TA region, the phonon DOS presents a maximum at 100 cm^{-1}, with a significant contribution from the lower TA branch along *L*-*M*. A secondary

maximum can be observed at ≈120 cm^{-1} with an important contribution from the nearly flat A branch along *L-M*. In the TO region, the phonon DOS exhibits a maximum at ≈455 cm^{-1} and a secondary maximum at ≈490 cm^{-1}, both of which contain important contributions from the split TO branches along *L-M*. Therefore, the A_1(LO) mode (574 cm^{-1}) decays most probably into pairs of TO and TA modes with frequencies around 455 and 120 cm^{-1}, respectively, whereas the corresponding decay frequencies for the E_1(LO) mode (590 cm^{-1}) are around 490 and 100 cm^{-1}.

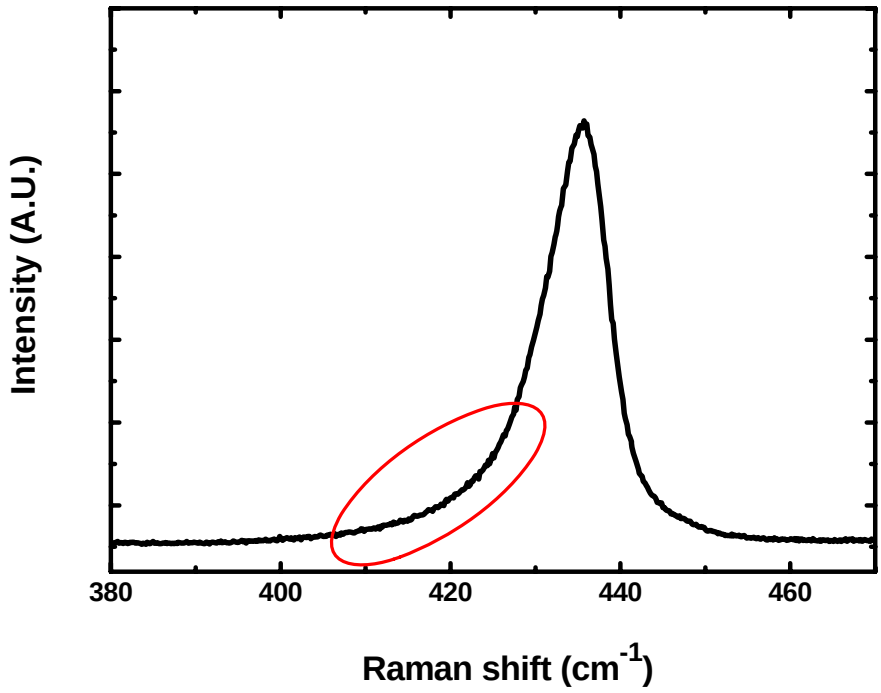

Figure 5.4 the $E_2^{(2)}$ mode possesses a visibly asymmetric line shape with a low frequency tail, which can be clearly clarified in the red circle.

The most usual method to analyze the decay channel is temperature dependence Raman spectroscopy. Assuming that the most relevant decay channel is generalized

Ridley channel with the main contributions clustered around ω_1 and ω_2, the temperature dependent FWHM of the phonon mode can be diagnosed by, [193]

$$\Gamma(T) = \Gamma_0 + A[1 + n(\omega_1, T) + n(\omega_2, T)] \qquad (2)$$

where Γ_0 is a background contribution due to impurity and/or defect scattering and isotropic broadening, A is the anharmonic coefficient, and n(ω, T) is the Bose-Einstein distribution function. The temperature dependence of the frequency of the phonon mode can be written as:

$$\omega(T) = \omega_0 + \Delta_0(T) + B[1 + n(\omega_1, T) + n(\omega_2, T)] \qquad (3)$$

where Δ_0(T) is the thermal expansion shfit and B is the anharmonic coefficient. Ramon Cusco *et al.* have measured the Raman shifts and linewidth of the A_1(LO) mode and fitted with equation (2) and (3) above with ω_1=120cm^{-1} and ω_2=455cm^{-1}. The adjustable parameters Γ_0, A, ω_0, and B were found to be 1.3cm^{-1}, 3.7cm^{-1}, 581.4cm^{-1} and -2.1cm^{-1}, respectively in there fitting result. For E_1(LO) phonon mode, the Raman shifts and linewidth were fitting with equation (2) and (3) with ω_1=100cm^{-1} and ω_2=490cm^{-1}. The fitting results, Γ_0, A, ω_0, and B, were found to be 2.8 cm^{-1}, 3.3 cm^{-1}, 595 cm^{-1}, -1.7cm^{-1}. [174] The E_1(LO) shows a wider linewidth that implies a higher value of Γ_0 and suggested that the E_1(LO) is more strongly affected by impurities and/r defect scattering than A_1(LO) mode. As the incorporation of defects in ZnO is known to be highly anisotropic that can be related to a possible anisotropy distribution of defects and the fact that E_1(LO) mode has an in-plane atomic motion whereas the atomic motion of the A_1(LO) is belongs to c axis.

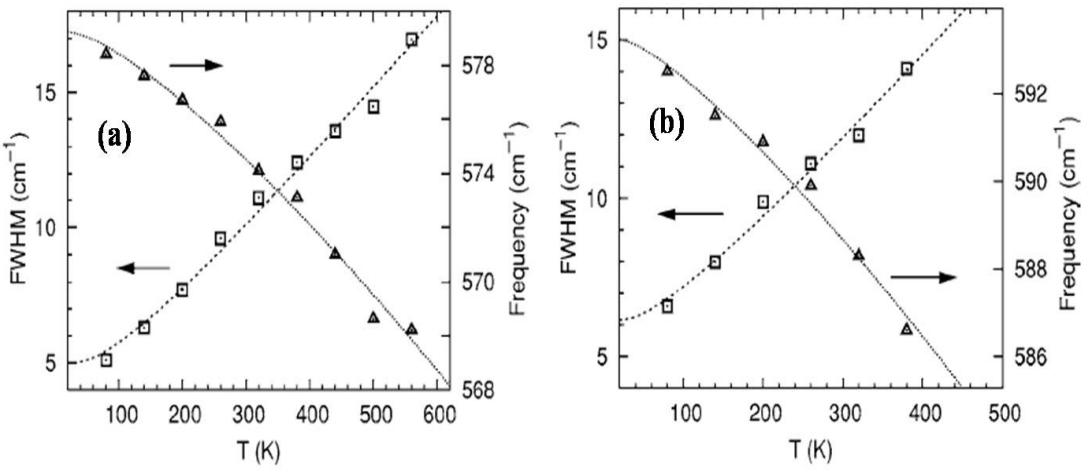

Figure 5.5 (a) measured values of frequency (triangles) and linewidth (squares) of the A_1(LO) mode for temperature in the range of 80-560K. The dotted lines are fits of Γ(T) and ω(T) given by equation (2) and (3) (b) measured values of frequency (triangles) and linewidth (squares) of the E_1(LO) mode for temperature in the range of 80-380K. The dotted lines are fits of Γ(T) and ω(T) given by equation (2) and (3). [174]

In order to calculate the phonon lifetime via the Raman spectrum linewidth, the linewidth were plotted as a function of the slit size and a curve fit was generated using equation (1). Figure 5.6 shows the typical Raman spectra, which is collected under z(-,-)z backscattering geometry, of a-face and c-face undoped bulk ZnO by the collecting slit size of 100μm. Figure 5.7 is the deconvoluted spectrum of a –face undoped ZnO in the range of 350-460cm^{-1}. In the spectrum the A_1(TO), E_1(TO), and $E_2^{(2)}$ modes are at 378, 409, and 438cm^{-1}, respectively.

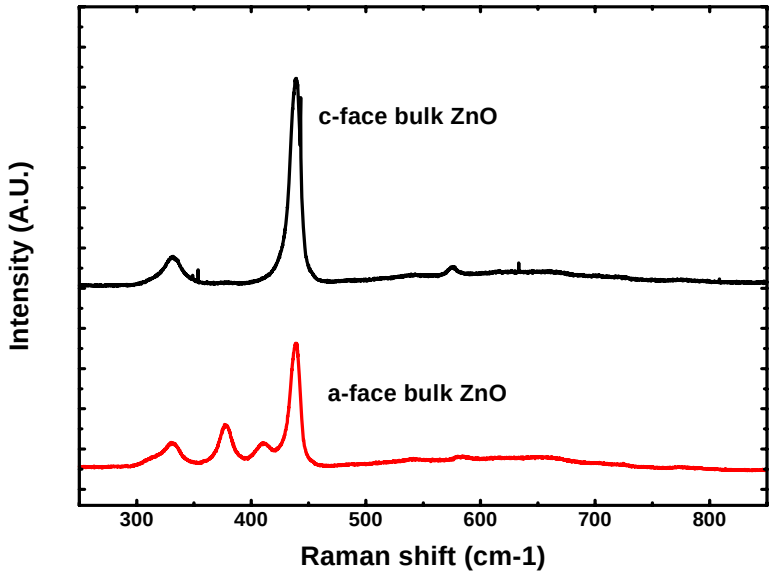

Figure 5.6 The typical Raman spectra, which is collected under z(-,-)z backscattering geometry, of a-face and c-face undoped bulk ZnO by the collecting slit size of 100μm.

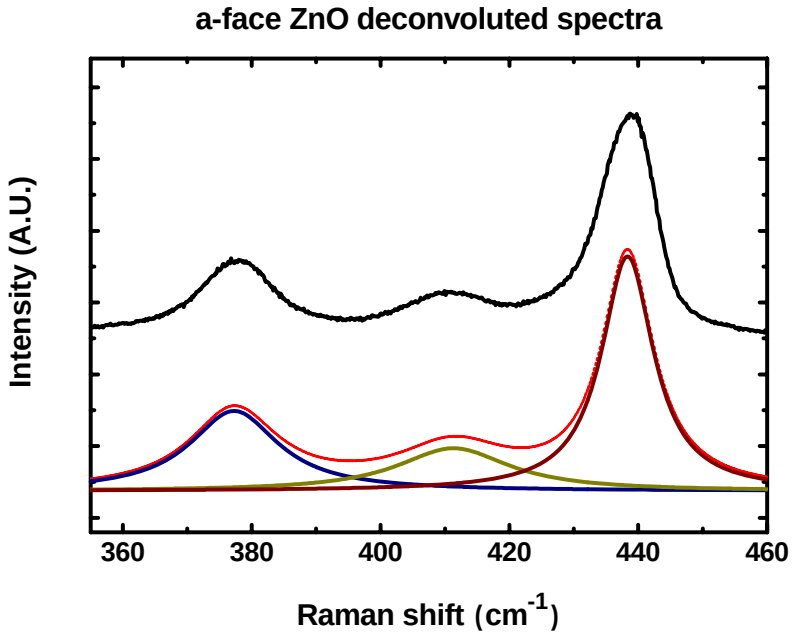

Figure 5.7 the deconvoluted spectrum of a –face undoped ZnO in the range of 350-460cm^{-1}.

The phonon lifetime can be derived from the Raman spectra via the energy-time uncertainty relation,

$$\frac{1}{\tau} = \frac{\Delta E}{\hbar} = 2\pi c\Gamma \qquad (4)$$

where ΔE is the uncertainty in the energy of the phonon mode, ħ=5.3×10^{-12} cm^{-1}s is the Planck constant, and Γ is the FWHM of the Raman peak in units of cm^{-1}. Figure 5.8 shows the Raman linewidth results of a-face, c-face undoped bulk ZnO, aligned ZnO and ZnO nanopowder data with a curve fitting using equation (1). The phonon lifetime of $E_2^{(2)}$ mode at different dimensionality shows a degradation from the longest lifetime 0.61ps of undoped a-face bulk ZnO down to 0.416ps of ZnO nanopowder. Phonon lifetime is greatly influenced by (1) anharmonic decay of the phonon into two or more phonons so that energy and momentum are conserved, with a characteristic decay time τ_A and (2) perturbation of the translational symmetry of the crystal by the presence of impurities, defects and isotropic fluctuations, with a characteristic decay time τ_I. The phonon lifetime deduced from the Raman measurement is clarified to be as followed,

$$\frac{1}{\tau} = \frac{1}{\tau_A} + \frac{1}{\tau_I} \qquad (5)$$

Separating the contribution of the both mechanisms is difficult, but estimation of the characteristic decay time is associated with impurities from the value of the Γ_0 parameter provided by the FWHM temperature dependence fits. The mechanism of the lifetime time shortening due to the lower dimensionality is still unclear but it may be caused via

anharmonic decay. The defects of aligned ZnO and nanopowder should be less than the undoped bulk ZnO since the PL spectrum shown in Figure 5.2 reveals a less severe defect-related emission as compared to that of undoped bulk ZnO. Therefore, the lifetime shortening contributes from the impurities defect scattering is much less than the anharmonic decay of phonon via different decay channels. Table 5.3 summarized the results for each different ZnO samples the zero slit linewidth is presented along with the calculated lifetime for each of the Raman modes. From Figure 5.8 (a), E_1(TO) exhibits the shortest lifetime of 0.35 ps as compared to other phonon mode, which is a good agreement of Ramon Cusco *et al.'s* results. They demonstrate that polar E_1 modes display the shortest τ_I. The fact that the E_1 modes have a polar character allows a Frohlich interaction with charged impurities and defects. [194] They claimed that because of owing to a possible anisotropy in the distribution of defects such interaction could affect the E_1 modes lifetime more severely than A_1 modes lifetime, as the E_1 has in-plane polarization, whereas the A_1 modes are polarized along the c axis. The A_1(LO) lifetime of aligned nanorods shows the shortest lifetime, 0.29 ps, among all the phonon modes that have been measured. The A_1(LO) mostly undergoes an anharmonic decay channel of a TA+TO mode. The A_1 and E_1 modes of nanopowder exhibit a mixing character due to the randomly oriented nanopowder was sprayed on a metallic substrate that originates severe scattering light and enormous diffusive light. The A_1 and/or E_1 that have been collected are mixing A_1 and E_1 mode, which cannot be relied on, instead of pure A_1 and E_1 mode.

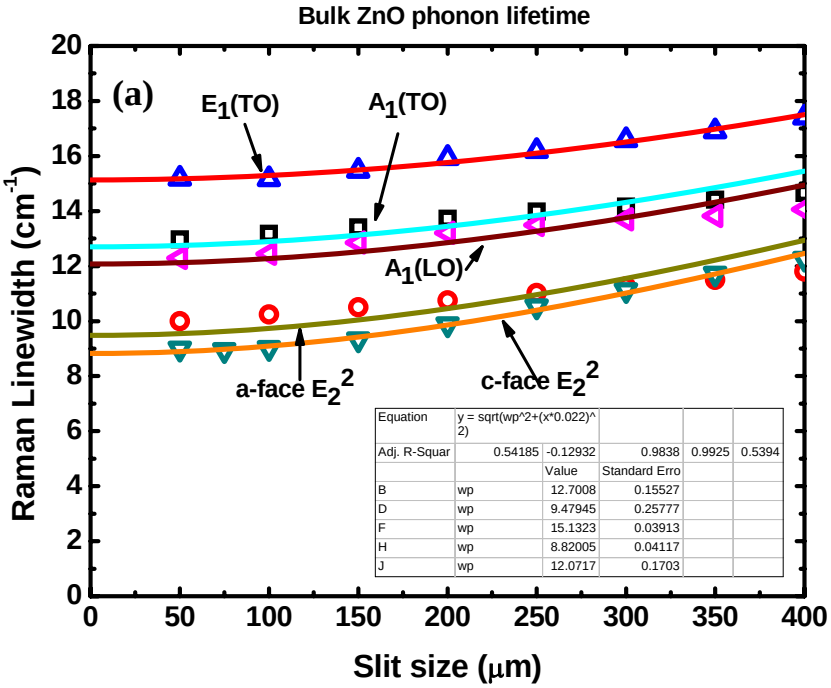

Equation	y = sqrt(wp^2+(x*0.022)^2)				
Adj. R-Squar	0.54185	-0.12932	0.9838	0.9925	0.5394
		Value	Standard Erro		
B	wp	12.7008	0.15527		
D	wp	9.47945	0.25777		
F	wp	15.1323	0.03913		
H	wp	8.82005	0.04117		
J	wp	12.0717	0.1703		

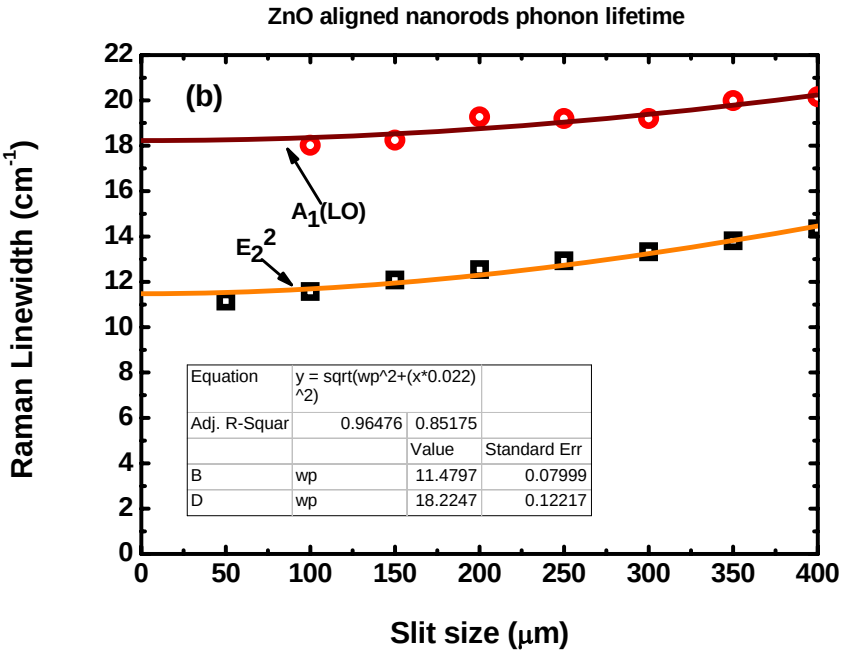

Equation	y = sqrt(wp^2+(x*0.022)^2)		
Adj. R-Squar	0.96476	0.85175	
		Value	Standard Err
B	wp	11.4797	0.07999
D	wp	18.2247	0.12217

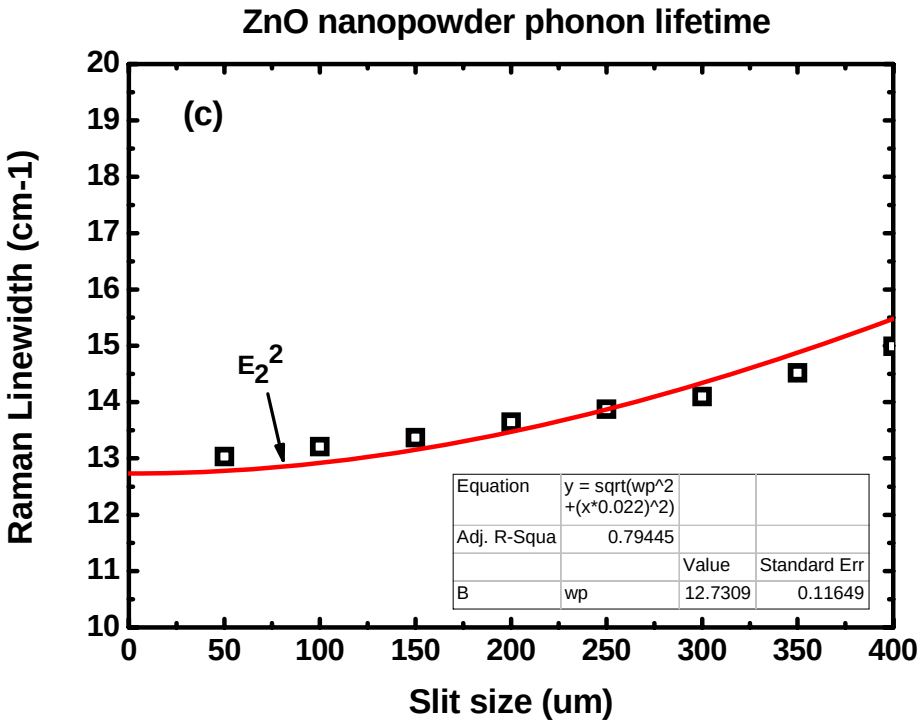

Figure 5.8 the linewidth of the Raman phonon modes as a function of the slit size. (a) undoped a-face and c-face bulk ZnO of $E_2^{(2)}$, A_1(TO), A_1(LO), and E_1(TO) modes; (b) aligned nanorods of $E_2^{(2)}$ and A_1(LO); (c) nanopowder of $E_2^{(2)}$ mode.

Phonon mode	a-face		c-face		aligned nanorods		nanopowder	
	Γ (cm-1)	τ (10^{-12}s)	Γ (cm-1)	τ (10^{-12}s)	Γ (cm-1)	τ (10^{-12}s)	Γ (cm-1)	τ (10^{-12}s)
$E_2^{(2)}$	9.47	0.56	8.82	0.61	11.48	0.462	12.73	0.416
A_1(TO)	12.70	0.417	--	--	--	--	--	--
E_1(TO)	15.13	0.35	--	--	--	--	--	--
A_1(LO)	--	--	12.07	0.44	18.22	0.29	--	--

Table 5.3 the phonon lifetime and the zero-slit Raman linewidth of the $E_2^{(2)}$, A_1(TO), A_1(LO), E_1(TO) modes of undoped a-face and c-face ZnO, aligned nanorods, and nanopowder.

5.4 Conclusion

The phonon lifetime of undoped bulk ZnO, aligned nanorods, and nanopowder have been carried out using room temperature Raman spectroscopy. We found out that the lifetime of $E_2^{(2)}$ phonon mode becomes shorter as the dimensionality decreases. The $E_2^{(2)}$ lifetime decreases from 0.61 ps of a-face ZnO wafer to 0.462 ps of aligned nanorods and then down to 0.416 ps of ZnO nanopowder. The lifetime shortening is claimed to mainly contributed form the anharmoinc decay since the PL spectrum shows aligned nanopowder and nanopowder have less visible defect emission as compared to undoped bulk ZnO. The $E_2^{(2)}$ mode exhibits a visibly asymmetric line shape that could be successfully explained in terms of resonant anharmonic interaction of the $E_2^{(2)}$ mode with a band of combined transverse and longitudinal acoustic modes, as the steep variation of the two-phonon DOS around the $E_2^{(2)}$ frequency leads to a distorted phonon line shape. The anharmonic decay of $E_2^{(2)}$ mode involves a continuum of TA+LA phonons, and the temperature dependence A1(LO) and E1(LO) modes can be accounted by a simple model in which the longitudinal phonon decays into a pair of TO and TA phonons whose frequencies correspond to a maxima of the phonon DOS.

CHAPTER 6

ZINC OXIDE NANOSTRUCTURE BASED DYE-SENSITIZED SOLAR CELLS

6.1 Introduction of Dye Sensitized Solar Cells

Dye-sensitized solar cells (DSSCs) are the most promising alternative electrochemical cells to conventional silicon based solar cells conceived in recent years. DSSCs is an optoelectronics device that converts light to electrical energy *via* charge separation in sensitizer dyes absorbed on a wide band gap semiconductor, which is different to conventional cells. A main difference between DSSCs and conventional solar cells, epitomized by silicon p-n junction solar cells is the relative importance of the interfacial processes. Conventional solar cells are primary the minority carrier transport devices. The efficiency is determined by the ability of photo-generated minority carrier to escape away from the internal electrical field before recombining with the majority carriers. Therefore, the efficiency of the conventional solar cell can be affected by the minority carrier lifetime, diffusion length, crystallinity and so on.

DSSC is a kind of excitonic solar cells belonging to the majority carrier devices of which electrons are found almost exclusively in one phase and holes in another. Charge carriers in these excitonic solar cells are generated at the interface between the electron-conducting and hole-conducting media via exciton dissociation. In traditional organic

photovoltaic (OPV), photo-generated excitons must diffuse to the interface before dissociating. However, the excited stated are created right at the interface of the DSSCs. All the charge carrier processes, photogeneration, separation, and recombination, occur primarily at the interface of the excitonic solar cells. Thus, the properties of the interface are of paramount importance in DSSCs as compared to bulk properties.

Energy conversion from dye-sensitized TiO_2 solar cell was first reported by Gratzel *et al* in 1988. [195] Even though the charge separation was able to generate at high efficiency, the energy conversion efficiency of this early DSSC was poor due to the low light absorption coefficient of the solar cell. Because the sensitizer dyes were absorbed onto a fairly flat surface of the TiO_2 semiconductor electrode, the light absorption by the monolayer of dye was limited. This problem was solved by replacing the TiO_2 electrode with nanoporous TiO_2 sintered electrodes. [196] Since the nanoporous electrode can provide large surface area per projected area, solar cell made from the dye-absorbed nanoporous film can dramatically increase its effective light harvesting. The highest current energy conversion of DSSC is over 11.3%, [197] and further increase of the efficiency is still under investigation.

TiO_2 DSSCs are typically consisted of a dye coated nanoporous TiO_2 electrode on transparent conductive oxide (TCO) glass substrate, electrolytes containing I^-/I_3^- redox couple filling into the porous of the electrode, and a platinum counter electrode placed on the top of the TiO_2. Figure 6.1 shows the diagram of the TiO_2 DSSC, the nanoporous electrode is usually synthesized by sintering TiO_2 nanoparticles with the diameter around tens of nanometer in order to achieve high surface area for dye absorbing and light

harvesting. The injected electrons in TiO_2 and acceptors, like ionized dye and I_3^- in the electrolyte are located within the scale of nanometer range. Such situation would likely results in short electron lifetime, decrease in the efficiency of the solar cells, whereas DSSCs have significantly long electron lifetime. This is one of the prominent features of the DSSCs. The relative energy levels of the sensitizing dye, the TiO_2, and the redox couple electrolyte determine the driving forces for the interfacial electron-transfer processes of photoinjection and recombination.

The photogenerated electron hole pairs are simultaneously and identical to the initial separation of the electrons from the holes across the DSSC interface. This is a distinguishable mechanism difference relative to conventional solar cell in whish electron hole pairs' generation and separation are two spatially and temporally distinct processes. Conventional solar cells have a gradient electric potential across the p-n junction to separate the photogenerated charge carriers. The built-in potential, Φ_{bi}, sets the upper limitation of the achievable photovoltage. In DSSC, electrons are generated in one phase (injected into the TiO_2) while the holes remain in the other; therefore, these two carriers are already separated across the interface of the phase boundary. The photovoltage of the DSSC is not determine by the built-in potential, but mainly affected by the phototinduced chemical potential $\Delta\mu$ difference across the interface.

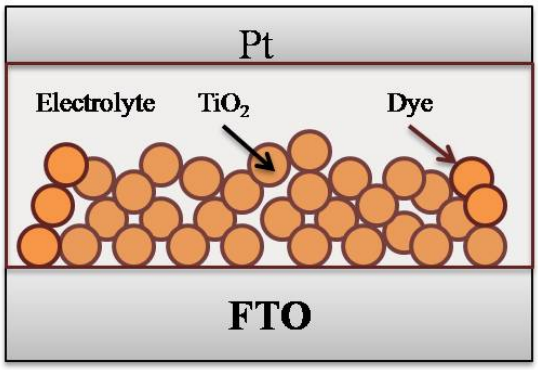

Figure 6.1 Structure of TiO_2 nanoparticle sintered DSSC.

6.2 Charge Carrier Processes Mechanisms in DSSC

The charge carrier processes include photogeneration, separation and recombination of carriers. The photo-conversion process starts at the interface when the absorbed dye, D, absorbs a photon and the resulting excited state, D*, injects an electron, e_{TiO2}, into the nanocrystalline TiO_2:

$$D^* \rightarrow D^+ + e_{TiO2} \qquad (1)$$

Normally, this reaction is extremely rapid, occurring in the subpicosecond regime. [198,199,200] The electrons and holes are generated on opposite side of the interface by the photoinjection process and never coexist in the same phase. The photoinjection reaction is followed by regeneration of the dye through the redox electrolyte, R:

$$R + D^+ \rightarrow R^+ + D \qquad (2)$$

this reaction in nanosecond range when R is an iodide ion in the 0.5M concentration electrolyte solution. [201] Diffusion of e_{TiO2} electrons through the nanocrystalline TiO_2 film to the FTO electrode and diffusion of the oxidized redox species R^+ through the

solution to the counter-electrode allow both charge carriers to transport to the external circuit.

The motion of ions in the pores of DSSCs plays an important role in charge separation process. When a photogenerated electron-hole pair is separated across the TiO_2-solution interface the electrostatic attraction between the opposite charges will oppose the separation. However, the interior DSSC contains no significant electric fields expect across the electrochemical double layers, and these are not adequate to screen an injected electron from the hole on the oxidized dye. [202,203] In a DSSC, mobile electrolyte ions can rapidly rearrange around the photogenerated charge pair and neutralize the Coulomb attraction force between them and thereby slowing the recombination rate. [204,205] This is one of the most critical functions of the electrolyte in the DSSC. If a solar cell is approximately electroneutral in the dark, such as DSSC, indicates that neutralizing the electrical field between the photogenerated electrons and holes is essential for efficient charge separation. Tennakone *et al.* confirmed this using CuI as the hole conductor in which the ionic mobility of the CuI may have helped neutralize the Coulomb attraction. [206] The design of high surface area solar cells in general, the bulk of the device is essentially field-free at equilibrium, then mobile electrolyte and nanoporosity are required to eliminate the photoinduced electric field. If the particle size is substantially larger than in the conventional dye cell or no mobile electrolyte, then an interfacial or bulk built-in electric field is required for efficient separation of the photogenerated charge carriers.

Carrier recombination is the energy-wasting process that needs to be eliminated as much as possible. There are three primary recombination pathways in DSSC; one involves recombination of e_{TiO2} with the oxidized dye before the dye before regenerated: [207]

$$e_{TiO2} + D^+ \rightarrow D \qquad (3)$$

The other two recombination processes are the interfacial recombination, one is the recombination of e_{TiO2} with the oxidized redox species and the other is the recombination of an electron in the SnO_2 substrate, e_{SnO2}, with the oxidized redox species,

$$e_{TiO2} + R^+ \rightarrow R \quad (4)$$

$$e_{SnO2} + R^+ \rightarrow R \quad (5)$$

The recombination of equation (5) is caused by the nanocrystalline TiO_2 film does not fully cover the SnO2 electrode, leaving void between particles when the substrate comes into contact with the redox solution. [208] Reaction (4) is favored by the high surface area of the TiO_2 rather than the SnO2 and reaction (5) is favored by the high concentration of electrons in the degenerately doped SnO_2 relative to TiO_2.

Figure 6.2 is the relative energy diagram of a DSSC. The conversion of phonon to current energy can be described by the following steps:

(1) Dye photosensitizers are attached on the TiO_2 surface to absorb incident photon injection.

(2) The dye sensitizers are excited from the ground state to the excited state. The excited electrons are injected in to the conduction band of the TiO_2 film, which results in the oxidation of the dye sensitizers.

(3) The injected electrons are transported through the surface or the bulk of interconnected TiO_2 nanoparticles with diffusion toward the FTO electrode.

(4) The oxidized dyes accept electrons from the redox mediator, I^- ion, regenerating the ground state of dye sensitizer, and the I^- ion is oxidized to the I_3^-ion.

(5) The oxided redox mediator diffuses to the counter-electrode and is relaxed to I^- over the Pt electrode.

The performance of DSSC is based on four enegy levels of the components: (i) the excited state /lowest unoccupied molecular orbital (LUMO level); (ii) the ground state/highest occupied molecules orbital (HOMO level) of the dye sensitizers; (iii) the Fermi level of the TiO_2 phototelectrode, which is located near the conduction band level since it is a n-type semiconductor; (iv) the redox potential of the redox mediator (I^-/I_3^-) in the electrolyte solution. The photocurrent generated from the DSSCs is mainly determined by the potential energy difference between the HOMO and LUMO of the dye sensitizer which is corresponds to the band gap of inorganic semiconductor. The smaller the HOMO-LUMO gas is, the higher the photocurrent that can be generated due to the utilization of the long wavelength regime of the solar spectrum. The potential energy difference between the LUMO level and the conduction band of the TiO_2 film is defined as ΔE_1, which indicates the energy of the LUMO level must be sufficiently more negative with respect to the conduction band of TiO_2 film in order to inject electrons effectively. The HOMO level of the dye must be sufficiently more positive than the redox potential in order to accept electrons (ΔE_2). The energy gaps, ΔE_1 and ΔE_2, must be greater than 200mV in order to provide enough driving force for the electron-transfer reactions to take

place. [209] As shown in Figure 6.2, the photovoltage is attributed to the energy band gap between the Fermi level of TiO_2 and the redox potential of the mediator in the electrolyte. The conduction band level of TiO_2 and the redox potential are -0.5 versus saturated calomel electrode (SCE) and 0.4V versus SCE, respectively. Therefore, the maximum photovoltage that can be generated fir TiO_2 DSSCs is approximately 0.9V.

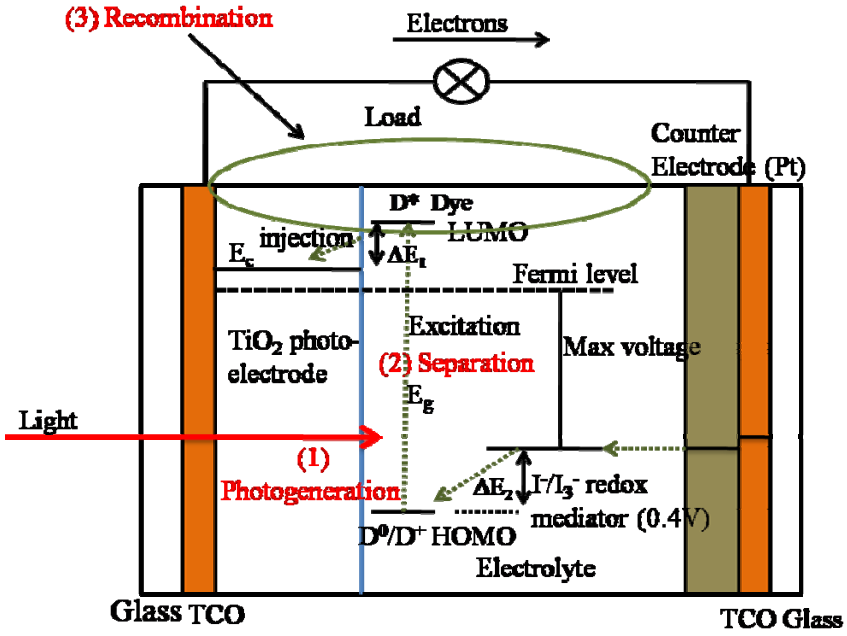

Figure 6.2 Energy diagram and operating principle of DSSCs. [209]

For an ideal energy conversion, all the incoming photons are ideally converted to electrons without losing the energy of photons. This phenomenon can be described by the incident photon-to-current conversion efficiency (IPCE). IPCE is determined by the light-harvesting efficiency (LHE), charge injection efficiency (CIE), and charge collection efficiency (CCE). IPCE can be obtained by the following equation:

$$IPCE = \frac{1240(nm \bullet eV) \times J_{sc}(\frac{\mu A}{cm^2})}{\lambda(nm) \times \Phi(\frac{\mu W}{cm^2})}$$

where Jsc is the short circuit photocurrent density for monochromatic irradiation, λ is the wavelength, and Φ is the monochromatic light intensity. IPCE can also be given by

$$IPCE = LHE \times \varphi_{inj} \times \eta_c$$

$$LHE(\lambda) = 1 - 10^{-\alpha d}, \alpha = \sigma \times c$$

φ_{inj} is the quantum yield of electron injection, and η_c is the efficiency of collecting injected electrons at the electrode. LHE is defined as the ratio of the amount of absorbed photons to that of incoming photons. Lambert Beer's law is applied to describe the light absorption yield for the reciprocal absorption length, α=σ×c, σ and c are the optical absorption cross section of the dye sensitizer and its concentration in the mesoporous film. [210] σ can be derived from the decadic extinction coefficient ε of the sensitizer using σ= ε×1000[cm^2/mole]. For the LHE equation above, it is a function of the thickness of the semiconductor film (*d*) and the optical absorption cross section. LHE can be improved by the absorption coefficient of dye, the density of absorbed dye, and the thickness of dye absorbed nanoporous film. From the energy diagram of Figure 6.2, the CIE can be determined as potential difference between the conduction band edge of the wide band gap semiconductor (TiO_2, ZnO etc.) and LUMO level of the adsorbed dye, and acceptor density of the TiO_2/ZnO; (3) spatial separation between the surface of the TiO_2/ZnO and the dye. CCE is mainly controlled by the electron diffusion length. Diffusion length can

be expressed by $L= (D\tau)^{(1/2)}$, where D is the electron diffusion coefficient and τ is the electron lifetime inTiO_2/ZnO.

The electron-transfer rate from the dye sensitizer depends on the configuration of the adsorbed dye on the semiconductor surface and the energy gap between the LUMO level of the dye and the conduction band edge of the semiconductor. In a DSSC, the dye molecules are strongly absorbed onto the semiconductor surface with carboxyl groups as anchors resulting in a very large electronic coupling potential between the π^*-orbital of the excited state of the dye and the conduction band of the semiconductor, which consists of the unoccupied 3d-orbital of Ti^{4+} for TiO_2 and 4s-orbital of Zn^{2+} for ZnO. [211] Figure 6.3 is the schematic diagram of electron-transfer processes in DSSC. Theoretically, in order to make the DSSC to work properly the electron injection rate must be higher the rate of relaxation rate of the dye and the carrier recombination rate. Time-resolved laser spectroscopy observed that electron injection from N3 dye into the TiO_2 film occurs on the order of femtosecond. [196,212] This ultrafast electron injection rate ensures the high energy conversion of DSSC. The carrier recombination process between injected electron and oxidized dyes must be orders of magnitude slower than the process of electron injection and electron transfer from the redox ion (I^-) into oxidized dye to achieve effective charge separation. It was reported that the charge recombination of the electron in the conduction band and the cations of N3 dye occurs on the order of microsecond to millisecond. [213,214,215,216] The much slower recombination rate leads to an effective charge separation and high cell efficiency.

Excited dye relaxation is attributed by gaining electrons from I⁻ ions into the oxidized dye (cation), is one of the most important processes needed to achieve effective charge separation. The electron-transfer rate from I⁻ into the oxidized (N3) was reported to be 100 nsec. [217] Recombination of injected electrons in the semiconductor with the triiodide ion (I_3^-) at the interface is related to the dark current which is one of the most unwanted configurations. This recombination comes from two pathways (1) from the electrons of the SnO_2 electrode surface recombine with the triiodide since the nanocrystalline TiO_2 does not completely cover the TCO surface; (2) the other pathway is the most predominant recombination of which the electrons in the conduction band of TiO_2 recombine with the triiodide (I_3^-) cation. The second pathway is most predominant because of the large surface area of TiO_2 as compare with SnO_2. This recombination results to the loss of photovoltaic performance in DSSCs, which is similar to the forward bias injection of holes and electron in p-n junctions. The open circuit voltage in the DSSCs can be determined by the injection current, I_{inj}, as reprented by following equation,

$$V_{oc} = \frac{kT}{q}\ln\left(\frac{I_{inj}}{I_0}+1\right)$$

where k is the Boltzmann constant, q is the electron charge, T is the absolute temperature, and I_o is the dark current. The injection current I_{inj} is represented as

$$I_{inj} = q \times \eta \times \Phi_0$$

η is the quantum yield for photogenerated electrons, Φ_o is the incident photon flux.

Solar energy-to-electricity conversion efficiency (η) under white light irradiation can be found from,

$$\eta = \frac{P_{out}}{P_{in}} = \frac{J_{sc} \times V_{oc} \times FF}{I_0 \times 100}$$

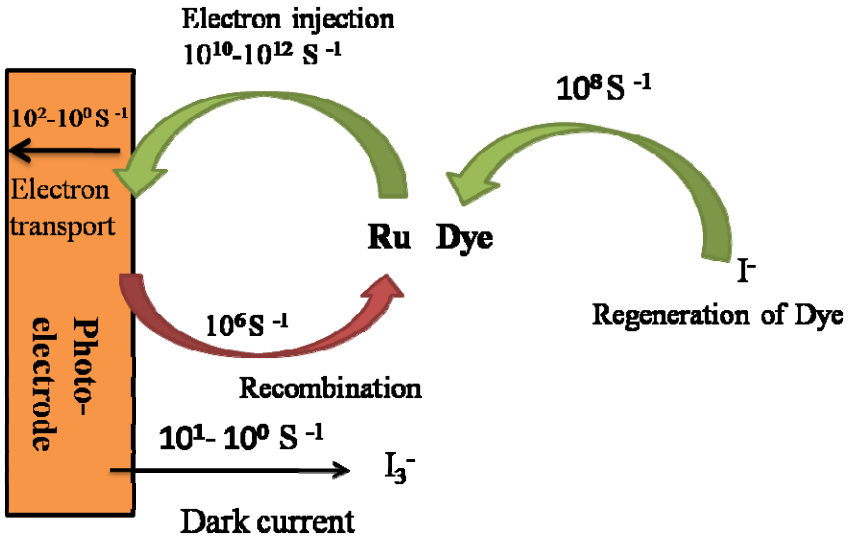

Figure 6.3 Schematic diagram of electron-transfer processes in DSSC.

6.3 Distributed Resistor Network Model of DSSC

Distributed resistor model is a simple concept to realize the spatial dependence of current flow across a high-surface area interface between the TiO_2 and the electrolyte solution containing redox couples. [209,218] In this model, the ion motions through the nanoporous film are neglected and focus on the spatial distribution of current flow across the large-surface area. While a negative bias is applied to the substrate electrode in the dark, some electrons will be repelled and injected into the semiconductor (TiO_2/ZnO) which is in contact with the substrate. The electrons can transport along two possible pathways: (1) hopping into the other adjacent TiO_2 particles (2) conduct across the TiO_2-solution interface, reducing the redox species R^+ which is as same as reaction (4). The

distributed resistor is hold valid for the potential distribution under steady-state conditions. The first consideration is the interparticle resistance, R_{TiO2}, and the second is the interfacial charge transfer resistance, R_{ct}. Electrons transfer into the second TiO_2 particle (second node of the circuit) have the same choice of two pathways and so forth through the entire structure until reach the last particle. As the electrons are transfered to the last particle, the only choice is to proceed into the electrolyte solution. While the electrons are transferred into solution, they will encounter the electrolyte resistance, R_s, which is considered negligible compared to the other two resistances in this model, but might be a factor for solid-state electrolyte.

Figure 6.5 is the calculated potential distribution across a DSSC modeled by the resistor network of Figure 6.4. [209] Figure 6.5 shows a solution for a 100 resistors network and the parameters are setting as V_{app}=1.0V, R_s=0.001Ω, and $R_{TiO2+}R_{ct}=10^4$ Ω. The potential applied to the substrate electrode (E_{sub}) can extend uniformly throughout the semiconductor only when $R_{ct}/R_{TiO2}\rightarrow\infty$. Otherwise, the potential of the semiconductor film will be a function of distance from the substrate and vary between E_{sub} and the solution redox potential, E_{redox}. Among the three resistances, R_s is only considered to be approximately constant in a standard DSSC. $R_{TiO2/ZnO}$ is considerably variable depending on the light illumination intensity, applied potential, and concentration of the ions.

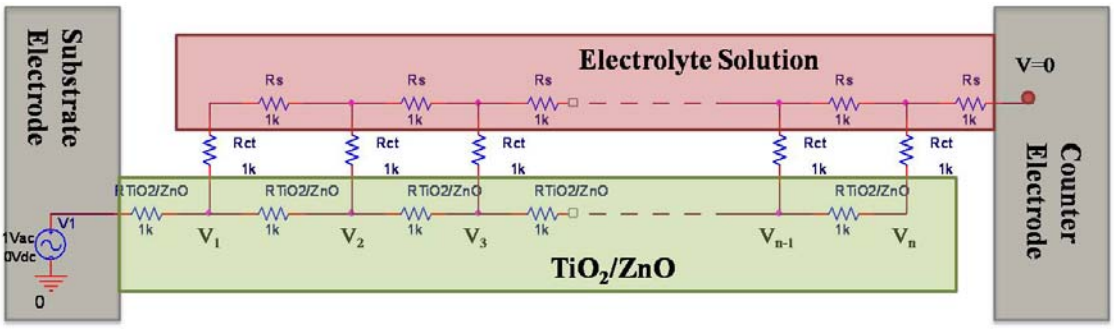

Figure 6.4 A distributed resistor model network of DSSC under steady-state condition. $R_{TiO2/ZnO}$ is the interparticle resistance, and the interfacial charge transfer resistance, R_{ct}. The voltage is calculated for each node of the TiO_2 network, labeled V_1 through V_n. This model is a pure electric model which does not take electrolyte mobility into account. Therefore, potentials at the nodes are electrical potentials; however, in a DSSC all internal potential are electrochemical in nature. [209]

Under illumination of DSSC, both the electrons concentration and electron diffusion coefficient increase by orders of magnitude over a cell at equilibrium [219], which indicates the resistance of the semiconductor decrease by several orders of magnitude. R_{ct} also decreases under illumination and with applied negative potential, but much less than R_{TiO2}. [210,220] It is valid to assume that $E_{sub} \approx E_{TiO2}$ only when the condition of $R_{ct} >> R_{TiO2}$ is hold, which may be approached in thin cells under conditions of high illumination intensity with a kinetically slow redox couple like I^-/I_2. The current (electrons) always takes the smallest resistance path through the entire cell. If R_{TiO2} is the dominant resistance, like under dark current condition, much of the TiO_2 will remain near solution potential and most current will flow through solution rather than TiO_2. If R_{ct} is the dominant resistance the TiO_2 film will be near the substrate potential and the current

will flow approximately uniformly across the TiO_2-solution interface in DSSC. This condition may be valid as illuminated DSSC using the I^-/I_2 redox couple. For the condition of $R_{ct} \approx R_{TiO2}$, only the dyes which are closed to the substrate will contribute the photocurrent because electrons injected far away will recombine before they reach the substrate. The difference in effective current pathways under different conditions, like light versus dark, solid state versus liquid electrolyte etc, are an essential characteristic to be considered for DSSCs design. One dimensional spatial model is appropriate for conventional solar cell since only one current pathway need to be taken into account.

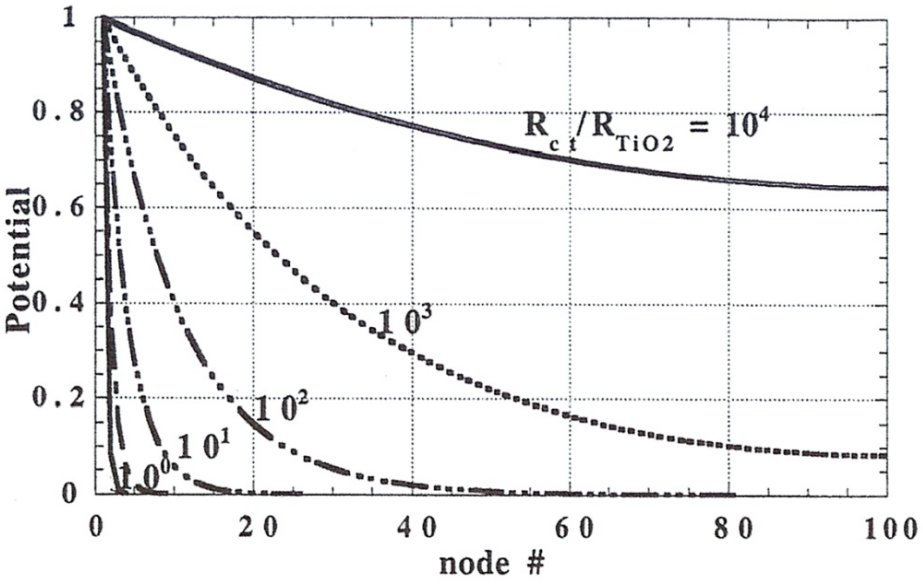

Figure 6.5 The calculated potential distribution across a DSSC modeled by the resistor networking of Fig. 6.4. The node number corresponds to the distance through the cell. [209]

6.4 Theoretical Analysis of DSSC

The electrochemical potential energy E is the sum of the electrical and chemical potential energies, E=U+μ, has been well-established by Gibbs. [221] The spatial gradient of the potential energy is defined as force, ∇E is the fundamental force that drives the charge carrier fluxes through the solar cell and the other electrical components. The general kinetic energy expression for one-dimensional current density of electrons $J_n(x)$ is

$$J_n(x) = n(x)\mu_n \nabla U(x) + kT\mu_n \nabla n(x) \qquad (6)$$

where n(x)is the electron concentration, μ_n is the electron mobility and k and T are Boltzmann constant and the absolute temperature. This current density formula holds both at equilibrium and away from it, both in the dark and in the light measurements. The nonequilibrium quasi Fermie level of electron in the semiconductor is

$$E_{Fn}(x) = E_{cb}(x) + kT \ln[\frac{n(x)}{N_c}] \qquad (7)$$

where $E_{cb}(x)$ is the electrical potential energy of the conduction band edge, $E_{cb}(x)=U(x)+$constant, and N_c is the density of electronic states at the bottom of the conduction band. Substituting equation (7) into equation (6), and then generates a simplest expression for the electron current,

$$J_n(x) = n(x)\mu_n \nabla E_{Fn}(x) \qquad (8)$$

The above electron current density equation is proportionally to the electrochemical force (∇E_{Fn}) by a factor of n(x) ×μ_n. This reveals that under any photo-process that generates a nonzero value of ∇E_{Fn} will result in a photovoltaic effect. This can be valid in both

conventional p-n junction solar cells and excitonic solar cells. In order to shows the mechanisms of excitonic solar cells (DSSCs), it is essentially to consider the quasi-thermodynamic component of ∇U and $\nabla\mu$, which are the factors of ∇E_{Fn}. The electron density in equation (6) is consists of two independent driving forces ∇U and $\nabla\mu$.. J_n due to the electrical potential energy gradient is,

$$J_n(x) = n(x)\mu_n \nabla U(x)$$

, and Jn due to the chemical potential energy gradient is,

$$J_n = \frac{n(x)\mu_n}{n(x)} \nabla n(x) = n(x)\mu_n \nabla \mu(x)$$

The identity $\nabla\mu(x) = \frac{kT}{n(x)}\nabla n(x)$ can be obtained from the equilibrium thermodynamic expression $\mu = kT\ln(n) + \mu^0$. [222] Therefore, equation (8) can be rewritten in the form of

$$J_n(x) = n(x)\mu_n\{\nabla U + \nabla\mu(x)\} \qquad (9)$$

, n(x) and μ_n influence the magnitude of the electron flux, and $\nabla U + \nabla\mu(x)$ controls its direction. [223] In conventional p-n junction solar cell, ∇U is the predominant factor that results from two primarily factors: (1) the photogeneration of carriers throughout the bulk and (2) the high mobilities that allow them to quickly balance their special distributions regardless of their point of origin. Therefore, minimize the influence of $\nabla\mu(x)$. In DSSC, all the photogenerated carriers are created in a very narrow region near the interface, leading to a photoinduced carrier concentration gradient, which is related to $\nabla\mu(x)$, that is much higher and qualitatively distinct from conventional solar cell. This phenomena

coupled with the spatial separation of two types of carriers across the interface upon photogeneration, constitute a powerful photovoltaic driving force.

The maximum photovoltage for any type of solar cells at a static light intensity can be obtained by deriving equation (8). ∇E_{Fp} *and* ∇E_{Fn} are the driving force of electron and hole fluxes, respectively. The maximum photovoltage in an ideal PV cell is given by the maximum splitting between the quasi Fermi levels anywhere in the cell at open circuit, since an applied potential difference greater than this will cause the photocurrent to reverse its direction. [224]

$$qV_{oc,\max}(I) = (E_{Fn} - E_{Fp})_{\max}$$

The photovoltage in a real solar cell $V_{oc}(I)$ is usually less than $V_{oc,max}(I)$ because of recombination processes, mass limitations, etc. The photovoltage of a solar cell is a function of both the built-in electrical and the photoinduced chemical potential energy difference across the cell. In DSSC, the charge carrier pairs are already separated across the interface upon photogeneration, creating a large $\nabla\mu$ which tends to separate them further. An internal electric field is not required for charge separation and thus the built-in electric potential does not set the upper limit to V_{oc}.

6.5 Zinc Oxide Based Dye-Sensitized Solar Cell

Recently, a great attention has been paid to dye-sensitized solar cells (DSSCs) due to its low fabrication cost. In a typical DSSC, photogeneration of charge carrier occurs under the light illumination, followed by a rapid charge separation. The electrons are injected into the porous TiO_2 nanocrystalline film while the separated holes are

transported to the counter-electrode by means of redox process. Previously, DSSCs have been fabricated using semiconducting TiO_2 nanoparticles. [225,226,227] However, even though the conventional TiO_2 DSSCs can reach the power conversion efficiency higher than 11.3%, the performance of the nanoparticle-based DSSCs greatly relies on trap-limited diffusion for electron transport, which can result in a slow transport mechanism (with electron escape times of 1-10 ms for an approximately 10 μm thick TiO_2 films) and limitation on the device efficiency. [228] Theoretically, a substantial increase of DSC performance can be achieved by one of the three fix.

In order to improve the efficiency and stability of the photoelectrochemical cell, the following approaches have been attempted; (i) replacing the volatile liquid electrolyte with nanovolatile. [229,230] or solid state electrolyte, (ii) attempting to improve the light absorption efficiency and quantum yield toward red wavelength, [231] (iii) adopting a different nanocrystalline material in order to speed up the electron transport and to prevent the recombination to occur. [232,233]

Zinc oxide (ZnO) is a wide band gap semiconducting (3.37 eV) material with a similar band-gap and electron affinity to those of TiO_2, and has been considered as an alternative material in DSSC application. Table 6.1 is the data table of properties of ZnO and TiO_2.It is also expected that ZnO will serve a better optical window than TiO_2 due to its larger band gap. One-dimensional (1-D) ZnO nanostructure also provides higher surface-to-volume ratio, which allows much more dye molecules to be adsorbed. In addition, electron conduction can occur through the direct electron path formed *via* a ZnO nanowire, instead of electron hopping between TiO_2 nanoparticles, thus contributing a

faster electron transport than TiO_2. [234] In addition, it is not easy to synthesize 1-D TiO_2 nanostructure while the growth of 1-D ZnO is relatively controllable.

	ZnO	TiO_2	Unit
Crystal Structure	Wurtzite	Anatase	
Lattice constant, a	3.25	3.78	Å
Lattice constant, c	5.12	9.51	Å
Density	5.6	3.79	gcm^{-3}
Static dielectric constant ε_s	7.9	31	
Optical dielectric constant ε_∞	3.7	6.25	
Optical band-gap, E_{obg}	3.2	3.2	eV
Flat band potential, E_{fb}	-0.5	-0.5	V vs.SCE
Effective electron mass	0.24-0.3m_e	1.0 m_e	m_e=9.11×10-^{31}kg
Effective hole mass	0.45-0.6m_e	0.8 m_e	m_e=9.11×10-^{31}kg
Electron mobility, μ_e	200	30	$cm^2V^{-1}s^{-1}$
Point zero charge	8-9	5.5-6.5	pH

Table 6.1 The optical and electrical properties of ZnO and TiO_2. [71]

6.6 Experiment

A glass substrate coated with transparent conducting oxide (TCO) such as indium tin oxide (ITO) or fluorine-doped tin oxide (FTO) has been typically employed for DSSC fabrication. Due to the low melting temperature of a glass, low-temperature process is

required to grow ZnO nanostructures on ITO-coated glass (hereafter to be referred to as ITO/glass). For this reason, thermal CVD which requires high-temperature synthesis has not been considered as a proper technique for ZnO growth on ITO/glass. Instead, 1-D ZnO have been synthesized on ITO/glass using a metalorganic chemical vapor deposition (MOCVD) [235] and solution-based growth [226,236] since these techniques allow low temperature processing and easy morphological control. However, the properties of ZnO can be changed by different growth methods. Thermal CVD synthesis can achieve high crystallinity, various morphologies, and less chemical contamination when non-catalyst growth process is empolyed. In spite of the significance, relatively little work has been performed on ZnO nanowire-based DSSC research. [237] In our laboratory, we have successfully synthesized ZnO nanostructures at low temperatures (~500 °C), which enables DSSC application that necessitates low temperature processing. This is made possible by using a novel double-source-double-tube (DSDT) thermal CVD system which is a modified form of conventional thermal CVD system. A ZnO nanocrystalline thin film had also been prepared in order to show and compare the difference between planer electrode and one dimensional naonstructured electrode.

The ZnO nanostructures were prepared *via* catalyst-assisted DSDT thermal CVD with a liquid nickel catalyst. Prior to ZnO nanostructure growth, the ITO/glass substrate was sputter coated with an ultra thin (20-30nm) ZnO layer which can originate more preferential and uniform nucleation sites for ZnO growth. [238] These ZnO layers were prepared using RF magnetron sputter at 300W under the growth pressure of 8 Torr for 15 minutes. Argon (Ar) and oxygen (O_2) were serving as the reaction species during

deposition at the flow rate of 33 sccm and 11sccm. The thickness of the ZnO film needs to be optimized for DSSCs since it can greatly eliminate the charge recombination of the photo-generated free electrons and the positive ions from the ITO substrate, which will decrease the performance of the DSSCs. It is important to optimize the thickness of the ZnO layer since there is a trade-off between the open circuit voltage (V_{oc}) and short circuit current (I_{sc}) of the DSSC depending on the thickness of the ZnO layer. The V_{oc} can increase with increasing the thickness while the I_{sc} will decrease as the layer thickness increases. All the as-sputtered samples were cleaned and immersed into the Zn powder diluted methanol ultrasonic bath for 30 min in order to achieve a more uniform ZnO growth and easier first stage nucleation sites generation.

The ZnO nanostructures were grown for 45 minutes under 25 Torr of a mixture of Ar and O_2 with a flow rate of 125 sccm and 20 sccm, respectively. The ITO/glass substrates were placed on top of a larger alumina boat with Zn powder underneath the substrate. An additional smaller alumina boat that contained very little amount of Zn powder was initially inserted into the end of the smaller quartz tube before loading the larger alumina boat. The whole tube was inserted into the center zone of the quartz tube furnace. The temperature was gently ramped to 500°C with the elevating rate of 5°C/min. Ar was firstly fed into the quartz tube as the furnace temperature reach above the melting point of the Zn powder. Oxygen (O_2) was introduced to the tube 1 minute after the Ar was started to be fed. It was observed that 1-D ZnO with different morphologies can be synthesized if the growth parameters such as gas flow rate, pressure, and growth time changes.

The ZnO morphology was studied using field emission scanning electron microscope (JOEL JSM-7000) and the crystal structures were characterized by x-ray diffraction (XRD) using a Rigaku Miniflez powder X-ray diffractometer. UV-Vis spectrophotometry was used to collect the absorption spectra of the ZnO with/without dye coating. Room temperature photoluminescence (PL) and micro-Raman spectra were performed with a Jobin-Yvon spectrometer using 325 nm and 441.6 nm lines from He-Cd laser, respectively.

6.7 Result and Discussion

Figure 6.6 shows the schematics of the configuration of the 1-D ZnO-based DSSC device. A portion of the ZnO and the ITO surface was covered with epoxy in order to prevent the short circuiting and the charge recombination. The as-grown samples were dipped in a 0.2 mM ethanolic solution of cis-bis(isothiocyanato) (2-2'-bipyridyl-4, 4' dicarboxylato)-ruthenium(II) bis-tetrabutylammonium dye (N719) for 1 hour. As a counter-electrode, an ITO/glass substrate with a sputtered 50 nm thick Pt layer was used. The electrolyte was a mixture of 0.5 M tetrabutylammonium iodide, 0.05 M I_2, and 0.5 M 4-tertbutylpyridine in acetonitrile. Electrolyte was fed into the gap between the electrodes by a capillary force. A 60 μm thick anodized alumina oxide (AAO) was served as the spacer between the two electrodes. Current-voltage (I-V) characteristics of the devices were studied using Keithley 6487 picoammeter with an embedded voltage source with a sweeping rate of 0.1V/s. Xenon lamp (150W) was used for I-V measurement under illumination. The power density of the light was adjusted to approximately 100 mW/cm^2.

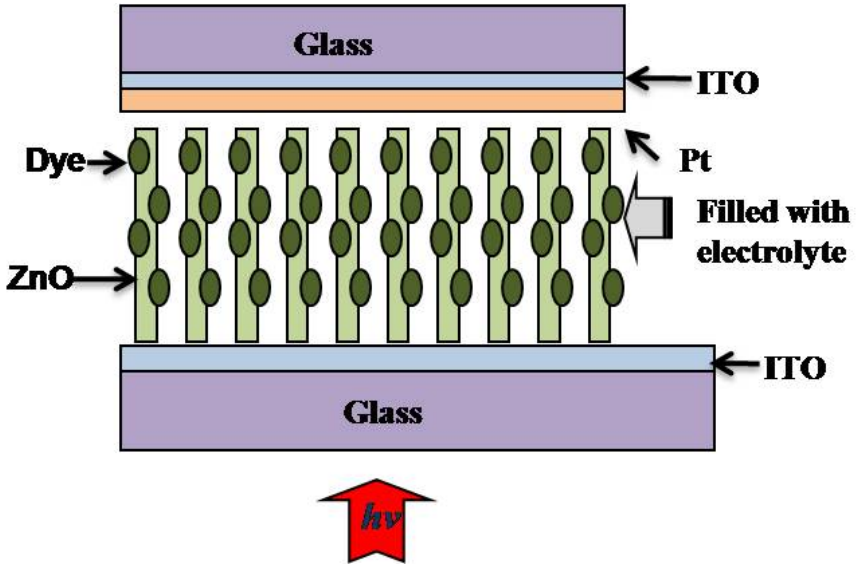

Figure 6.6 Schematics of the DSSC device based on 1-D ZnO nanostructures.

The X-ray diffraction (XRD) pattern shown in Figure 6.7 confirms that the ZnO nanorods are quasi-aligned predominantly with (002) orientation. A fairly uniform and well-aligned ZnO nanorods array SEM image is shown in figure 6.8(a). According to figure 5.8(b), the average size of the nanorods is approximately 70-100nm in diameter with the length of tens of micrometers. From 6.8 (b), the hexagonal shape of the ZnO nanorods can be clearly identified from the top view of the substrate which means those ZnO nanorods are hexagonal wurtzite crystal structure. It was reported that quasi-aligned nanorod provide better light-harvesting capability than well-aligned one. [239]

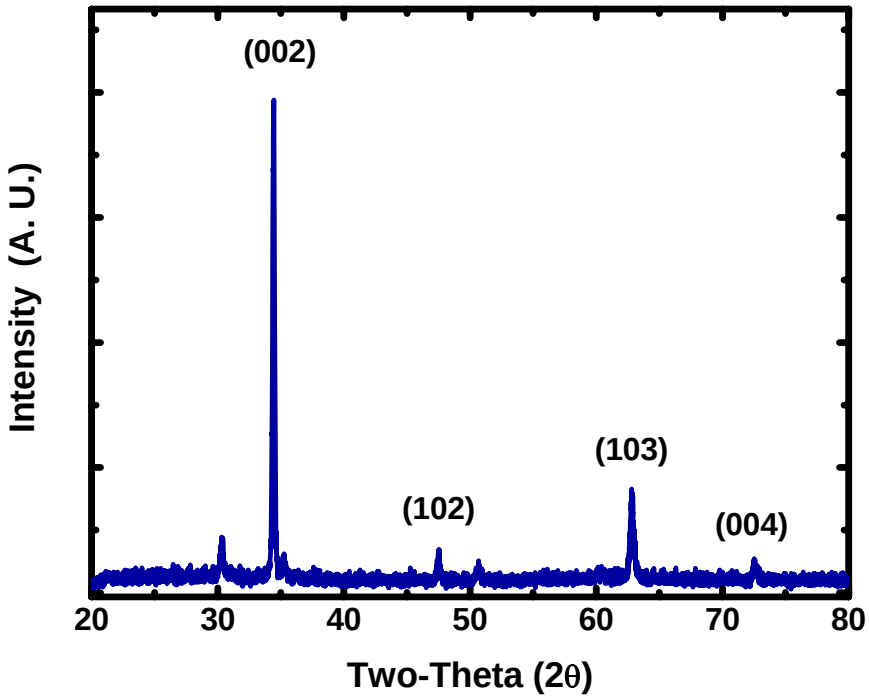

Figure 6.7 X-ray diffraction pattern of the ZnO nanostructure.

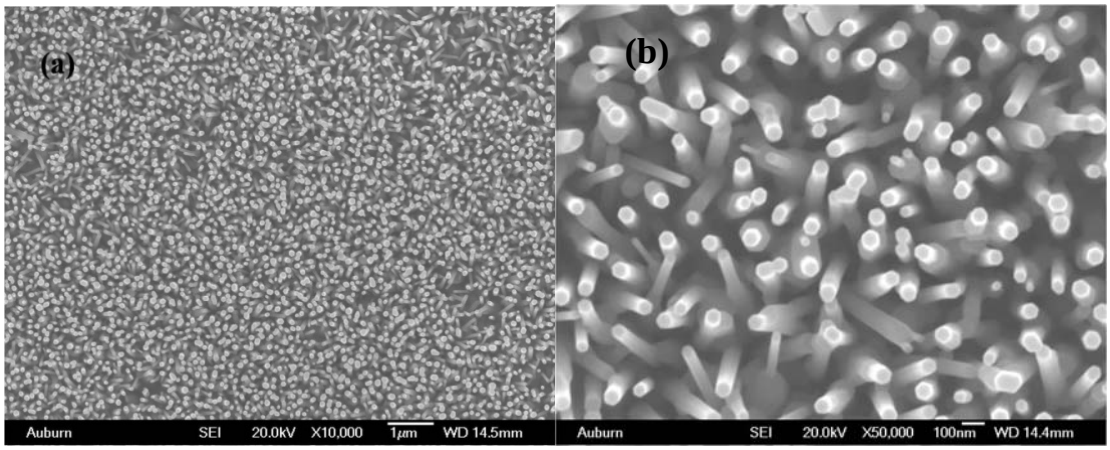

Figure 6.8 SEM microgroaph of ZnO nanorods (a) low magnification (b) high magnification.

This ZnO nanorods sample was prepared *via* catalyst-assisted thermal CVD method by applying liquid nickel catalyst. The ZnO nanorod was grown under the condition of 25Torr for 45 min with the mixture of Ar and O_2 for 125 sccm and 20sccm, respectively. The as-sputtered ZnO nanocrystalline thin film shown in Figure 6.9(a) is about 700nm thick. The ZnO crystal size varies from 10nm to 100nm due to the aggregation of the ZnO islands and the strain/stress between each crystal sites. The ZnO islands can be clearly found in the tilted view of higher magnification SEM image in Figure 6.9 (c). In Figure 6.9(b), the XRD of the ZnO thin film shows the film is preferential oriented in (002) direction with a small peak at (103) direction. The gray curve represents the XRD of the ITO coated glass, which shows the background peaks of the ZnO nanocrystaline thin film are originated from the ITO glass substrate.

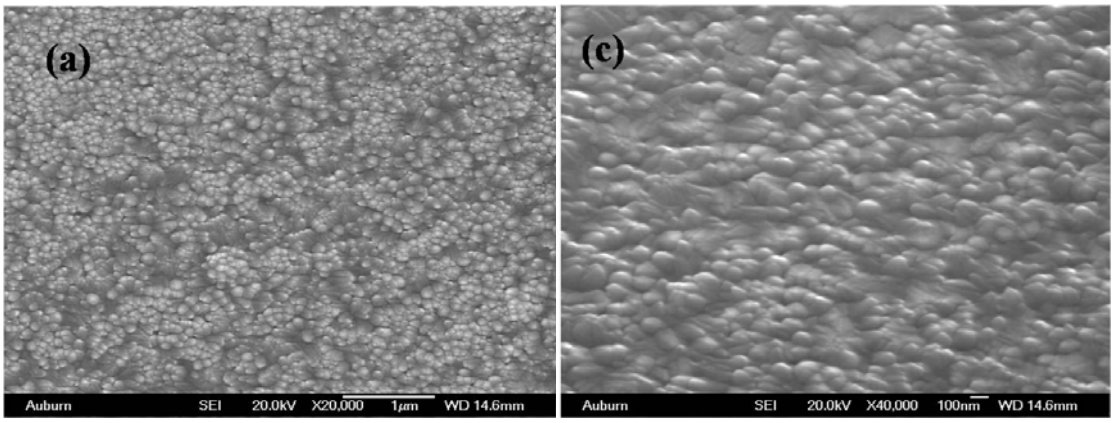

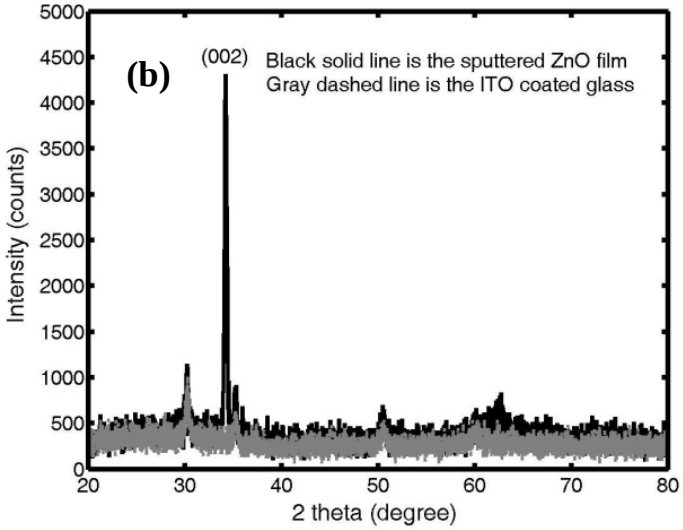

Figure 6.9 (a) low resolution SEM image of as-sputtered ZnO thin film; (b) black curve represents the XRD of the ZnO thin film, the gray curve represents the pure ITO coated glass; (c) high resolution SEM image of the ZnO thin film with the tilting angle of 30º.

The photoluminescence spectrum of the quasi-aligned ZnO nanorods is shown in Figure 6.10 (a). An ultraviolet near-band-edge (NBE) emission at 380 nm and a blue-green emission centered at around 500 nm are observed. The blue-green emission is considered to be due to the deep level defect produced during the growth. The green emission is thought to be produced by photogenerated holes recombining with the electrons of singly occupied oxygen vacancies. [240] Oxygen vacancies and zinc interstitial related defects are considered as the most probable culprit for generation of green/blue emission in our samples grown under oxygen deficient environment. [241] The Raman spectrum (Figure 6.10 (b)) exhibits peaks at 435 cm^{-1}, and 574 cm^{-1}, which correspond to E_2 and $A_1(LO)/E_1(LO)$ modes of a wurtzite ZnO, respectively. Note that ITO also contributes Raman peaks at 585, 1110, and 1610cm^{-1}. [242] The Raman

scattering spectrum of ZnO nanorods coated ITO glass substrate in Figure 6.10 (b) is compared with the Raman spectrum of a bare ITO coated glass substrate. The Raman scattering of ITO thin film substrate should have the peaks at 585, 1110, and 1610cm^{-1}. [226] Curve (b) in Figure 6.10 (b) shows a broad peak at ~560cm^{-1} measuring from a bare clean ITO glass substrate which indicated that the broad peak should be generated from the glass substrate instead of the ITO film. Con-focal Raman was performed to confirm the ITO is too thin to be measured as compare to the glass substrate. The ITO film Raman scattering peaks have not detected due to the film of ITO is much thinner than the glass substrate. In Figure 6.10 (b), the peak at ~570cm^{-1} in curve (a) is a mixing peak of ZnO A_1(LO) and the ITO coated glass substrate since the peak have a 10cm^{-1} red shift as compare the curve (b). From the Raman spectrum, the ZnO nanostructure is confirmed to have wurtzite structure with a good crystalllinity.

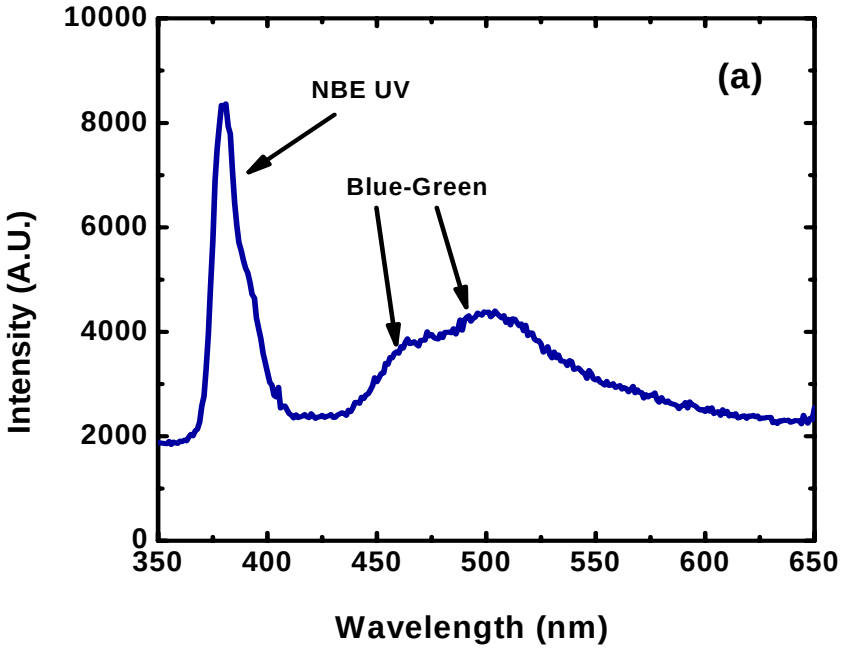
10000
8000
6000
4000
2000
0
Intensity (A.U.)
NBE UV
Blue-Green
(a)
350
400
450
500
550
600
650
Wavelength (nm)

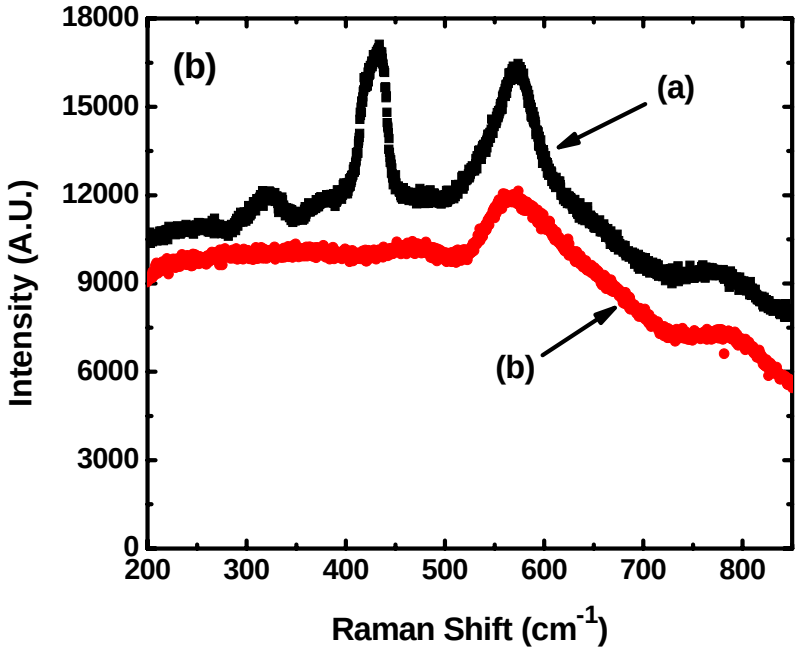
18000
15000
12000
9000
6000
3000
0
Intensity (A.U.)
(b)
(a)
(b)
200
300
400
500
600
700
800
Raman Shift (cm-1)

Figure 6.10 (a) Photoluminescence and (b) Raman spectrum of the ZnO nanostructure.

In order to confirm whether or not the dye molecules are successfully adsorbed onto the surface of the ZnO nanorods, transmission spectroscopy was performed before and after dye adsorption. Figure 6.11 show the absorption spectra of ITO/glass and the ZnO/ITO/glass electrode before and after immersing in the dye solution for 1 hour. Note that the peak around 380 nm corresponds to the absorption of the ZnO nanostructure. After application of dye, an additional absorption peak at ~535nm showed up, and this peak corresponds to the absorption peak of N719 dye. Therefore, it can be confirmed that the N719 dye was attached onto the surface of the ZnO nanostructure.

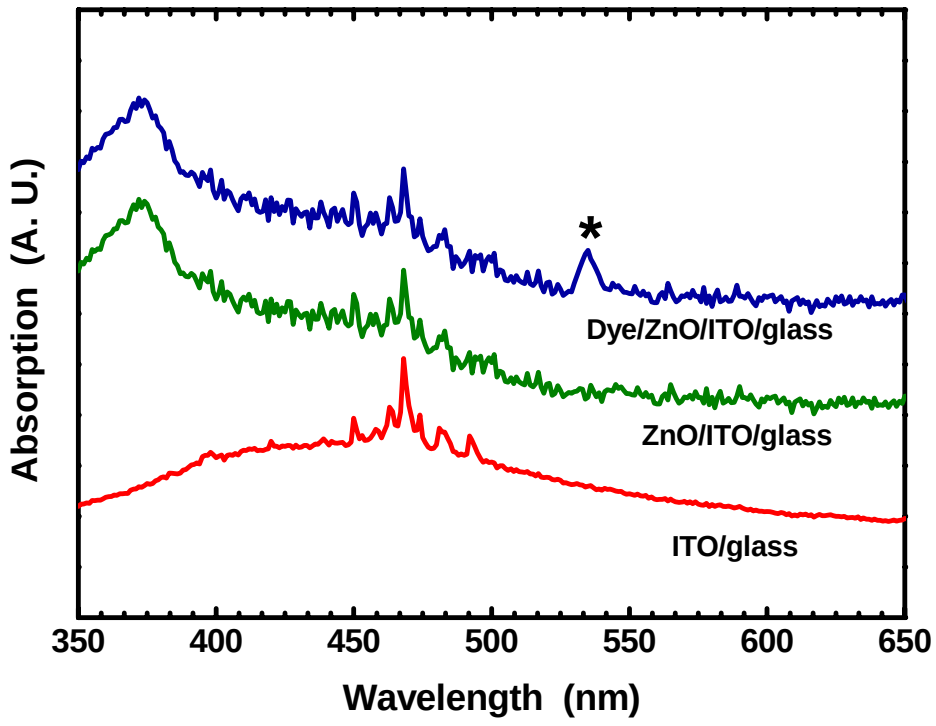

Figure 6.11 Absorption spectra of dye/ZnO/ITO/glass, ZnO/ITO/glass and ITO/glass (Note that ITO/glass is coated with thin sputtered ZnO layer.

The photo current-voltage characteristics for a ZnO based DSSCs are measured by the broadband xenon light source of 100mW/cm^2. The dark and photo current-voltage (I-V) characteristics for the ZnO nanorods based DSSCs are shown in Figure 6.12(a). From the I-V characteristics (Figure 6.12(b)), the open-circuit voltage (V_{oc}), short-circuit current density (J_{sc}), fill factor (FF), and the overall power conversion efficiency (η) are determined and the values are 0.82 V, 1.2 mA/cm^2, 0.61, and 0.60%, respectively. The FF can be increased by reducing the recombination between the photo-excited carriers at the nanorods and the tri-iodide ions in the electrolyte. The recombination is evidenced by the low value of the parallel resistance $R_p=dV/dI|_{v=0}$ from the I-V curves under illumination. The series resistance $R_s=dV/dI|_{I=0}$ is as low as approximately 185 Ω for the aligned ZnO nanorods. The I-V characteristics of ZnO nanocrystalline thin film is showed in 5.12 (c). The V_{oc}, J_{sc}, FF, and the η are 0.46 V, 0.092mA/cm^2, 0.15, and <0.001%, respectively. The overall power conversion efficiency was obtained by using the following equation:

$$\eta = \frac{P_{out}}{P_{in}} = \frac{J_{sc} \times V_{oc} \times FF}{P_{in}}$$

The lower V_{oc} for the ZnO thin film may be contributed from the insufficient of dye coverage, the lower surface-to-volume ratio, and the fairly little amount of electrolyte direct contact with the ITO substrate. Even though the ZnO thin film can attain high V_{oc}, a relatively low I_{sc} was obtained due to the more sever electron scattering among the grain boundaries of ZnO thin film. The thicker the film is the lower the I_{sc} will be

generated. The V_{oc} of the ZnO nanorod can sustain higher due to an ultra thin layer of ZnO film (20-30nm) sputtered before growth and the nanorods can absorb more dye molecules with higher surface-to-volume ratio. Electrons can directly transport through the two ends of the nanorods. A lower V_{oc} of the ZnO nanostructure with no ZnO thin film sputtered is obtained of 630mV. Therefore, the scattering of the electrons will be dramatically decreased by replacing the 1-D ZnO nanostrucutres. The FF and the efficiency of the ZnO nanorods are greatly increased about 240 times larger than the as-sputtered ZnO thin film. The efficient charge separation and the screening of the Coulomb attraction between photogenerated charge carrier-pairs are only effective as the electrolyte ions sufficiently surround the charge-carrier pairs. The ZnO nanocrystallue thin film acts as a planer electrode which the electrolyte ions are confined to only the half-space. These kinds of planer semiconductor electrodes DSSCs have been intensively studied and those studies provided much of the knowledgeable concept for the initial analysis of DSSCs. [243,244] In contrast, the ZnO nanostructure geometry of the nanorod based-DSSC makes the phenomena different since electrolyte ions can mostly surround photogenerated charge carriers in the DSSC; no interfacial electrical field is required to affect charge separation. For dye sensitization of planer electrodes, the photogenerated electrical field between the injected carriers and the holes cannot be completely neutralized by ion motion, requires a built-in electric field (Φ_{bi}) for efficient charge separation. [202, 228, 245]

The incident photon-to-current conversion efficiency (*IPCE*) at a certain wavelength can be obtained by the following expression; [178]

$$IPCE(\%) = \frac{1240(nm \bullet eV) \times J_{sc}(\frac{\mu A}{cm^2})}{\lambda(nm) \times \Phi(\frac{\mu W}{cm^2})} \times 100$$

where Φ is the monochromatic light intensity. The IPCE for our device measured at 535 nm is 23%.

The efficiencies [246 , 247] of ZnO DSSCs based on MOCVD grown ZnO nanostructures has been reported as 0.5% and 0.55%. As shown above, the efficiency of our device is comparable to those based on MOCVD grown ZnO nanostructures. Therefore, we can tentatively conclude that thermal CVD can be used for the preparation of the ZnO nanostructure on TCO/glass substrate for the DSSC application, which is believed to be possible due to our novel DSDT CVD set up. Thermal CVD has the advantages over MOCVD because ZnO nanostructures with a controllable morphologies and high crystallinity can be synthesized in an economically viable and environmentally benign process.

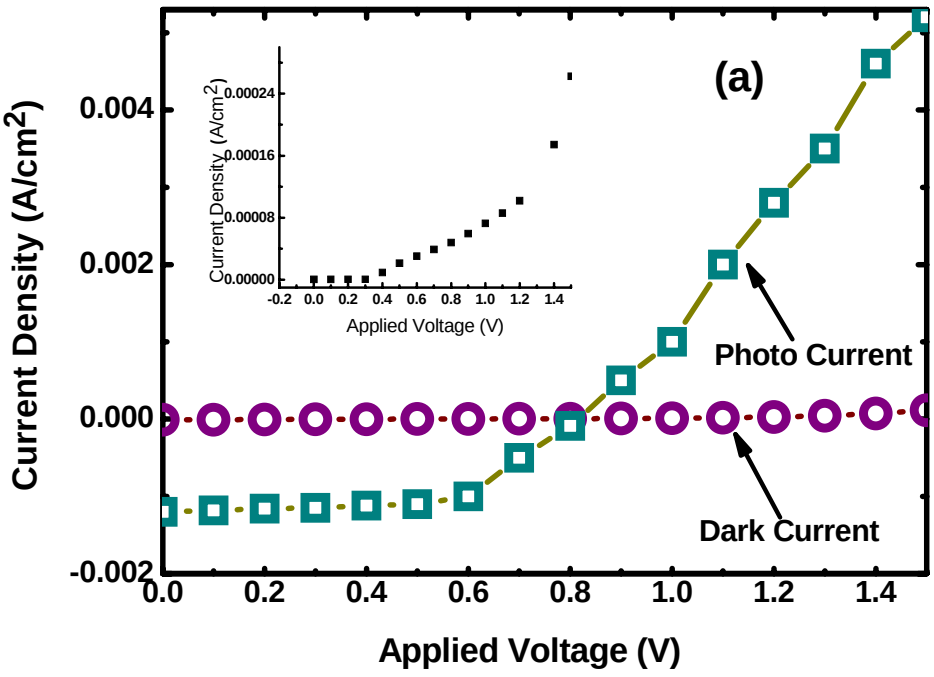
(a)
Current Density (A/cm2)
Applied Voltage (V)
Photo Current
Dark Current
0.004
0.002
0.000
-0.002
0.0
0.2
0.4
0.6
0.8
1.0
1.2
1.4
Current Density (A/cm2)
0.00024
0.00016
0.00008
0.00000
-0.2
0.0
0.2
0.4
0.6
0.8
1.0
1.2
1.4
Applied Voltage (V)

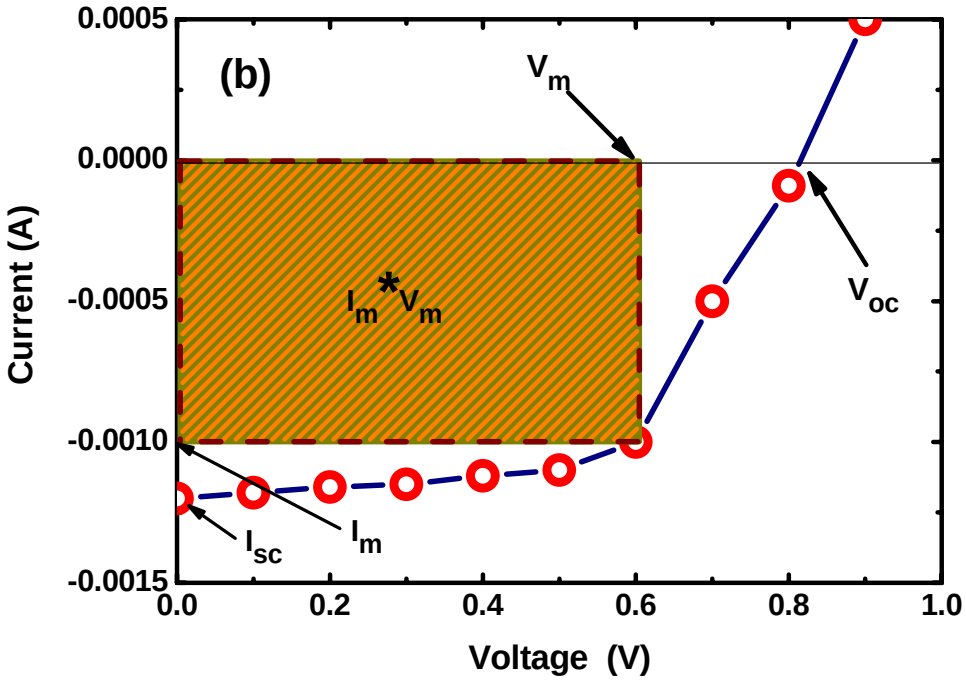
(b)
Vm
Im*Vm
Voc
Isc
Im
Current (A)
Voltage (V)
0.0005
0.0000
-0.0005
-0.0010
-0.0015
0.0
0.2
0.4
0.6
0.8
1.0

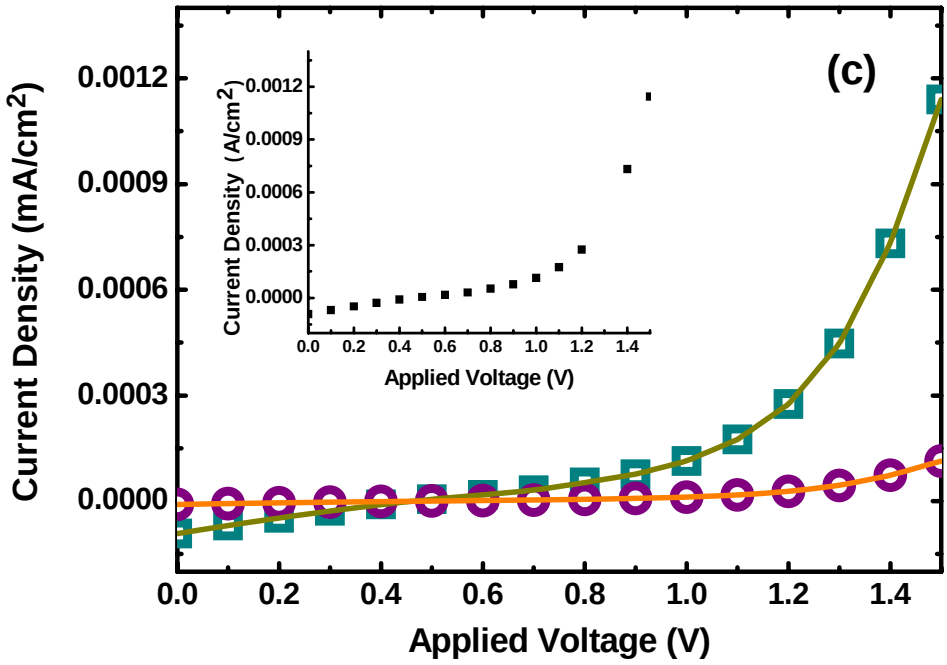

Figure 6.12 (a) Dark and photo current-voltage (I-V) characteristics of the ZnO nanrods based-DSSC. Inset shows the rescaled plot of the dark current characteristics. (b) Replotted photo I-V curve for fill factor calculation. (c) Dark and photo current-voltage (I-V) characteristics of the ZnO nanocrystalline thin film based-DSSC. Inset shows the rescaled plot of the photo current characteristics.

6.8 Conclusion

In summary, we have successfully synthesized ZnO nanorods on TCO/glass substrate using a novel DSDT thermal CVD process. The fill factor and the power conversion efficiency of the DSSC based on aligned ZnO nanorods are 0.61 and 0.6%, respectively. The IPCE of the device measured at 535 nm is 23%. The ZnO thin film has been

prepared for reference and comparison. The FF and the power conversion efficiency of the aligned ZnO nanorods are 240 times larger than the as-sputtered ZnO thin film. Electrons scattering can be greatly reduced by utilizing 1-D nanostructures and the V_{oc} can be slightly increased by sputtering an ultra thin layer of ZnO on top of ITO. It was demonstrated that thermal CVD is a viable method for the growth of ZnO nanostructure for DSSC application.

CHAPTER 7

SUMMARY AND FUTURE DIRECTION

In summary, ZnO nanostructures of different morphologies can be controllably grown by our specific DSDT system with relatively high reproducibility and high crystalllinity. The as-grown ZnO samples were confirmed to have high crystal quality by XRD and Raman spectroscopy. Raman spectra also reveal that different kinds of nanostructures have slightly different spectra. From PL spectrum, evidence can be confirmed that the ZnO nanostructures, especially the aligned ZnO nanorods, having extremely low defect level intensity as corresponding to the visible green luminescence at 500 nm. Even when the growth temperature of ZnO nanostructures is lower down to 470 °C, the processing temeperature is still relatively high as compared to chemical bath deposition (CBD), and MOCVD. Thermal CVD has the advantages of requiring less processing steps, non-toxic processes, being mass production applicable and so on. The growth temperature is one of the most important limitations for this growth method, especially for growth on flexible and transparent substrates. Low temperature PL characterization needs to be performed in order to further analyze the defect levels of ZnO nanostructures corresponding to different growth parameters.

Raman scattering of the aligned ZnO nanorods has been investigated. It has demonstrated by Raman spectroscopy that the ZnO nanorods are relatively strain free. The free carrier concentration as well as electron mobility of the ZnO nanorods were obtained via line shape analysis of the coupled A_1(LO) phonon-plasmon mode. The local temperature heating of the nanorods by the laser beam was estimated by the integrating the ratio of Stokes to anti-Stokes Raman intensity. The position of the LO phonon peak was observed to be dependent on both the temperature and the LO phonon-plasmon coupling. It is crucial to consider temperature effect in determining the frequency of the uncoupled LO phonon mode for the line shape analysis. The mobility of the aligned ZnO nanorods is about 20% lower than that of undoped bulk ZnO, which can be as attributed to the enhanced surface scattering due to a low-dimensionality of the nanorod structure. For further investigation, UV Raman can be performed for diagnosing the surface electronic properties of those ZnO nanostructures since UV light suffers an extremely high absorption while it penetrates an very thin layer of ZnO (tens of nanometer). ZnO nanostructure UV Raman can provide useful information for nano-scaled device applications such as ZnO nanowire based field effect transistor, chemical sensor, field emission display and so forth.

Room temperature Raman spectroscopy has also been used for observing the phonon lifetime of undoped bulk ZnO, aligned nanorods, and nanopowder. We found out that the lifetime of $E_2^{(2)}$ phonon mode becomes shorter as the dimensionality decreases. The $E_2^{(2)}$ lifetime decreases from 0.61 ps of a-face ZnO wafer to 0.462 ps of aligned nanorods and then down to 0.416 ps of ZnO nanopowder. The lifetime shortening is claimed to mainly

contributed form the anharmoinc decay since the PL spectrum shows that aligned nanorods and nanopowder have less visible defect emission as compared to undoped bulk ZnO. The $E_2^{(2)}$ mode exhibits a visibly asymmetric line shape that could be successfully explained in terms of resonant anharmonic interaction of the $E_2^{(2)}$ mode with a band of combined transverse and longitudinal acoustic modes. The steep variation of the two-phonon DOS around the $E_2^{(2)}$ frequency leads to a distorted phonon line shape. The anharmonic decay of $E_2^{(2)}$ mode involves a continuum of TA+LA phonons. The temperature dependence A_1(LO) and E_1(LO) modes can be accounted by a simple model in which the longitudinal phonon decays into a pair of TO and TA phonons whose frequencies correspond to a maxima of the phonon DOS. However, for more detail decay channel mechanisms of each optical phonon modes, a further and precisely temperature dependence Raman spectrum needed.

Conventional TiO_2 DSSCs has the power conversion efficiency about 11.3%, the performance of this nanoparticle-based DSSCs greatly relies on trap-limited diffusion for electron transport, which can result in a slow transport mechanism. The device working stability and efficiency would be greatly limited by this deficiency. Replacing the TiO_2 nanoparticle with ZnO nanorods has been considered as the best choice to (1) improve the cell efficiency and stability; (2) to speed up the electron transport; and (3) to prevent the recombinations. Therefore, those ZnO nanostructures that have been made *via* thermal CVD were fabricated into DSSCs. The fill factor and the power conversion efficiency of the DSSC based on aligned ZnO nanorods are 0.61 and 0.6%. Even though the conversion efficiency is competitive with other research groups' records, it is still

hard to compete with conventional TiO_2 nanoparticle solar cell. The N719 dye can be well adapted for TiO_2 nanoparticle DSSC but may not be suitable for ZnO based DSSC because of the grabbing anchors of this dye encroach the ZnO surface and the grabbing efficiency of the dye is much worse for ZnO than TiO_2. The main problem with ZnO DSSC at present is related to a complex dye-sensitization process. Acidic carboxyl groups are commonly used as anchoring groups and protons from these groups cause dissolution of Zn surface atoms with subsequent formation of Zn^{2+}/dye complexes in the nanostrucutred based DSSC. Hence, the amount of dye molecules are loaded on the ZnO nanorods surface may be poor than TiO_2 nanoparticle although ZnO nanorods provides a larger surface-to-volume ratio. The dye absorption spectrum reveals that it only absorbs a single wavelength of the solar spectrum at 535nm, which is not a powerful light absorbing media. For improving the efficiency of this type of ZnO nanorods based DSSC several approaches can be considered as followed (1) to invent other types of dye with high grabbing efficiency and low surface encroachment to ZnO; (2) to investigate new anchoring groups and to control the chemistry at the oxide/dye/electrolyte interface; (3) to invent dye that has multiple absorption wavelengths in order to enhance the light absorption efficiency and quantum yield toward red wavelength; (4) to replace absorption media to quantum dots instead of dye; (5) to enhance the surface-to-volume ration of ZnO by producing features like dendritic and flower-like structures. The electrolyte, which serves as the hole transport media, is mostly in liquid phase that greatly limited the lifetime of the solar cell and the solar cell sealing is an important issue. Research community puts lots of effort to replace the liquid type electrolyte gel either gel like (*i.e.*

extreme thin absorber) or solid type hole transport media since the DSSC is a diffusion device; therefore, the thickness of the hole transport media and the intensity of the electric field creates across the device are not the crucial factors for this type of solar cell. The surface defects on the ZnO nanostructures provide one types of the recombination centers. The surface defects can be easily detected by PL spectrum because the green luminescence from the ZnO nanostructures represents either the oxygen vacancy or Zn interstitial defects. Some annealing or plasma treatments can solve the green luminescence problems. [248]

DSSC has attracted lots of attention because it is easy to fabricate and it possesses the energy generation as low as 60 cent/pW (pW stands for peak Watt), which is relatively low as compared to silicon based solar cells. However, DSSC is still in lab scale investigation because of the lifetime, sealing, stability and long term efficiency issues. There have several different types of silicon based solar cells such as passivated emitter rear surface totally diffuse (PERT), buried contact solar cell, back contact solar cell, thin film solar cell, p-i-n single junction solar cell, hydrogenated amorphous and polycrystalline solar cells, etc. Silicon thin film solar cells are believed to be one of the next generation solar cells. Among different type of silicon thin film solar cells, p-i-n single junction solar cell possesses the most unique prospective breakthrough for next generation solar cell. Figure 7.1 (a) shows a traditional type of p-i-n solar cell. A thick intrinsic (*i*) hydrogenated amorphous silicon is sandwiched in between the n-type and p-type amorphous silicon because the diffusion length of the charge carriers is much shorter than in crystalline silicon and the photogenerated carrier would virtually recombine in the

doped amorphous silicon layers before reaching the depletion region of the p-n junction if the intrinsic layer is not present. The thickness of the p- and n- doped amorphous silicon is 10 nm and 20 nm, respectively. The doped layer originates an internal electric field across the intrinsic silicon layer and the generated internal electric field should be high enough for photogenerated charge carriers to separate. The doped layers also establish low loss ohmic electrical contacts between amorphous silicon part of the solar cell and the external electrodes. The intrinsic is the heart of p-i-n thin film solar cell since it serves as an absorber layer of the device. Traditional p-i-n solar cell can reach a maximum energy conversion of ~10%, but this kind of amorphous p-i-n solar cell suffers severe light degradation after light soaking. The energy conversion after light soaking is only 60%-80% of the original fresh devices. However, if the intrinsic amorphous silicon layer can be replaced with silicon nanostructures, as shown in Fig. 7.1(b), the light degradation can be solved and the nanostructures provides a large surface-to-volume-ration that can dramatically increase the light harvesting factor and highly increase the energy conversion efficiency. Even though this kind of silicon nanostrcutred based p-i-n solar cell has not been reported yet, growth of silicon nanostructures, as shown in Fig. 7.1 (c) and (d), is under intensive investigations. [249,250] We believe this type of novel structure based silicon thin film solar cell will bring the solar energy research into another bright future.

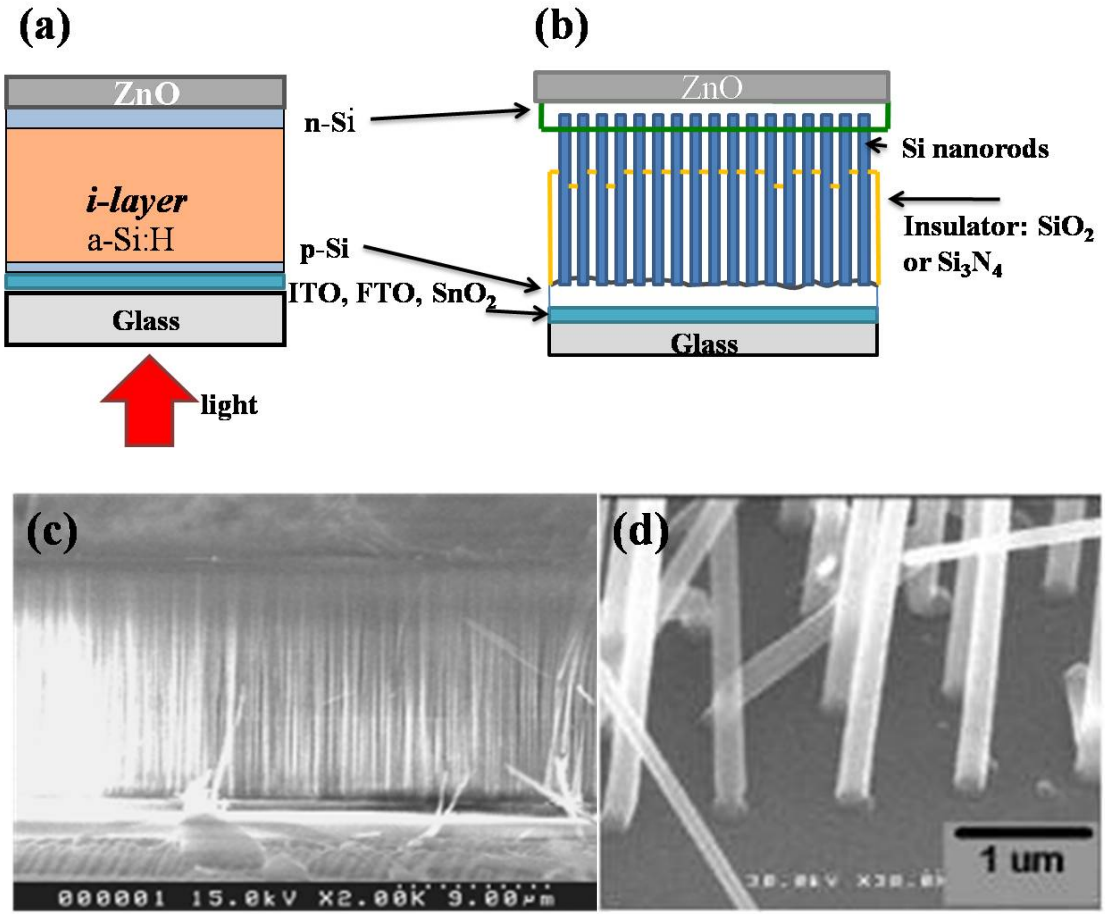

Figure 7.1 (a) schematic of traditional p-i-n solar cell; (b) silicon nanorods based p-i-n solar cell; (c) well-aligned silicon nanorods; (d) selective growth of silicon nanorods. [249, 250]

BIBLIOGRAPHY

[1] K. H. Hellwege, O. Madelung, A. M. Hellege, Numerical Data and Functional Relationship in Science and Technology (Springer-Verlag, New York, 1987).

[2] C. Jagadish and S. J. Pearton, "Zinc Oxide Bulk, Thin Films and Nanostructures Processing, Properties and Application" Elsevier (2006).

[3] Z. L. Wang and Z. C. Kang, editors, "Functional and Smart Materials", Plenum, New York (1998).

[4] Z.L. Wang, J. Phys. Condensed Matter, **16**, R829, (2004).

[5] J. Nishii, F.M. Hossain, S. Takagi, T. Aita, K. Saikusa, Y. Ohmaki, I. Ohkubo, S. Kishimoto, A. Ohtomo, T. Fukumura, F. Matsukura, Y. Ohno, H. Koinuma, H. Ohno, and M. Kawasaki, Jpn. J. Appl. Phys. **42**, L347 (2003)**.**

[6] O. Dulub, L. A. Boatner, U. Diebold, Surf. Sci. **519**, 201 (2002)

[7] J. C Phillips, Bonds and Bands in Semiconductors, Academic, New York, 1973.

[8] T. Sekiguchi, S. Miyashita, K. Obara, T. Shishido, and N. Sakagami, J. Cryst. Growth **214/215**, 72 (2000).

[9] T. Sakagami, M. Yamashita, T. Sekiguchi, S. Miyashita, K. Obara, and T. Shishido, J. Cryst. Growth **229**, 98 (2001).

[10] W.-J. Li, E.-W. Shi, W.-Z. Zhong, and Z.-W. Yin, J. Cryst. Growth **203**, 186 (1999).

[11] S. J. Pearton, D. P. Norton, K. Ip, Y. W. Heo, T. Steiner, Progess in Material Science, **50**, 293 (2005).

[12] D. Vogel, P. Kruge, J. Pollmann, Phys. Rev. B **52**, R14316 (1995).

[13] I. Ivanov and J. Pollmann, , Phys. Rev. B **24**, 7275 (1981).

[14] A. Mang, K. Reimann, and S. Rubenacke, Solid State Commun. **94**, 251 (1995).

[15] J. J. Hopfield, J. Phys. Chem. Solids **15**, 97 (1960).

[16] D.A. Long, Raman Spectroscopy, New York McGraw-Hill, 1976.

[17] G. Turrell and J. Corset, Raman microscopy : developments and applications, London; San Diego : Academic Press, (1996).

[18] W. Y. Liang and A. D. Yoffe, Phys. Rev. Lett. **20**, 59 (1968).

[19] J. F. Muth, R. M. Kolbas, A. K. Sharma, S. Oktyabrsky, and J. Narayan, J. Appl. Phys. **85**, 1884 (1999).

[20] D. C. Reynolds, D. C. Look, B. Jogai, C. W. Litton, G. Cantwell, and W. C. Harsch, Phys. Rev. B **60**, 2340 (1999).

[21] A. Teke, Ü. Özgür, S. Doğan, X. Gu, H. Morkoç, B. Nemeth, J. Nause, and H. O. Everitt, Phys. Rev. B **70**, 195207 (2004).

[22] S. F. Chichibu, T. Sota, G. Cantwell, D. B. Eason, and C. W. Litton, J. Appl. Phys. **93**, 756 (2003).

[23] S. F. Chichibu, A. Tsukazaki, M. Kawasaki, K. Tamura, Y. Segawa, T. Sota, and H. Koinuma, Appl. Phys. Lett. **80**, 2860 (2002).

[24] K. Thonke, T. Gruber, N. Teofilov, R. Schönfelder, A. Waag, and R. Sauer, Physica B **308–310**, 945 (2001).

[25] C. Boemare, T. Monteiro, M. J. Soares, J. G. Guilherme, and E. Alves, Physica B **308–310**, 985 (2001).

[26] D. C. Reynolds, D. C. Look, B. Jogai, R. L. Jones, C. W. Litton, H. Harsch, and G. Cantwell, J. Lumin. **82**, 173 (1999).

[27] R. P. Wang, G. Xu, and P. Jin, Phys. Rev. B. **69**, 113303 (2004).

[28] J. F. Muth, R. M. Kolbas, A. K. Sharma, S. Oktyabrsky, and J. Narayan, J. Appl. Phys. **85**, 7884 (1999).

[29] K. Vanheusden, W. L. Warren, C. H. Seager, D. R. Tallant, J. A. Voigt, and B. E. Gnade, J. Appl. Phys. **79**, 7983 (1996). K. Vanheusden, C. H. Seager, W. L. Warren, D. R. Tallant and J. A. Voigt, Appl. Phys. Lett. **68**, 403 (1996).

[30] A. van Dijken, E. A. Meulenkamp, D. Vanmaekelberg and A. Meijerink, J. Phys. Chem. B **104**, 1715 (2000).

[31] T. Sekiguchi, N. Ohashi and Y. Terada, Jpn. J. Appl. Phys. **36**, L289 (1997).

[32] X. Liu, X. H. Wu, H. Cao and R. P. H. Chang, J. Appl. Phys. **95**, 3141 (2004).

[33] W. S. Shi, O. Agyeman, and C. N. Xu, J. Appl. Phys. **91**, 5640 (2002).

[34] B. X. Lin, Z. X. Fu, Y. B. Jia and G. H. Liao, J. Electrochemical. S. **148**, G110 (2001).

[35] M. Anpo, Y. Kubokawa, J. Phys. Chem. **88**, 5556 (1984).

[36] S. H. Bae, S. Y. Lee, H. Y. Kim and S. Im, Optic. Mater. **17**, 327 (2001).

[37] Y. G. Wang, S. P. Lau, H. W. Lee, S. F. Yu, B. K. Tay, X. H. Zhang and H. H. Hng, J. Appl. Phys, **94**, 354 (2003).

[38] S. Adachi, Properties of Group-IV, III-V and II-IV Semiconductors, John Wiley and Sons, Ltd, West Sussex, England, 2005.

[39] T. Minami, H. Sato, H. Nanto, and S. Takata, Jpn. J. Appl. Phys., Part 2 **24**, L781 (1985).

[40] D. C. Look, B. Clafin, Y. I. Alivov, S. J. Park, Phys. Stst. Sol. A **201**, 2203 (2004).

[41] D. C. Look, J. W. Hemsky, and J. R. Sizelove, Phys. Rev. Lett. **82**, 2552 (1999); D. C. Look, D. C. Reynolds, J. R. Sizelove, R. L. Jones, C. W. Litton, G. Cantwell, and W. C. Harsch, Solid State Commun. **105**, 399 (1998).

[42] A. F. Kohan, G. Ceder, D. Morgan, and C. G. Van de Walle, Phys. Rev. B **61**, 15019 (2000).

[43] S. B. Zhang, S-H. Wei, and A. Zunger, Phys. Rev. B. **63**, 075205 (2001).

[44] C. G. Van de Walle, Phys. Rev. Lett. **85**, 1012 (2000).

[45] K. Shimomura, K. Nishiyama, and R. Kadono, Phys. Rev. Lett. **89**, 255505 (2002).

[46] H. Kato, M. Sano, K. Miyamoto, and T. Yao, J. Cryst. Growth 237–239, **538** (2002).

[47] S. Y. Myong, S. J. Baik, C. H. Lee, W. Y. Cho, and K. S. Lim, Jpn. J. Appl. Phys. Part 2 **36**, L1078 (1997).

[48] V. Assuncao, E. Fortunato, A. Marques, H. Aguas, I. Ferreira, M. E. V. Costa, and R. Martins, Thin Solid Films **427**, 401 (2003).

[49] B. M. Ataev, A. M. Bagamadova, A. M. Djabrailov, V. V. Mamedo, and R. A. Rabadanov, Thin Solid Films **260**, 19 (1995).

[50] C. H. Park, S. B. Zhang, and S.-H. Wei, Phys. Rev. B **66**, 073202 (2002).

[51] M. L. Cohen, Phys. Scr., T **T1**, 5 (1982).

[52] J. Ihm, A. Zunger, and M. L. Cohen, J. Phys. C **12**, 4409 (1979).

[53] Tsukazaki A. Ohtomo, T. Onuma, M. Ohtani, T. Makino, M. Sumiya, K. Ohtani, S. F. Chichibu, S. Fuke, Y. Segawa, H. Ohno, H. Koinuma, and M. Kawasaki, Natre Mater. **4**, 42 (2005).

[54] A. Ohtomo et al., Appl. Phys. Lett. **77**, 2204 (2000).

[55] R. P. Koffyberg, Phys. Rev. B **13**, 4470 (1976).

[56] E. R. Segnit and A. E. Holland, J. Am. Ceram. Soc. **48**, 412 (1965).

[57] D. I. Florescu, L. G. Mourokh, F. H. Pollak, D. C. Look, G. Cantwell, X. Li, J. Appl. Phys. **91**, 890 (2002).

[58] U. Ozgur, Y. I. Alivov, C. Liu, A. Teke, M. A. Reshchikov, S. Douan, V. Avrutin, S. J. Cho, H. Morkoc, J. Appl. Phys. **98**, 041301 (2005).

[59] Y. W. Heo, et al. Appl. Phys. Lett. **81**, 3046 (2002).

[60] Y. C. Kong, et al. Appl. Phys. Lett. **78**, 407 (2001).

[61] R. Zhang, Y. Lifshitz, and S. Lee, Adv. Mater. **15,** 635 (2003).

[62] M. H. Huang, et al. Adv. Mater. **13,** 113 (2001).

[63] S. C. Lyu, et al. Chem. Phys. Lett. **363**, 134 (2002).

[64] S. Y. Li, et al. J. Crystal Growth, **247**, 357 (2003).

[65] B. D. Yao, et al. Appl. Phys. Lett. **81**, 757 (2002).

[66] M. Kawakami, A. B. Hartanto, Y. Nakata, and T. Okada. Jpn. J. Appl. Phys., **42**, L33 (2003).

[67] T. Okada, B. H. Agung, and Y. Nakata, Appl. Phys. A, **79**, 1417 (2004).

[68] T. Okada, and K. Kawashima, Proceedings of SPIE - The International Society for Optical Engineering , Fifth International Symposium on Laser Precision Microfabrication, v **5662**, 420 (2004).

[69] W. Lee, M.-C. Jeong, J.-M. Myoung, Acta Materialia, **52**, 3949 (2004).

[70] J. Y. Park, D. J. Lee, Y. S. Yun, J. H. Moon, B.-T. Lee, S. S. Kim, J. Cryst. Growth, **276**, 158 (2005).

[71] J. B. Baxter, and E. S. Avdil, Appl. Phys. Lett. **86** (2005).

[72] P. Ravirajan, A. M. Peiro, M. K. Nazeeruddin, M. Graetzel, D. D. C. Bradley, J. R. Durrant, and J. Nelson, J. Phys. Chem. B **110** (2006).

[73] T. Soga, "Nanostructured materials for solar energy conversion", Elsevier, 447 (2003).

[74] C. Y. Lee, T. Y. Tseng, S. Y. Li, and P. Lin, Tamkang J. Sci. Eng, **6**, 127 (2003).

[75] Cui.Y. Lauhon, L.J. Gudiksen, M.S. Wang, and J. Lieber, Appl. Phys. Lett. **78**, 2214 (2001).

[76] Y.-J. Zeng, Z.-Z. Ye, W.-Z. Xu, L.-P. Zhu, and B.-H. Zhao, Applied Surface Science, **250** (2005).

[77] O. Tatsuo, K. Ku, N. Yoshiki, and N. Xu, J. J. Appl. Phys., **v44**, n1B (2005).

[78] X. Liu, X. H. Wu, H. Cao, and R. P. H. Chang, J. Appl. Phys. **95**, 3141 (2004).

[79] T. L. Sounart, J. Liu, J. A. Voigt, W. P. Hsu, E. D. Spoerke, Z. Tian, and Y. Jiang, Adv. Func. Mater., **16** (2006).

[80] A. E. Hichou, M. Addou, J. Ebothe, and M. Troyon, J. Lumin. **113,** 183 (2005).

[81] B. D. Yao, Y. F. Chan, and N. Wang, Appl. Phys. Lett. **81**, 757 (2002).

[82] Q. Wan, K. Yu, T. H. Wang, C. L. Lin, Appl. Phys. Lett. **83**, 2253 (2003).

[83] Q. H. Li, Q. Wan, Y. J. Chen, T. H. Wang, H. B. Jia and D. P. Yu, Appl. Phys. Lett. **85**, 636 (2004)

[84] J. Y. Lao, J. Y. Huang, D. Z. Wang, and Z. F. Ren, Nano Lett. **3**, 235 (2002).

[85] A-J. Cheng, D. Wang, H. W. Seo, C. Liu, M. Park, and Y. Tzeng, Diamond & Related Matter. **15**, 426 (2006).

[86] Z. Fan, and J. G. Lu, Journal of Nanoscience and Nanotechnology, **5**, 1561(2005).

[87] Cui.Y. Lauhon, L.J. Gudiksen, M.S. Wang, and J. Lieber, Appl. Phys. Lett. **78**, 2214 (2001).

[88] C. Y. Lee, T. Y. Tseng, S. Y. Li, and P. Lin, Tamkang J. Sci. Eng, **6**, 127 (2003).

[89] F-Q. He, Y-P. Zhao, Appl. Phys. Lett. **88**, 193113 (2006).

[90] X. Han, G. Wang, L. Zhou, and J. G. Hou, Chem. Commun., **2**, 212 (2006)

[91] K. K. Schuegraf, "Handbook of Thin Film Deposition Processes and Techniques" Noyes (1988)

[92] M. Ohring, "The Material Science of Thin Film", 1st ed. (Academic, London, 1992)

[93] J. Q. Hu, Q. Li, N. B. Wong, C. S. Lee, and S. T. Lee, Chem. Mater. **14**, 1216 (2002)

[94] R.C. Wang, C. P. Liu, J. L. Huang, and S.-J. Chen, Appl. Phys. Lett .**86** 251104 (2005)

[95] Z. Fan, and J. G. Lu, Journal of Nanoscience and Nanotechnology, **5**, 1561 (2005)

[96] R. A. Laudise and A.A. Ballman, J. Phys. Chem. **64**, 688(1960)

[97] P. X. Gao, and Z. L. Wang, Small **1,** No.10, 945 (2005).

[98] B. A. Korgel, Science **309,** 1683 (2005).

[99] X. Y. Kong, Y. Ding, R. Yang, Z. L. Wang, Science **303**, 1348 (2004).

[100] D. Wang, Doctoral Dissertation " Optical Spectroscopy of Wide-Band-Gap Semiconductors: Raman and Photoluminescence of Gallium Nitride , Zinc Oxide and Their Nanosructures"(2006)

[101] W. Y. Liang and A. D. Yoffe, Phys. Rev. Lett. **20**, 59 (1968).

[102] D. G. Thomas, J. Phys. Chem. Solids **15**, 86 (1960).

[103] J. G. A. Gardeniers, Z. M. Rittersma, and G. J. Burger, J. Appl. Phys. **83**, 7844 (1998).

[104] K. A. Alim, V. A. Fonobeov, A. A. Balndin, Appl. Phys. Lett. **86**, 053103 (2005).

[105] A. Umar, B. Karunagaran, E. K. Suh, and Y. B. Hahn, Nanotechnology, **17**, 4072 (2006)

[106] S. A. Studenikin, N. Golego, and M. Cocivera, J. Appl. Phys. **84**, 2287 (1998)

[107] K. Vanheusden, C. H. Seager, W. L. Warren, D. R. Tallant, and J. A. Voigt, J. Appl. Phys. **79**, 7983 (1996)

[108] W. Cheng, W. Ping, X. Zou, and T. Xiao, J. Appl. Phys. **100**, 054311 (2006)

[109] X. Liu, X. H. Wu, H. Cao and R. P. H. Chang, J. Appl. Phys. **95**, 3141 (2004).

[110] L. E. Greene, M. Law, J. Goldberger, F. Kim, J. C. Johnson, Y. Zhang, R. J. Saykally, and P. Yang, Angew. Chem., Int. Ed. **42**, 3031 (2003).

[111] L. Wu, Y. Wu, X. Pan, and F. Kong, Opt. Mater. **28**, 418 (2006).

[112] T. Sekiguchi, S. Miyashita, K. Obara, T. Shishido, and N. Sakagami, J. Cryst. Growth **214/215**, 72 (2000).

[113] Y. Harada and S. Hashimoto, Phys. Rev. B **68**, 045421 (2003).

[114] I. Shalish, H. Temkin and V. Narayannamurti, Phys. Rev. B **69**, 245401 (2004).

[115] D. Li, Y. H. Leung, A. B. Djurišić, Z. T. Liu, M. H. Xie, S. L. Shi, S. J. Xu and W. K.

Chan, Appl. Phys. Lett. **85**, 1601 (2004).

[116] D. Wang, N. Sathitsuksanoh, An-jen Cheng, Y. H. Tzeng, H. W. Seo, C.-C. Tin, M. J. Bozack, J. R. Williams, and M. Park, J. Appl. Phys. **99**, 113509 (2006).

[117] P. S. Xu, Y. M. Sun, C. S. Shi, F. Q. Xu, and H. B. Pan, Nucl. Instrum. Methods Phys. Res. B **199**, 286 (2003).

[118] N. E. Korsunska, L. V. Borkovska, B. M. Bulakh, L. Yu. Khomenkova, V. I. Kushnirenko and I. V. Markevich, J. Lumin.**733**, 102 (2003).

[119] E. Bylander, J. Appl. Phys. **49**, 1188 (1978).

[120] R. B. Lauer, J. Phys. Chem. Solids **34**, 249 (1973).

[121] A. Ohtomo et al., Appl. Phys. Lett. **77**, 2204 (2000).

[122] C. Gaspar, F. Costa, and T. Monteiro, J. Mater. Sci.: Mater. Electron. **12**, 269 (2001).

[123] L. Bergman, M. Dutta, C. Balkas, R.F. Davis, D. Alexson, and R.J. Nemanich. J. of Appl. Physics **85**, 3535 (1999).

[124] C.A. Arguello, D.L.Rousseau, S.P.S.Porto, Phys. Rev. **181**, 1351 (1969).

[125] L. Bergman, M. D. Bremser, W. G. Perry, R. F. Davis, M. Dutta, and R. J. Nemanich, Appl. Phys. Lett. **71**, 2157 (1997).

[126] R. Loudon, Adv. Phys. **13**, 423 (1964).

[127] G. H. Wei, J. Zi, K. Zhang, and X. Xie, J. Appl. Phys. **82**, 4693 (1997).

[128] H. Harima, H. Sakashita and S. Nakashima, Material Science Forum, **5**, 1363 (1998).

[129] Z. L. Wang, J. Phys: Condens. Matter **16**, R829 (2004).

[130] X. Duan, Y. Huang, Y. Cui, J. Wang, and C. M. Lieber, Nature **409**, 66 (2001).

[131] M. Law, D. J. Sirbuly, J. C. Johnston, J. Goldberger, R. J. Saykally, and P. Yang, Science **292**, 1897 (2001).

[132] P. Zu, Z. K. Tang, P. Yu, G. K. L. Wong, M. Kawasaki, A. Ohtomo, H. Koinuma, Y. Segawa Solid Stat. Commun.**103**, 459 (1997).

[133] D. M. Bagnall, Y. F. Chen, Z. Q. Zhu, T. Yao, S. Koyama, M. Y. Shen, T. Goto, Appl. Phys. Lett. **70**, 2230 (1997).

[134] H.-M. Cheng, H.-C.Hsu, Y.-K. Tzeng, L.-J. Lin, and W.-F. Hsieh, J. Phys. Chem. B **109**, 8749 (2005)

[135] A. Tsukazaki, A. Ohtomo, and M. Kawasaki, Appl. Phys. Lett. **88**, 152106 (2006).

[136] J.-J. Wu, D. K.-P. Wong, Advanced Materials, **19**, 2015 (2007).

[137] A. Mooradian and G. B. Wright, Phys. Rev. Lett. **16**, 999 (1966).

[138] M. Park, J. J. Cuomo, B. J. Rodriguez, W.-C. Yang, R. J. Nemanish, and O. Ambacher, J. Appl. Phys. **93**, 9542, (2003).

[139] A.F.J. Levi, J.R. Hayes, P.M. Platzman, and W.Wiegmann, Phys. Rev. Lett. **55**, 2071 (1985).

[140] C. L. Petersen and S.A. Lyon, Phys. Rev. Lett. **65**, 760 (1990).

[141] S. Das Sarma, J.K. Jain, and R. Jalabert, Phys. Rev. B. **18**, 6890 (1978).

[142] H. Sato and Y. Hori, Phys. Rev. B **36** 6033 (1987).

[143] M. Giltrow, A. Kozorezov, M. Sahraoui-Tahar, J.K. Wigmore, J.H. Davies, C.R. Stanley, B. Vogel, and C.D.W. Wilkinson, Phys. Rev. Lett. **75**, 1827 (1995).

[144] M.V. Klein in: Light Scattering in Solids, Ed. M. Cardona, Springer-Verlag, Berlin/Heidelberg/New York 1975.

[145] D. Wang, C.-C. Tin, J. R. Williams, M. Park, Y. S. Park, C. M. Park, T. W. Kang, W.-C Yang, Appl. Phys. Lett. **87**, 242105 (2005).

[146] C. A. Arguello, D. L. Rousseau, and S. P. S. Porto, Phys. Rev. **181**, 1351 (1969).

[147] R. H. Lyddane, R. G. Sachs, and E. Teller, Phys. Rev. **59**, 673 (1941).

[148] K. A. Alim, V. A. Fonobeov, and A. A. Balndin, Appl. Phys. Lett. **86**, 053103 (2005).

[149] M. Balkanski, R. F. Wallis, E. Haro, Phys. Rev. B. **28**, 1928 (1983).

[150] H. Fujimori, M. Kakihana, K. Loku, S. Goto, and M. Yoshimura, Appl. Phys. Lett. **79**, 937.

[151] W. L .Faust and C. H. Henry, Phys. Rev. Lett. **17**, 1265 (1966).

[152] M. Oshikiri, Y. Imanaka, F. Aryasetiawan, G. Kido, Physica B, **298**, 472 (2001).

[153] H. Yoshikawa, and S. Adachi, Jpn. J. Appl. Phys. **36**, 6237 (1997).

[154] B. H. Bairamov, A. Heinrich, G. Irmer, V. V. Toporov, and E. Ziegler, Phys. Stat. Sol. B. **119**, 227 (1983).

[155] K. A. Alim, V. A. Fonoberov, M. Shamsa, A. A. Balandin, J. Appl. Phys.**97**, 124313 (2005).

[156] N. Ashkenov, B. N. Mbenkum, C. Bundesmann, V. Riede, M. Lorenz, D. Spemann, E. M. Kaidashev, A. Kasic, M. Schubert, M. Grundmann, G. Wagner, H. Neumann, V. Darakchieva, H. Arwin, and B. Monemar, J. Appl. Phys. **93**,126 (2003).

[157] T. C. Damen, S. P. S. Porto, and B. Tell, Phys. Rev. **142**, 570 (1966).

[158] R. H. Callender, S. S. Sussman, M. Selders, and R. K. Chang, Phys. Rev. B **7**, 3788 (1973).

[159] L. Liao, D. H. Liu, J.C. Li, C. Liu, Q. Fu, M. S. Ye, Appl. Surface Science **240**, 175 (2005).

[160] G.W. Cong, H. Y. Wei, P. F. Zhang, W. Q. Peng, J. J. Wu, X. L. Liu, C. M. Jiao, W. G. Hu, Q. S. Zhu, and Z. G. Wang, Appl. Phys. Lett. **87**, 231903 (2005).

[161] A. Motayed, M. Vaudin, A. V. Davydov, J. Melngailis, M. He, and S. N. Mohammad, Appl. Phys. Lett. **90**, 043104 (2007).

[162] S.-H. Kim, H.-K. Kim and T.-Y. Seong, Appl. Phys. Lett. **86**, 112101 (2005).

[163] H.-K. Kim, S-H. Han, W.K. Choi, and T.-Y. Seong, Appl. Phys. Lett. **77**, 1647 (2000).

[164] B. C. Lee, K. W. Kim, M. A. Stroscio, and M. Dutta, Phys. Rev. B. **58**, 4860 (1998).

[165] C. A. Arguello, D. L. Rousseau, and S. P. S. Porto, Phys. Rev. **181**, 1351 (1969).

[166] L. Bergman, D. Alexson, P. L. Murphy, R. J. Nemanich, M. Dutta, M. A. Stroscio, C. Balkas, H. Shin, and R. F. Davis, Phys. Rev. B. **59**, 12977 (1999).

[167] T. Kozawa, T. Kachi, H. Kano, Y. Taga, M. Hashimoto, N. Koide, and K. Manabe, J. Appl. Phys. **75**, 1098 (1994).

[168] J. W. Pomeroy, M. Kauball, H. Lu, W. J. Schaff, X. Wang, and A. Yoshikawa, Appl. Phys. Lett. **86**, 223501 (2005).

[169] M. A. Stroscio, J. Appl. Phys. **80**, 6864 (1996).

[170] M. V. Kisin, V. B. Gorfinkel, M. A. Stroscio, G. Belenky, and S. Luryi, J. Appl. Phys. **82**, 2031 (1997).

[171] L. Bergman and R. J. Nemanich, J. Appl. Phys. **78**, 6709 (1995).

[172] T. R. Hart, R. L. Aggarwal, and B. Lax, Phys. Rev. B **1**, 638 (1970).

[173] B. Di Bartolo, Optical Interactions in Solids (Wiley, New York, 1968).

[174] J. Menendez and M. Cardona, Phys. Rev. B **29** 2051 (1984).

[175] P. G. Klemens, Phys. Rev. **148**, 845 (1966).

[176] B. C. Lee, K. W. Kim, M. A. Stroscio, and M. Dutta, Phys. Rev. B. **58**, 4860 (1998).

[177] R. Cusco, E. Alarcon-Llado, J. Ibanez, L. Artus, J. Jimennex, B. Wang, M. J. Callahan, Phys. Rev. B **75**, 165202 (2007).

[178] J. Serrano, A. H. Romero, F. J. Manjon, R. Kauck, M. Cardona, and A. Rubio, Phys. Rev. B **69**, 094306 (2004).

[179] C. Aku-Leh, J. Zhao, R. Marlin, J. Menendez, and M. Cardona, Phys. Rev. B **71**, 205211 (2005).

[180] H. Bernstein and G. Allen, J. Opt. Soc. Am. **45**, 237 (1955).

[181] E. E. Whiting, J. Quant. Spectrosc. Radiat. Transf. **8**, 1379 (1968).

[182] A. B. Djurisic. W. C. H. Choy, V. A. L. Roy, Y. H. Leung, C. Y. Kwong, K. W. Cheah, T.K. Gundu Rao, W. K. Chan, H. F. Lui, and C. Suryu, Adv. Func. Mater. **14**, 856 (2004).

[183] K. Vanheusden, W. L. Warren, C. H. Seager, D. R. Tallant, J. A. Voigt, and B. E. Gnade, J. Appl. Phys. **79**, 7983 (1996).

[184] A. van Dijken, E. A. Meulenkamp, D. Vanmaekelberg and A. Meijerink, J. Phys. Chem. B **104**, 1715 (2000).

[185] X. Liu, X. H. Wu, H. Cao and R. P. H. Chang, J. Appl. Phys. **95**, 3141 (2004).

[186] L. E. Greene, M. Law, J. Goldberger, F. Kim, J. C. Johnson, Y. Zhang, R. J. Saykally, and P. Yang, Angew. Chem., Int. Ed. **42**, 3031 (2003).

[187] J. M. Calleja and M. Cardona, Phys. Rev. B **16**, 3753 (1977).

[188] H. Siegle, G. Kaczmarczyk, L. Filippidis, A. P. Litvinchuk, A. Hoffmann, and C. Thomsen, Phys. Rev B **55**, 7000 (1997).

[189] B. A. Weinstein, Solid State Commun. **20**, 999 (1976).

[190] F. Widulle, T. Ruf, A. Gobel, E. Schonherr, and m. Cardona, Phys. Rev. Lett. **82**, 5281 (1999).

[191] J. Serrano, F. J. Manjon, A. H. Romero, F. Widulle, R. Lauck, and M. Cardona, Phys. Rev. Lett. **90**, 055510 (2003).

[192] J. Serrano, A. H. Romero, F. J. Manjon, R. Lauck, M. Cardona, and A. Rubio, Phys. Rev. B **69**, 094306 (2004).

[193] J. Menendez and M. Cardona, Phys. Rev. B **29**, 2051 (1984).

[194] B. K. Ridley and R. Gupta, Phys. Rev. B **43**, 4939 (1991).

[195] N. Vlachopoulos, P. Liska, J. Augustynski and M. Gratzel, J. Am. Chem. Soc., **110**, 1216-1220 (1988)

[196] B. O'Regan and M Gratzel, Nature, **353**, 737 (1991)

[197] M. Graztel, J. Potochem. Photobiol. A, **164**, 3 (2004)

[198] Y. Tachibana, J. E. Moser, M. Graztel, D. R. Klug, J. R. Durrant, J. Phys. Chem. **100**, 20056 (1996)

[199] T. Hannappel, B. Burfeindt, W. Storck, F. Willig, J. Phys. Chem. B. **101**, 6799 (1997)

[200] S. Ferrere, B. A. Gregg, J. Am. Chem. Soc. **120**, 843 (1998)

[201] A. Hagfeldt and M. Gratzel, Acc. Chem. Res, **33**, 269 (2000)

[202] G. Schlichthorl, S. Y. Huang, I. Sprague, A. J. Frank, J. Phys. Chem. B. **101**, 8141 (1997)

[203] D. Cahen, G. Hodes, M. Gratzel, J. F. Guillemoles, I. J. Riess, J. Phys. Chem. B. **104**, 2053 (2000)

[204] A. Zaban, A. Meier, B. A. Gregg, J. Phys. Chem. B. **101**, 7985 (1997)

[205] A. Zaban, S. Ferrere, B. A. Gregg, J. Phys. Chem. B. **102**, 452 (1998)

[206] K. Tennakone, G. R. R. A. Kumara, A. R. Kumarasinghe, K. G. U. Wijayantha, A. R. Sirimanne, Semicond. Sci. Technol. **10**, 1689 (1995)

[207] J. E. Moser and M. Gratzel, Chem. Phys. **176**, 493 (1993)

[208] Pichot and B. A. Gregg, J. Phys. Chem. B **104**, 6 (2000)

[209] K. Kalyanasundaram and M. Gratzel, Cood. Chem. Rev. **177**, 347 (1998)

[210] J. Poortmans, and V. Arkhipov, "Thin Film Solar Cells Fabracation, Characterization and Applications", Wiley (2006)

[211] V. Ramamurthy and K.S Schanze, "Semiconductor Photochemistry and Photophysics" CRC (2003)

[212] P. V. Kamat, I. Bedja, S. Hotchandani, and L. K. Patterson, J. Phys. Chem, **100**, 4900 (1996)

[213] M. R. Close, J. L. Peterson, and E. L. Kugler, Inorg. Chem. **38**, 1535 (1999)

[214] M. W. Peterson, M. T. Nenadovic, T. Rajh, R. Herak, O. I. Micic, J. P. Goral, and A. J. Nozik, J. Phys. Chem. **92**, 1400 (1988)

[215] V. Chikan, D. F. Kelley, J. Phys. Chem. B, **106**, 3794 (2002)

[216] D. M. Kaschak, S. A. Johnson, D. E. Hooks, H. –N. Kim, and T. E. Mallouk, J. Am. Chem. Soc. **120**, 10887 (1998)

[217] S. A. Haque, Y. Tachibana, D. R. Klug, and J. R. Durrant, J. Phys. Chem. B. **102**, 1745 (1998)

[218] A. J. Brad, L. R. Faulkner, "Electrochemical Methods", Wiley (1980)

[219] N. Kopidakis, E. A. Schiff, N.-G. Park, J. van de Lagemaat, A. J. Frank, J. Pheys. Chem. B. **104**, 3930 (2000)

[220] S. A. Hauqe, Y. Tachibana, R. L. Willis, J. E. Moser, M. Gratzel, D. R. Klug, J. R. Durrant, J. Phys. Chem. B. **104**, 538 (2000)

[221] J. W. Gibbs, "The Scientific papers of J. Willard Gibbs", Dover, New York, **1**, (1967)

[222] W. J. Moore, "Physical Chemistry", 4th Ed. Prentice-Hall, NJ (1972)

[223] B. A. Gregg, J. Phys. Chem. B, **107**, 4688 (2003)

[224] B. A. Gregg, M. C. Hanna, J. Appl. Phys. **93**, 3605 (2003)

[225] B. O. Regan and M. Grätzel, Nature **353**, 737 (1991).

[226] N. Vlachopoulos, P. Liska, J. Augustynski, and M. Grätzel, J. Am. Chem. Soc. **110**, 1216 (1988).

[227] A. J. McEvoy and M. Gratzel, Solar Energy Mater. Solar Cells **32**, 221 (1994).

[228] N. Kopidakis, K. D. Benkdtein, J. van de Lagemaat, A. J. Frank, J. Phys. Chem. B, **107**, 11307 (2003).

[229] W. Kubo, T. Kitamura, K. Hanabusa, Y. Wada, S. Yanagida, Chem. Commun. **5**, 374 (2002).

[230] F. Mazille, Z. Fei, D. Kuang, D. Zhao, S. M. Zakeeruddin, M. Gratzel, P. J. Dyson, Inorg. Chem. **45**, 1585 (2006).

[231] D. Kuang, S. Ito, B. Wanger, C. Klein, J.-E. Moser, R. Humphry-Baker, S.M. Zakeeruddin, M. Grätzel, J. Am. Chem. Soc. **128**, 4146 (2006).

[232] J. B. Baxter, and E. S. Aydil, Appl. Phys. Lett, **86**, 053114 (2005).

[233] M. Law, L.E. Greene, A. Radenovic, T. Kuykendall, J. Liphard, and P. Yang, J. Phys. Chem B, **110**, 22652 (2006).

[234] E. Galoppini, J. Rochford, H. Chen, G. Saraf, Y. Lu, A. Hagfeldt, and G. Boschloo, J. Phys. Chem B, **110**, 16159 (2006).

[235] A. D. Pasquier, H. Chen and Y. Lu, Appl. Phys. Lett. **89**, 253513 (2006)

[236] M. Law, L.E. Greene, A. Radenovic, T. Kuykendall, J. Liphard, and P. Yang, J. Phys. Chem B, **110**, 22652 (2006).

[237] J. B. Baxter, M. Reichman, and E. S. Aydil, 51st Int'l AVS Symp., Anaheim, CA, Nov. 2004.

[238] X. Han, G. Wang, L. Zhou, and J. G. Hou, Chem. Commun., **2**, 212 (2006).

[239] C. Y. Jiang, X. W. Sun, G. Q. Lo, D. L. Kwon, and J. X. Wang, Appl. Phys. Lett. **90**, 263501 (2007).

[240] K. Vanheusden, C. H. Seager, W. L. Warren, D. R. Tallant, and J. A. Voigt, J. Appl. Phys. **79**, 7983 (1996).

[241] W. Cheng, W. Ping, X. Zou, and T. Xiao, J. Appl. Phys. **100**, 054311 (2006).

[242] R. Chandrasekhar and K.L. Choy, Thin Solid Films, **398-399**, 59 (2001).

[243] B. A. Parkinson, M. T. Spitler J. Phys. Chem. **89**, 1453 (1992)

[244] M. T. Spitler J. Electroanal. Chem. **228**, 69 (1987).

[245] K. P. Charle, F. Willig Chem. Phys. Lett. **57**, 253 (1978).

[246] J. B. Baxter, and E. S. Aydil, Appl. Phys. Lett, **86**, 053114 (2005).

[247] A. D. Pasquier, H. Chen and Y. Lu, Appl. Phys. Lett. **89**, 253513 (2006).

[248] D. Wang, H. W. Seo, C.-C. Tin, M. J. Bozack, J. R. Williams, M. Park. N. Sathitsuksanoh, A.-J. Cheng, and Y. Tzeng, J. Appl. Phys. **99**, 113509 (2006).

[249] T.-C. Wong, J.-J. Wu, Mat. Res. Soc. Sypm. Proc. **715**, A8.2.1 (2002).

[250] B. M. Kayes, J. M. Spurgeon, T. C. Sadler, N. S. Lewis, and H. A. Atwater, Photovoltaic Energy Conversion, IEEE 4th World Conf., **1**, 221 (2006).

APPENDIX

LPP formula:

$$I(\omega) = cont \bullet A(\omega) \bullet \mathrm{Im}[-\varepsilon(\omega)^{-1}]$$

$$A(\omega) = 1 + 2C\frac{\omega_{TO}^2}{\delta}[\omega_p^2\gamma(\omega_{TO}^2 - \omega^2) - \omega^2\Gamma(\omega^2 + \gamma^2 - \omega_p^2)] + C^2\{\omega_p^2[\gamma(\omega_{LO}^2 - \omega_{TO}^2) + \Gamma(\omega_p^2 - 2\omega^2)] + \omega^2\Gamma(\omega^2 + \gamma^2)\} \times \left(\frac{\omega_{TO}^4}{\delta(\omega_{LO}^2 - \omega_{TO}^2)}\right)$$

$$\delta = \omega_p^2\gamma[(\omega\Gamma)^2 + (\omega_{TO}^2 - \omega^2)^2] + \omega^2\Gamma(\omega^2 + \gamma^2)(\omega_{LO}^2 - \omega_{TO}^2)$$

$$\varepsilon(\omega) = \varepsilon_\infty\left(1 + \frac{\Omega^2}{\omega_{TO}^2 - \omega^2 - i\omega\mathrm{T}} - \frac{\omega_p^2}{\omega(\omega + i\gamma)}\right)$$

CompleteExpand[

```
δ = Wp^2 × γ × {(W × Γ)^2 + (WTO^2 - W^2)^2} +
    W^2 × Γ × (W^2 + γ^2) × (WLO^2 - WTO^2);
A_W =
 1 + 2 × C × (WTO^2/δ) [Wp^2 × γ × (WTO^2 - W^2) - W^2 × Γ × (W^2 + γ^2 - Wp^2)] +
  C^2 × {Wp^2 [γ * (WLO^2 - WTO^2) + Γ * (Wp^2 - 2 × W^2)] +
      W^2 × Γ × (W^2 + γ^2)} × WTO^4/(δ × (WLO^2 - WTO^2))
```

]

$$\left\{1+2\,C\left\{\frac{w_{T0}^2}{w^2\,(w^2+\gamma^2)\,\Gamma\,(w_{L0}^2-w_{T0}^2)+\gamma\,w_p^2\left(w^2\,\Gamma^2+(-w^2+w_{T0}^2)^2\right)}\right\}\right.\left[\right.$$
$$-w^2\,\Gamma\,(w^2+\gamma^2-w_p^2)+\gamma\,w_p^2\,(-w^2+w_{T0}^2)\left.\right]+$$
$$\left.\left(C^2\,w_{T0}^4\,(w^2\,(w^2+\gamma^2)\,\Gamma+w_p^2\left[\Gamma\,(-2\,w^2+w_p^2)+\gamma\,(w_{L0}^2-w_{T0}^2)\right]\right)\right)\Big/$$
$$\left((w_{L0}^2-w_{T0}^2)\right.$$
$$\left.\left.\left(w^2\,(w^2+\gamma^2)\,\Gamma\,(w_{L0}^2-w_{T0}^2)+\gamma\,w_p^2\left(w^2\,\Gamma^2+(-w^2+w_{T0}^2)^2\right)\right)\right)\right\}$$

```
ComplexExpand[
  Im[-(e8 * (1 - wp^2/(w * (i * r + w)) + X^2/(-i * T * w - w^2 + wto^2)))^
    -1]]
```

$$(r\,wp^2)\Big/\left(e8\,w\,(r^2+w^2)\left(\left(\frac{r\,wp^2}{w\,(r^2+w^2)}+\frac{T\,w\,X^2}{T^2\,w^2+(-w^2+wto^2)^2}\right)^2+\left(1-\frac{wp^2}{r^2+w^2}+\frac{(-w^2+wto^2)\,X^2}{T^2\,w^2+(-w^2+wto^2)^2}\right)^2\right)\right)+$$
$$(T\,w\,X^2)\Big/\left(e8\,\left(T^2\,w^2+(-w^2+wto^2)^2\right)\right.$$
$$\left.\left(\left(\frac{r\,wp^2}{w\,(r^2+w^2)}+\frac{T\,w\,X^2}{T^2\,w^2+(-w^2+wto^2)^2}\right)^2+\left(1-\frac{wp^2}{r^2+w^2}+\frac{(-w^2+wto^2)\,X^2}{T^2\,w^2+(-w^2+wto^2)^2}\right)^2\right)\right)$$

;

$$
\begin{aligned}
&\text{FullSimplify}\Big[\\
&\quad S\Big[\\
&\qquad 1+\\
&\qquad\quad 2\times C\times\frac{w_{T0}^2}{\delta}\left[w_p^2\times\gamma\times\left(w_{T0}^2-w^2\right)-w^2\times\Gamma\times\left(w^2+\gamma^2-w_p^2\right)\right]+\\
&\qquad\quad C^2\times\left\{w_p^2\left[\gamma*\left(w_{L0}^2-w_{T0}^2\right)+\Gamma*\left(w_p^2-2\times w^2\right)\right]+\right.\\
&\qquad\qquad \left.w^2\times\Gamma\times\left(w^2+\gamma^2\right)\right\}\times\frac{w_{T0}^4}{\delta\times\left(w_{L0}^2-w_{T0}^2\right)}\Big]\times\\
&\quad\left(\left(\gamma\, w_p^2\right)\Big/\right.\\
&\qquad\left(e8\, w\left(w^2+\gamma^2\right)\right.\\
&\qquad\quad\left(\left(\frac{\gamma\, w_p^2}{w\left(w^2+\gamma^2\right)}+\frac{w\,\Gamma\,\Omega^2}{w^2\Gamma^2+\left(-w^2+w_{T0}^2\right)^2}\right)^2+\right.\\
&\qquad\qquad\left.\left.\left.\left(1-\frac{w_p^2}{w^2+\gamma^2}+\frac{\Omega^2\left(-w^2+w_{T0}^2\right)}{w^2\Gamma^2+\left(-w^2+w_{T0}^2\right)^2}\right)^2\right)\right)+\\
&\qquad\left(w\,\Gamma\,\Omega^2\right)\Big/\\
&\qquad\left(e8\left(w^2\Gamma^2+\left(-w^2+w_{T0}^2\right)^2\right)\right.\\
&\qquad\quad\left(\left(\frac{\gamma\, w_p^2}{w\left(w^2+\gamma^2\right)}+\frac{w\,\Gamma\,\Omega^2}{w^2\Gamma^2+\left(-w^2+w_{T0}^2\right)^2}\right)^2+\right.\\
&\qquad\qquad\left.\left.\left.\left.\left(1-\frac{w_p^2}{w^2+\gamma^2}+\frac{\Omega^2\left(-w^2+w_{T0}^2\right)}{w^2\Gamma^2+\left(-w^2+w_{T0}^2\right)^2}\right)^2\right)\right)\right)\Big]
\end{aligned}
$$

$$\left(S\left[\left\{ 1 + 2\,C \left\{ \frac{w_{T0}^2}{w^2\,(w^2+\gamma^2)\,\Gamma\,(w_{L0}^2 - w_{T0}^2) + \gamma\,w_p^2\left(w^2\,\Gamma^2 + (w^2 - w_{T0}^2)^2\right)} \right\} \right.\right.\right.$$
$$\left[-w^2\,(w^2+\gamma^2)\,\Gamma + w_p^2\,(w^2\,(-\gamma+\Gamma) + \gamma\,w_{T0}^2) \right] + (C^2\,w_{T0}^4$$
$$(w^2\,(w^2+\gamma^2)\,\Gamma + w_p^2[-2\,w^2\,\Gamma + \gamma\,w_{L0}^2 + \Gamma\,w_p^2 - \gamma\,w_{T0}^2]))\Big/$$
$$\Big((w_{L0}^2 - w_{T0}^2)\left(w^2\,(w^2+\gamma^2)\,\Gamma\,(w_{L0}^2 - w_{T0}^2) + \right.$$
$$\left.\left.\left.\gamma\,w_p^2\left(w^2\,\Gamma^2 + (w^2 - w_{T0}^2)^2\right)\right)\right)\right\}\Big]$$
$$\left.\left.(w^3\,(w^2+\gamma^2)\,\Gamma\,\Omega^2 + w\,\gamma\,w_p^2\,(w^4 + w^2\,\Gamma^2 - 2\,w^2\,w_{T0}^2 + w_{T0}^4))\right)\right)\Big/$$
$$(e8\,(w_p^4\,(w^4 + w^2\,\Gamma^2 - 2\,w^2\,w_{T0}^2 + w_{T0}^4) + w^2\,(w^2+\gamma^2)$$
$$(w^4 + \Omega^4 + w^2\,(\Gamma^2 - 2\,\Omega^2) - 2\,(w-\Omega)\,(w+\Omega)\,w_{T0}^2 + w_{T0}^4) -$$
$$2\,w^2\,w_p^2\,(w^4 - \gamma\,\Gamma\,\Omega^2 + w^2\,(\Gamma-\Omega)\,(\Gamma+\Omega) +$$
$$(-2\,w^2 + \Omega^2)\,w_{T0}^2 + w_{T0}^4)))$$